Title
Laser-Driven Shock Compression Studies of Planetary Compositions

Permalink
https://escholarship.org/uc/item/73g7z3mj

Author
Spaulding, Dylan Kenneth

Publication Date
2010

Peer reviewed|Thesis/dissertation

Laser-Driven Shock Compression Studies of Planetary Compositions

By

Dylan Kenneth Spaulding

A dissertation submitted in partial satisfaction of the
Requirements for the degree of
Doctor of Philosophy

in

Earth and Planetary Science

in the

GRADUATE DIVISION
of the
UNIVERSITY OF CALIFORNIA, BERKELEY

Committee in charge:
Professor Raymond Jeanloz, Chair
Professor Walter Alvarez
Professor Geoffrey Marcy

Fall 2010

Laser-Driven Shock Compression Studies of Planetary Compositions

by

Dylan Kenneth Spaulding

Abstract

Laser-Driven Shock Compression Studies of Planetary Compositions

by Dylan Kenneth Spaulding

Doctor of Philosophy in Earth and Planetary Science
University of California, Berkeley
Professor Raymond Jeanloz, Chair

The physical and chemical properties of materials are profoundly affected by high pressure and temperature and differ significantly from the behavior commonly observed at ambient conditions. Understanding the interior dynamics and evolution of planetary bodies thus requires measurement of the equations of state of materials at these extreme conditions. Experiments employing laser-driven shock compression now permit exploration of phase space spanning orders of magnitude in pressure and temperature.

Results are presented here from a suite of laser-driven shock experiments on three major mineral phases of significance to the terrestrial mantle: SiO_2, MgO and $MgSiO_3$. New optical diagnostics, including an absolutely calibrated streaked optical pyrometry system were developed to measure shock temperatures from ~ 4000-60,000 K. This system was applied to observe high-pressure phase transitions and melting at previously unexplored conditions.

Experiments on two polymorphs of SiO_2 are used to validate experimental technique and pyrometry calibration and are compared to previous results. Data on MgO and $MgSiO_3$ constrain controversial predications for the ultra-high pressure melt curves and support melting temperatures at the Earth's core-mantle boundary higher than most previous predictions. In the case of $MgSiO_3$, the first observations of a distinct liquid-liquid phase transformation in a silicate material are presented. Experiments on amorphous and crystalline $MgSiO_3$ starting materials show evidence of a transition to a high-pressure liquid phase approximately 10% denser than the low-pressure counterpart. Isochemical liquid-liquid phase separation may represent a previously unrecognized means of geochemical partitioning in early planetary history. Finally, discussions of the transport properties of each material are given and it is found that all three transform to metallic liquids upon melting with high thermal and electrical conductivity, suggesting the possibility of enhanced electromagnetic coupling across the core-mantle boundary in the molten state.

Table of Contents

CHAPTER 5: SHOCK COMPRESSION OF $MgSiO_3$: FIRST OBSERVATIONS OF A LIQUID-LIQUID PHASE TRANSITION IN SILICATE MELT

<u>SECTION III – APPENDICES</u>

List of Figures

CHAPTER 1: INTRODUCTION

CHAPTER 2: CONSTRUCTION AND CALIBRATION OF A STREAKED OPTICAL PYROMETER FOR SHOCK TEMPERATURE MEASUREMENTS

CHAPTER 3: SHOCK COMPRESSION OF SiO_2: EXPERIMENTAL VALIDATION WITH QUARTZ AND FUSED SILICA

CHAPTER 4: SHOCK COMPRESSION OF SINGLE-CRYSTAL MgO

CHAPTER 5: SHOCK COMPRESSION OF $MgSiO_3$: FIRST OBSERVATIONS OF A LIQUID-LIQUID PHASE TRANSITION IN SILICATE MELT

CONCLUSIONS

APPENDIX A - EXPERIMENTAL TECHNIQUES AND METHODS

APPENDIX B – STREAKED OPTICAL PYROMETER: TECHNICAL DETAILS

List of Tables

CHAPTER 1: INTRODUCTION

CHAPTER 2: CONSTRUCTION AND CALIBRATION OF A STREAKED OPTICAL PYROMETER FOR SHOCK TEMPERATURE MEASUREMENTS

CHAPTER 3: SHOCK COMPRESSION OF SiO_2: EXPERIMENTAL VALIDATION WITH QUARTZ AND FUSED SILICA

CHAPTER 4: SHOCK COMPRESSION OF SINGLE-CRYSTAL MgO

CHAPTER 5: SHOCK COMPRESSION OF $MgSiO_3$: FIRST OBSERVATIONS OF A LIQUID-LIQUID PHASE TRANSITION IN SILICATE MELT

CONCLUSIONS

APPENDIX A - EXPERIMENTAL TECHNIQUES AND METHODS

APPENDIX B – STREAKED OPTICAL PYROMETER: TECHNICAL DETAILS

List of Symbols

U_s	Shock Velocity (km/sec)
U_p	Particle Velocity (km/sec)
ρ	Compressed Density (g/cm^3)
ρ_0	Initial Density (g/cm^3)
V	Compressed Volume (cm^3/g)
V_0	Initial Volume (cm^3/g)
P	Pressure (GPa)
P_0	Initial Pressure (GPa)
E	Internal Energy (J/kg, unless otherwise noted)
E_0	Initial Internal Energy (J/kg)
$R_{\lambda=532nm}$, R	Reflectivity at 532 nm (normalized to 1 unless otherwise noted)
T	Temperature (K)
n_0	Zero-Pressure Index of Refraction
λ	Wavelength (nm)
C_V	Isochoric Specific Heat (3Nk$_B$)
γ	Gruneisen Parameter
α	Coefficient of Thermal Expansion (K^{-1})
I	Intensity (counts)
k_B	Boltzmann's Constant (J•K^{-1})
h	Planck's Constant (J•s)
ε	Emissivity
σ	Electrical Conductivity (Ω-cm)$^{-1}$

Acknowledgements

First and foremost, many thanks to Raymond Jeanloz for allowing me to be part of his group at Berkeley, for introducing me to high-pressure and for providing all the support that was necessary to be able to complete the work presented here.

To the entire shock physics group at Lawrence Livermore- thank you for acting as a family of advisors and allowing me access to resources, facilities and, most importantly, your own expertise, without which none of this would have been possible.

To Walter Alvarez- thank you for inspiring discussions, for giving me an annual dose of ‘real’ geology in the field in Utah and for allowing me to participate in the development of ‘Big History’ at Berkeley in which you set a high bar for my future teaching endeavors.

To my office mates, past and present in 255 McCone- thanks for the moral support along the way, the constant distraction and all the marbles.

To my family- Thank you for always allowing me access to the best educational opportunities, both in terms of my taste for expensive schools all those years and also in the form of boats, cars and common sense.

Thanks to the Krell Institute for their financial support through the SSGF graduate fellowship program.

Chapter 2 has been summarized in a paper in the proceedings of the 2007 American Physical Society conference on Shock Compression of Condensed Matter. Chapters 4 and 5 are presently in submission with co-authors R. S McWilliams, J. H. Eggert, P. M. Celliers, D. G. Hicks, R. F. Smith, G. W. Collins and R. Jeanloz.

"at somewhere between 0.6 and 0.5 of the radius, measured from the surface, a very marked and remarkable change in the nature of the material, of which the Earth is composed, takes place."

- R.D. Oldham, 1913

SECTION I – INTRODUCTION AND TECHNICAL ASPECTS

Chapter 1
Introduction

The vast majority of the matter in the Universe represented in the Periodic Table exists under high-pressure conditions in the interiors of planetary bodies and stars, and yet our understanding of the material properties for most elements and compounds is limited to what we can observe at standard temperature and pressure. As fundamental thermodynamic variables, pressure and temperature can have a profound effect on the atomic packing structure and chemical properties of a material. Measurements of the equations of state of materials at extreme conditions are thus necessary to begin to understand the formation and evolution of celestial bodies, as well as myriad questions in basic materials science and fundamental physics and chemistry.

Pressure-volume-temperature (*PVT*) equations of state were first described for the ideal gas by Boyle [1662]. This work was greatly expanded upon during the 'golden age of chemistry' in the 19th century by scientists such as Clapeyron [1834], who put in place much of the thermodynamic basis for studying the high-pressure phase diagrams of materials. Practical laboratory techniques for exploring high-pressure states of materials did not begin in earnest until the work of Percy Bridgman [1923], who developed some of the first experimental devices for static high-pressure experiments. Bridgman's contributions were of tremendous importance to materials science, earning him a Nobel prize in 1946, but also paved the way for the exploration of geophysical materials at the conditions of the deep crust and upper mantle. Static techniques, particularly using the diamond anvil-cell (DAC), have evolved significantly since Bridgman's time but are inherently restricted by the mechanical limitations of the high-pressure vessel (diamond anvils *etc*.). Consequently, it remains an experimental challenge to simultaneously compress and heat samples to conditions much in excess of two million atmospheres (200 GPa). Perhaps anticipating these limitations, Bridgman ends his collected work with a particularly prescient observation, writing "the very highest pressures will doubtless continue to be reached by some sort of shock-wave technique." [Bridgman, 1964].

Indeed, following the second world war, nuclear-driven shock waves were used to achieve extremely high pressures for the first time and experimental techniques based around underground nuclear tests were developed in parallel in the United States and in the former Soviet Union [Trunin, 1998]. Flyers driven by compressed gas also began to be employed in the laboratory as a more practical and controlled means of performing repeated experiments at shock pressures of up to ~200-300 GPa. Today, high-accuracy material studies are routinely performed using both static and dynamic techniques as well as combinations of these methods [Jeanloz *et al.*, 2007]. The following chapters present experimental results from shock wave experiments obtained using laser ablation to drive a pressure wave through the sample (described fully in appendix A). Laser-driven shock waves permit exploration of pressure-temperature space spanning several tens of millions of atm (several TPa) and hundreds of thousands of degrees and are thus a means of achieving conditions far above all but the nuclear experiments mentioned above. Recent advances at large laser facilities such as the National Ignition Facility (Lawrence Livermore National Lab) are just beginning to permit even these conditions to be matched in the laboratory, allowing controlled and precise equation of state measurements at the conditions of stellar interiors.

In the case of the Earth, deep drilling has allowed direct sampling of material from up to 12 km depth, however this represents only ~0.19% of the Earth's radius [Kozlovsky, 1987]. Although some samples brought to the surface by geologic processes (xenoliths, kimberlites *etc.*) provide additional insight into the conditions at which they formed, most are subject to physical and chemical alteration upon decompression and cooling. Experiments at high pressure and temperature are thus the only means of observing materials under conditions comparable to the deep Earth and other planets.

Of particular interest are the equations of state of the liquid components of the mantle and the melting curves of the major mineral phases. This thesis examines these properties and the shock-wave (Hugoniot) equation of state for three end-member compositions of primary importance to Earth science: SiO_2, MgO and $MgSiO_3$. After hydrogen and helium, magnesium, silicon and oxygen are three of the most abundant elements in the solar system and are expected to compose greater than 80% of the terrestrial mantle. Shock experiments allow us to probe the role of these compositions in the processes that began some 4.56 billion years ago and lead to the present day Earth. Large impact events such as the one thought to be responsible for forming the Earth-Moon system would have melted large portions of the planet [Canup *et al.*, 2001] while present-day heterogeneities at the Earth's core-mantle boundary have been cited as evidence of extensive melting in the past [Labrosse *et al.*, 2007] and possibly as remnant pockets of partial melt [Lay *et al.,* 2004]. The structure and evolution of the planet thus owes itself to the high-pressure properties of the constituent minerals, in particular the melting behavior and transport properties of the liquid phases of these materials which dictate their stability and their role in the geodynamic processes that govern planetary evolution.

Looking beyond the Earth, recent recognition of the ubiquity of extra-solar planets with masses of a few to several tens of Earth-masses [Borucki *et al.*, 2010; Howard *et al.*, 2010] introduces the question of whether these 'super Earths' have undergone similar evolutionary histories, assuming similar composition. The results presented in the subsequent chapters suggest the possibility that this may not be the case. Phase transitions at higher pressures and temperatures than are encountered in the Earth as well as previously unexpected types of transitions (Chapter 5) introduce the possibility that mantle-core equilibration in larger mass planets may proceed differently than in the Earth. As the physical and transport properties of planetary materials evolve with pressure and temperature, corresponding evolution of the chemical behavior may affect the dynamics of 'super Earth' interiors and the final ('steady-state') structure of the planet. Knowledge of this evolution is one of the important components in understanding how to create the planetary conditions necessary for the origin and sustenance of life. The evolution of chemical properties with pressure is significant not only for planetary studies but also to understand the fundamental changes in chemistry and physics induced by high pressures from a basic science perspective.

Experiments such as those presented here permit us to explore new kinds of 'extreme chemistry' brought about at the conditions accessed by laser-driven shock. This is because the thermodynamic work done by compression results in a change in the internal energy of the sample. For compression to the million-atmosphere (100 GPa) level, this change is roughly comparable with the bonding energies of valence electrons for many materials [Jeanloz *et al.*, 2007]. Extreme pressure can thus change the nature of the chemical bond and introduce the potential for a new type of high-pressure chemistry. Understanding such changes is of fundamental importance for the study of novel materials, interactions in condensed matter and of course, for testing theories and models of planetary formation and evolution.

This dissertation explores such questions and presents experimental results up to TPa pressures for major constituents of the terrestrial mantle and probable composition of extra-solar 'rocky' planets. The remainder of the first section presents the technical and experimental details of shock temperature measurements, describing how we characterize the high-pressure state. The second section presents research results, beginning with proof-of-concept experiments on SiO_2 as a prototypical oxide and the fundamental building block of more complex silicates. This is followed by results on MgO and $MgSiO_3$, in which observation of several high-pressure phase transitions is discussed. Estimations of the thermodynamic and optical properties of these materials are presented as they relate to electrical and thermal transport properties. These results represent the highest pressure observations to date in MgO and $MgSiO_3$ and the first extensive exploration of the liquid phase of both materials.

References

Borucki, W.J. *et al.*, *Science*, **327**, 977-980 (2010).

Boyle, R., *New Experiments Physico-Mechanical, Touching the Spring and Weight of the Air, and its Effects*, H. Hall, Oxford (1662).

Bridgman, P.W., *Proceedings of the American Academy of Arts and Sciences*, ***58***, 166-242 (1923).

Bridgman, P W, Collected Experimental Papers, seven volumes, Cambridge, MA: Harvard University Press (1964).

Canup R. M., Asphaug E., *Nature,* **412**, 708–712 (2001).

Clapeyron, B. P. E., *Mémoire sur la Puissance Motrice de la Chaleur*, *Journal de l'École Polytechnique, Paris*, **14**, 153–190 (1834).

Howard, A.W. *et al.*, *Science*, **320**, 653-655 (2010).

Jeanloz, R. *et al.*, *Proceedings of the National Academy of Arts and Sciences*, **104**, 9172 (2007).

Kozlovsky, Ye.A, The Superdeep Well of the Kola Peninsula. Berlin: Springer Verlag, p. 558 (1987).

Labrosse, S., Herlund, J.W., Coltice, N., *Nature*, **450**, 6 (2007).

Lay, T., Garnero, E.J., Williams, Q., *Phys. of Earth and Planetary Interiors*, **146**, 441-467 (2004).

Marsh, S.P., LASL Shock Hugoniot Data, University of California Press, Berkeley, pp. 658 (1980).

Pushcharovskĭ, D Yu, *Minerals of the Deep Geospheres*, *Physics Uspekhi*, **45**, 4 (2002).

Trunin, R. F., *Shock Compression of Condensed Materials*, Cambridge Univ. Press, Cambridge, UK (1998).

Chapter 2
Construction and Calibration of a Streaked Optical Pyrometer for Shock Temperature Measurements

ABSTRACT

Of the extensive properties typically measured for equation of state studies, temperature has historically been one of the most difficult to determine experimentally, in particular on short timescales and at extreme pressures. This chapter describes the construction and calibration of new optical diagnostics for laser-driven dynamic-compression experiments at the Janus Laser facility at Lawrence Livermore National Laboratory. A streaked optical pyrometer (SOP) was developed to measure brightness temperatures from shock-compressed samples with high temporal (~100 psec) and spatial (~10 μm/pixel) resolution. Two techniques for absolute calibration of the system are described and an example is given of the data reduction process. Finally, a brief description is given of experiments to measure temporally-resolved broadband reflectivity between 532 and ~850 nm by supercontinuum generation in an optical fiber. These new tools expand capabilities to probe the thermal and electronic states of matter at high pressure and temperature.

INTRODUCTION

Laser-driven dynamic compression experiments are increasingly being applied to characterize materials at ultra-high temperatures and pressures. Such experiments typically use velocity interferometry to infer the kinematic properties (pressure, P, density, ρ, and internal energy, E) of the equation of state (EOS), however the temperature and optical properties of materials are not as widely characterized under such conditions, and have historically proven difficult to obtain. In the context of shock compression, the kinematic properties are related by simple relationships dictated by conservation of mass, momentum and energy (described in appendix A). Temperature, however, cannot be simply extracted from conservation relationships without independent knowledge of the heat capacity of the sample. Although shock temperatures can be estimated by assuming the pressure and temperature-dependence of specific heat, such predictions are uncertain and cannot capture the effects of phase transitions on the thermal behavior of the material. Complete and precise equation of state studies thus require experimental determination of temperature. This is most often achieved by observing the blackbody-like thermal emission from the sample and comparing its intensity to a source of known spectral radiance.

The pyrometer described here permits temporally and spatially resolved observations tracking the evolution of temperature as the shock propagates through the sample. In this manner, phase changes which affect the thermal properties of the material can be detected and correlated with simultaneous pressure measurements from velocimetry data, mapping the complete Hugoniot equation of state of the sample.

This chapter also briefly introduces an exploratory technique for measuring broadband optical reflectivity. Measurement of the optical properties as a function of pressure can reveal changes in electronic behavior and band structure that may not be closely coupled to the often-observed kinematic variables mentioned above. This introduces the possibility of observing changes in chemical bonding that can occur at ultra-high pressures. Measurement of optical reflectivity also provides a means of measuring the wavelength-dependence of sample emissivity, thus potentially improving the accuracy of absolute temperature measurements based on the assumption of grey-body behavior. Together with existing diagnostic capabilities at the Janus facility, these tools allow the possibility of robust P-V-T equation of state experiments and material studies at multi-Mbar dynamic pressures.

HEATING UNDER SHOCK

High pressure and high temperature are inextricably linked, both in nature and in the laboratory. Planetary isentropes increase in temperature with depth such that laboratory studies seeking to understand the material properties of deep planetary interiors must simultaneously pressurize and heat the sample to accurately describe the material response in a geophysical context. Static high-pressure techniques in the diamond anvil cell are now capable of reaching pressures comparable to those at the center of the Earth (~365 GPa), however the estimated temperatures at these conditions (thought to be ~6000-7000 K [Saxena et al., 1994; Williams et al., 1987]) remain a difficult experimental objective. Passage of a shock front through a material results in considerable heating, however.

One can understand the origin of heating upon shock compression quite simply. As shown in the left-hand panel of Figure 2.1, for a reversible (isentropic) process the thermodynamic work done upon compression from an initial state (P_0, V_0) to a state (P_1, V_1) is defined as the integral under the *P-V* curve. Shock compression, however, represents an *irreversible* thermodynamic process. This implies generation of entropy (S), providing an additional contribution to the total change in internal energy such that

$$E_H - E_0 = \int_H -PdV + \int_H TdS \qquad (2.1)$$

where the subscripts *'H'* and *'0'* represent the Hugoniot (shock) state and the initial state, respectively. The second term on the right in equation 2.1 represents the 'extra' energy due to entropy production which is converted to heat through dissipative processes. This is illustrated in the right-hand panel of Figure 2.1. For a shock process, passage from an initial state (P_0, V_0) to a final state (P_H, V_H) is described by a chord joining these states, referred to as a 'Rayleigh line'. The total change in internal energy is then given by the area beneath the Rayleigh line, which is defined by the area of the triangle $P_H V_H V_0$, such that

$$E_H - E_0 = \frac{1}{2}\left(P_H + P_0\right)\left(V_0 - V_H\right) \qquad (2.2)$$

Indeed, equation 2.2 can be obtained by simple arguments dictated by conservation of energy, as demonstrated in appendix A. The presence of 'waste heat' signifies that temperature rises upon shock compression such that the Hugoniot is always at higher temperature than an isentrope at a particular pressure.

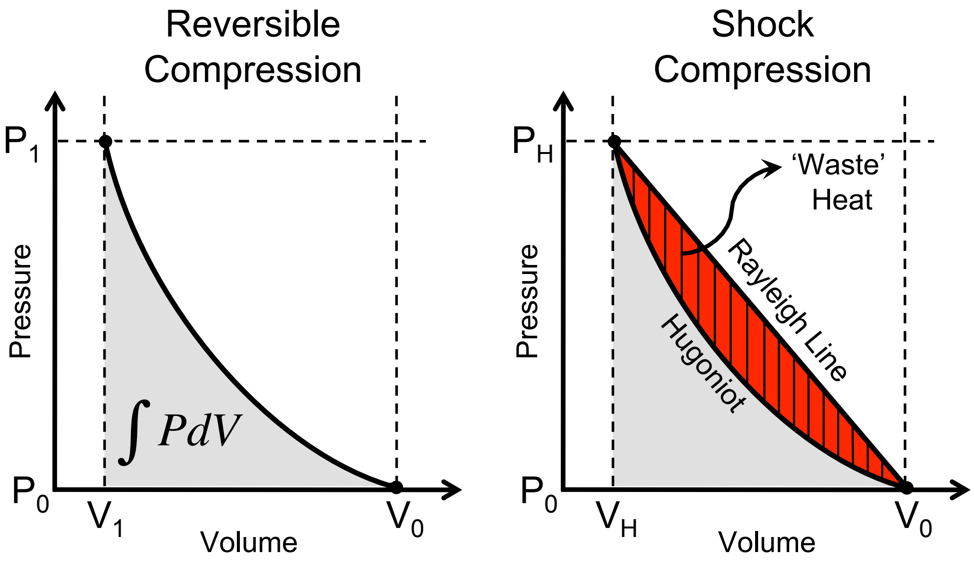

FIGURE 2.1. For a reversible process, the change in internal energy is given by integral beneath the P-V curve (left). Shock compression (right) is irreversible such that the change in internal energy is given by the area under the chord, resulting in 'waste heat' which raises the temperature of the sample. Here, the Hugoniot and isentrope are taken to be approximately equal.

In most geologic media, temperatures of several thousand Kelvin are achieved by shock compression to pressures characteristic of the terrestrial mantle while stronger shocks can easily match conditions expected to occur in giant impact events [Canup *et al.*, 2001; Melosh, 1990]. In many cases, the temperatures achieved upon shock compression actually exceed those of direct relevance to planetary studies, in which case, accurate characterization of the shock-temperature is necessary to compare laboratory results to nature.

Determination of absolute temperature is made possible by the fact that all bodies of finite temperature emit with a spectral radiance characteristic of their thermal state. For experimental measurement of shock temperatures, we relate temperature to spectral radiance by Planck's law

$$L(\lambda,T) = \varepsilon(\lambda)\frac{2hc^2}{\lambda^5}\frac{1}{e^{hc/\lambda kT} - 1} \tag{2.3}$$

where *h*, *c* and *k* are Planck's constant, the speed of light and Boltzmann's constant, respectively, λ is the wavelength and *T* is the temperature of the body. We assume grey-body behavior in which the pre-factor, *ε*, is approximated as a wavelength-independent emissivity, given by Kirchhoff's law as

$$\varepsilon(t) = 1 - R(t) \tag{2.4}$$

where *R(t)* is the reflectivity of the sample at time *t*, measured separately, as described below[1]. Empirically, it is found that most oxides of geophysical interest have low optical reflectivity in the solid state; however, high reflectivity in the molten state results in a larger correction to the measured intensities, *L*.

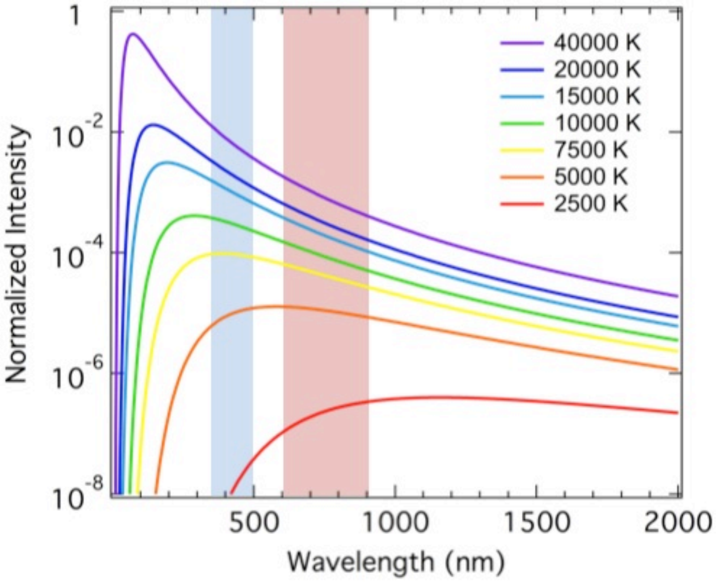

FIGURE 2.2. Intensity of self-emission as a function of wavelength for a range of temperatures characteristic of laser-driven shock experiments as given by Planck's law (eqn. 2.3). In these studies, self-emission is observed in the wavelength regions denoted by the shaded bands.

Most experiments presented here employ decaying shock waves in which the pressure and temperature decrease continuously in time as the shock propagates through the sample. A given experiment may thus sample a range of temperature spanning several orders of magnitude. As shown in Figure 2.2, above, this implies that the intensity of the thermal emission will vary by orders of magnitude over the ~10 nsec duration of a given experiment. A temperature measurement diagnostic must then have adequate sensitivity to observe low-intensity emission from 'cool' samples but high enough dynamic range to avoid saturation for high-temperature experiments. The following sections outline how this is achieved, describing the experimental configuration used to capture and record the thermal emission from shocked samples as well as the calibration techniques used to relate the observed intensities with absolute temperatures.

STREAKED OPTICAL PYROMETRY: EXPERIMENTAL CONFIGURATION

A complete description of the optical path for the streaked optical pyrometer (SOP) at the Janus laser facility is given in appendix B. Because the pyrometer and velocity interferometry system (VISAR) observe the sample simultaneously, a common collection objective-assembly focuses the interferometer probe-beam onto the sample,

---

[1] Equation 2.4 applies to an opaque material, appropriate for these experiments (in which transmission is taken to be zero).

and collects and collimates the returning signal along with the thermal emission (Fig. B.1). The lens assembly is approximately f/3, with a focal length of 146 mm and a lens aperture of 5 cm. Both diagnostics share a common optical path that conveys light from the vacuum chamber in which the sample resides to an optical table located across the room. A 45-degree dichroic beamsplitter (labeled DBS in Figure B.1) centered at 532 nm separates the VISAR probe beam from the wavelengths measured by the pyrometer (shown by the colored bands in Figure 2.2 and, as measured, in Figure 2.4). Two holographic notch filters (N1, N2) are used in collimated portions of the pyrometer beam-path for additional rejection of the VISAR signal and a set of calibrated neutral-density filters can be applied to accommodate intense signals without saturating the camera. A black box encloses the entire pyrometry system beyond the beamsplitter to mitigate contamination of the signal by stray light that does not come down the optical path. Inside the enclosure the thermal emission is focused onto a Hamamatsu C7700 streak camera by means of several 1 meter focal-length achromatic lenses (L1-L5) and two cylindrical lenses (500 mm plano-concave, CL1, and 100 mm plano-convex, CL2) that serve to compress the image of the sample perpendicular to the opening (slit) aperture of the camera. The resulting magnification is a factor of ~8 along the detector aperture, resulting in a spatial resolution of ~12 μm/pixel across the sample. The magnification, alignment and focus are checked prior to a given experiment by placing a grid of known spacing in the target plane and imaging the grid onto the detector.

Temporal resolution is achieved by virtue of the use of the streak camera – a sophisticated detector that images a line across the width of the sample and electronically ‘streaks’ that line across a detector (CCD) during the course of the experiment. The thermal emission emitted at early time is thus recorded on one edge of the detector while thermal emission at later times is recorded on the subsequent rows of pixels. The resulting record is spatially-resolved in one dimension and temporally resolved in the other such that the number of counts recorded on a given pixel corresponds to the intensity at a given position on the sample at a given time. Temporal resolution is determined by the sweep rate and the aperture of the camera and is typically ~100 ps. Under optimal conditions the apparent precision may be as good as 20-60 ps, corresponding to 1-3 pixels.

TECHNIQUES FOR ABSOLUTE CALIBRATION

CALIBRATION USING A SOURCE OF KNOWN SPECTRAL RADIANCE

Absolute temperatures are obtained from the streak records by calibration against a known standard. The first method of calibration relies on comparison to a NIST-traceable Tungsten ribbon filament of known spectral radiance (Optronics Laboratories, Model OL550, serial number IR-472). The calibration routine described here is similar to that developed by Miller *et al.* [2007] for the pyrometry system at the OMEGA laser facility at the University of Rochester, NY, with modifications appropriate to the Janus facility.

The method can be understood by considering the path from sample to detector and the efficiency of each element in the system at transfering light of a given wavelength downstream. The number of counts, *I(T(t))*, ultimately recorded on the detector at a given time is proportional to the spectral radiance of the sample, *L(λ,T)*, given by equation 2.3 [2]. The emitted intensity is modulated along the way, however, by the spectral response of the pyrometry system and also by a number of adjustable parameters which are determined by the experimenter. Because, for most experiments, we do not separate the spectral bandwidth into individual channels, the SOP measures spectrally integrated 'brightness temperature' such that the measured intensity is related to the sample's spectral radiance by a relation of the form

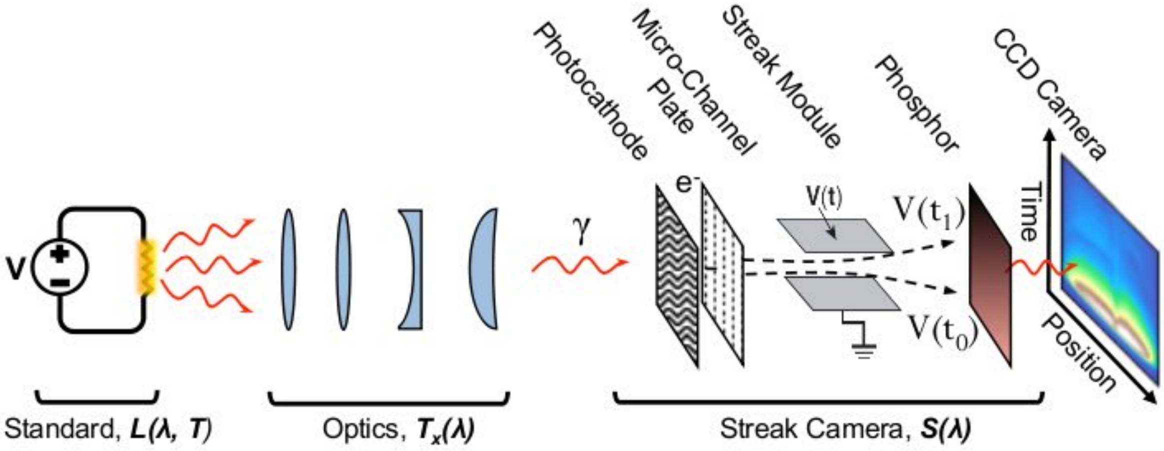

FIGURE 2.3. A graphical representation of the terms in equation 2.5. *L(λ,T)* is the spectral radiance from the sample. This is collected over a specific solid angle defined by the first optic. $T_x(\lambda)$ is the transfer function of the optical path. *S(λ)* is the percent efficiency of the streak camera photocathode which converts incident photons to electrons. The electronic signal is amplified by a microchannel plate and accelerated through a ramped potential which results in a time-dependent variation in their path, sweeping the signal across a phosphor screen upon which they are incident. The phosphor remits photons which are read by a CCD, resulting in a spatially and temporally resolved record of the thermal emission.

$$I(T) \propto C \cdot P_{System} \int_{\lambda} L(\lambda,T) \cdot T_x(\lambda) \cdot S(\lambda) d\lambda \qquad (2.5)$$

Here, $T_x(\lambda)$ is the optical transfer function of the system, *S(λ)* is the efficiency of the photocathode in the streak camera, *C* represents constant system parameters and P_{system} represents the user-defined set of adjustable system parameters. $T_x(\lambda)$ was determined by measuring the transmissive characteristics of each optical element using a Perkin-Elmer Lambda 9 Spectrophotometer[3]. The resulting function is multiplied by the efficiency of the photocathode (provided specifically for this unit by the manufacturers' calibration report[4]) to determine the response illustrated in Figure 2.4. The values outside the integral can be treated as coefficients which are independent of wavelength. The term *C* includes the solid angle of collection of the VISAR objective (how many photons are collected for a given radiance) and the area on the sample mapped to a single pixel (a function of magnification). These values do not change unless the optical path is altered. P_{system}

---

[2] *L(λ, T)* has units $J/sr{\cdot}m^3{\cdot}sec$ such that the units of *C* in equation 2.5 are $I/L{\cdot}\lambda$.

[3] Lambda 9 Specification Manual, Perkin Elmer Corp., Norwalk, CT, 06859-0010.

[4] High Dynamic Range Streak Camera C7700 Instruction Manual and Test Report, Ver.1.3, 2006.7, 6660-401-02, Hamamatsu Photonic Systems, Bridgewater, N.J., 08807-0910.

represents a set of adjustable parameters which may change from one experiment to the next. These include the voltage across the camera's micro-channel plate (gain), the detector's opening aperture, CCD exposure time and streak length. The influence of each of these parameters on the number of observed counts is calibrated individually using the same tungsten ribbon filament and the influence on the measured intensity is given in Figure B.2 (appendix B).

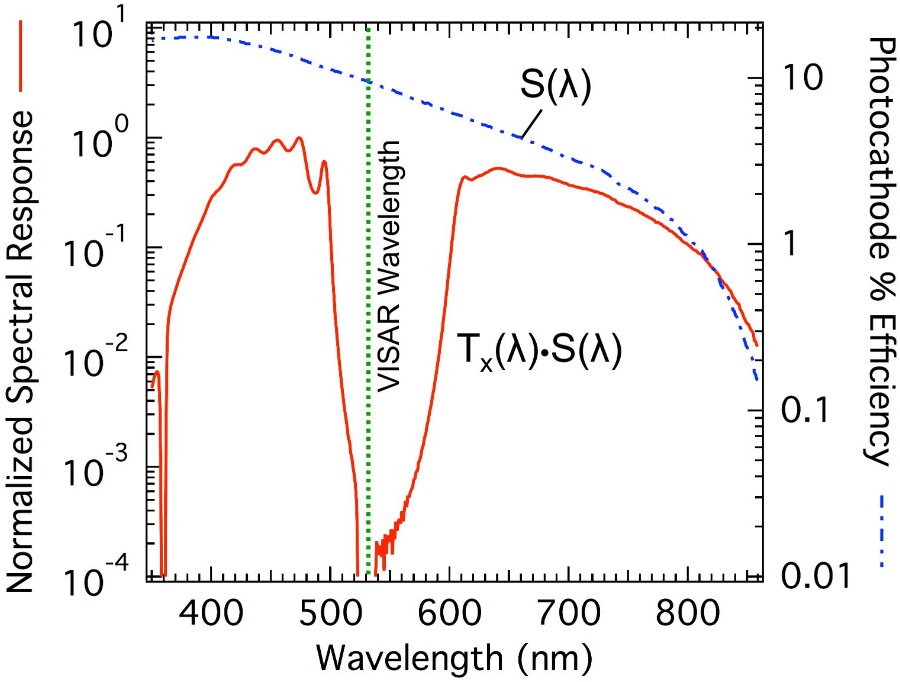

FIGURE 2.4. Lower trace: Normalized spectral response of the pyrometer, $T_x(\lambda)S(\lambda)$, showing sensitivity as a function of wavelength after losses incurred through the optical path and photocathode of the streak camera. The gap between 500 and 600 nm is caused by the dichroic beamsplitter that separates the VISAR signal at 532 nm. Upper trace: $S(\lambda)$, the percent efficiency of the streak camera photocathode.

During the calibration process, the Tungsten ribbon filament is placed in the sample chamber at the target plane and imaged onto the SOP camera. Because the lamp is a continuous source, the streak camera exposure was gated using a mechanical shutter operated with a 1 msec opening time and synchronized with the camera trigger. This ameliorates contamination from the 're-sweep' which occurs in the camera as the ramped field in the sweep module relaxes back to zero after the sweep and hence prevents the phosphor from being re-exposed by light which is still incident on the slit at late time. This configuration permits the measured intensity to be recorded for various combinations of adjustable parameters. It must be noted, however that the Tungsten filament is not sufficiently bright to yield acceptable signal-to-noise for sweep lengths on nanosecond timescales. Calibrations were thus carried out using microsecond sweeps and the intensities were then scaled by the ratio of the 'dwell time', defined as the time that each pixel 'sees' the sample during the sweep. Dwell time is given as $(W_{Slit}/\Delta x_{Slit})\cdot(1/\eta)$ where W_{Slit} is the slit width (the opening aperture of the camera), Δx_{Slit} is the dimension of a pixel at the slit and η is the sweep rate in pixels/nsec. As shown in appendix B, the relation between measured intensity and sweep rate is empirically found to be linear for the sweeps used in these experiments.

The spectral response shown in Figure 2.4 was also tested using the Tungsten ribbon filament. This was done by inserting color-glass filters in collimated regions of the beampath to isolate portions of the spectrum and verifying that the relative integrated intensities were consistent with those predicted by the measured transfer function. This provided some assurance that the efficiency curve (*S(λ))* for the photocathode was accurate since this could not be easily determined independently.

The Tungsten ribbon filament has a known spectral radiance, *L(λ,T)*, when operated at the NIST-specified voltage and current (5 V and 15 Amps) and thus defines a point in temperature-intensity space for a specific combination of camera settings. In order to develop a practical relationship for temperature *vs*. intensity based on this single datum, two techniques were tested. In the first case, the integral in equation 2.5 was solved numerically as a function of temperature and for a fixed set of adjustable parameters characteristic of our experiments. The number of counts expected on the detector was assumed to be proportional to the numerical solution matching the known point determined with the calibration lamp. For a given temperature, the proportionality is given as the ratio of the solutions to equation 2.5, relative to the number of counts measured for the lamp's calibrated temperature (2550 K). The resulting relationship for T *vs.* I (Figure 2.5) is well fit by an equation of the form

$$T = \frac{T_0}{\ln\left(1 + A/I\right)} \tag{2.6}$$

where T_0 and A are fitting constants and I is the measured intensity after background subtraction and correction for emissivity. Given T_0 and A, temperature can be simply calculated for any experiment that uses the same combination of adjustable parameters.

Another technique for arriving at equation 2.6 is outlined by Miller *et al.* [2007] and is based on the assumption that the wavelength dependence of the SOP is well approximated by a δ-function at the centroid in wavelength of the product of the integrand in equation 2.5. This assumption is based on the fact that the spectral band of the SOP is relatively narrow and is integrated over its entirety to obtain a brightness temperature. Under this assumption, T_0 can be understood as a 'characteristic temperature' associated with the centroid wavelength defining the δ-function and A is a function of the system parameters that were defined above as C and P_{System}.

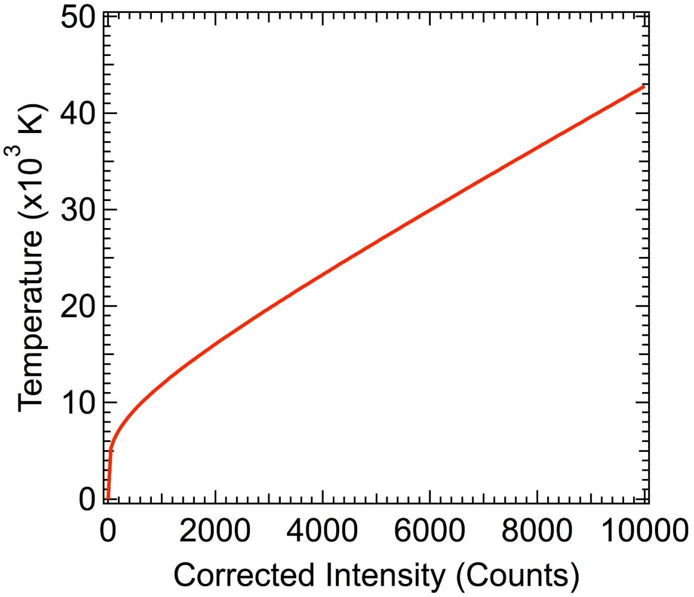

FIGURE 2.5. Example of experimentally-determined temperature-intensity relationship described by equation 2.6.

While the calibration method outlined here should, in principle, provide a robust foundation for experimental temperature measurements, in reality several practical matters hinder the reliability of temperatures determined in this manner. The first, already mentioned, is that the calibration lamp has a characteristic temperature of 2550 K however this is too dim to be detected using sweep lengths characteristic of our experiments and hence below the detection limit for realistic combinations of experimental parameters. The apparent linear scaling of intensity with sweep speed seems to justifiy scaling calibration results at longer sweep speeds to experimental timescales. Nonetheless, a standard with a characteristic temperature comparable to those achieved in shocked samples would be preferable.

As mentioned, the adjustable parameters are calibrated individually to quantify their effect on measured intensity (Appendix B, Figure B2). Unfortunately, attempts to correlate experimental data taken with different combinations of adjustable parameters gives discrepant results (see Chapter 4). This suggests that the effects of changing system settings are coupled such that simple normalizations cannot be applied to compare data taken, for example, with different gain and sweep speed since the correction for one affects the other. Finally, because the calibration relationship is sensitive to the optical transfer function and because it is the spectrally integrated intensity that is recorded, small changes to the optical path between calibration and experiment can have potentially disastrous results. This could include vignetting from a misaligned optical element or replacement of an optical element with another that has different transmission characteristics. Full calibration using the Tungsten filament is also quite time-consuming and is not easily done on a routine basis, particularly at the OMEGA facility where access to the target chamber is limited due to the experimental schedule and operational logistics.

Since the issues described here present several potential drawbacks, a straightforward in-situ calibration method based on an α-SiO_2 (quartz) standard was developed that avoids these concerns.

Relative Calibration Using an α-SiO_2 Standard

Relative calibration against a known material is a simple and effective method of obtaining absolute temperatures for laser-shock experiments. Comparison to quartz allows in-situ calibration (even simultaneously with another sample) and has the advantage of providing a more straightforward means of correlating data taken during different experimental campaigns. Comparison of data taken months or years apart is not straightforward using the Tungsten filmament calibration since intervening changes in laboratory setup and pyrometer configuration must be taken into account.

The method of calibration using α-SiO_2 relies on the fact that the EOS has been previously measured [Lyzenga *et al.*, 1983; Hicks *et al.*, 2006; Knudson *et al.*, 2009]. VISAR measurements of shock velocity are thus sufficient to identify the corresponding Hugoniot temperature. Windows of quartz are prepared in an identical manner to the sample materials and placed adjacent to the sample for one or several experiments in a given campaign. This is illustrated as shown in Figure 2.6. Velocity and thermal emission are recorded simultaneously for both samples (as shown on the right). Since the quartz thermal emission can be correlated directly with a known temperature, the temperature *vs*. intensity relationship is defined by a single shot. Furthermore, for a decaying shock experiment, the shock traces a segment of the Hugoniot in both the sample and the quartz, permitting a large region of the calibration curve (Figure 2.7) to be fit using equation 2.6 as opposed to the single point reference provided by the Tungsten filament technique.

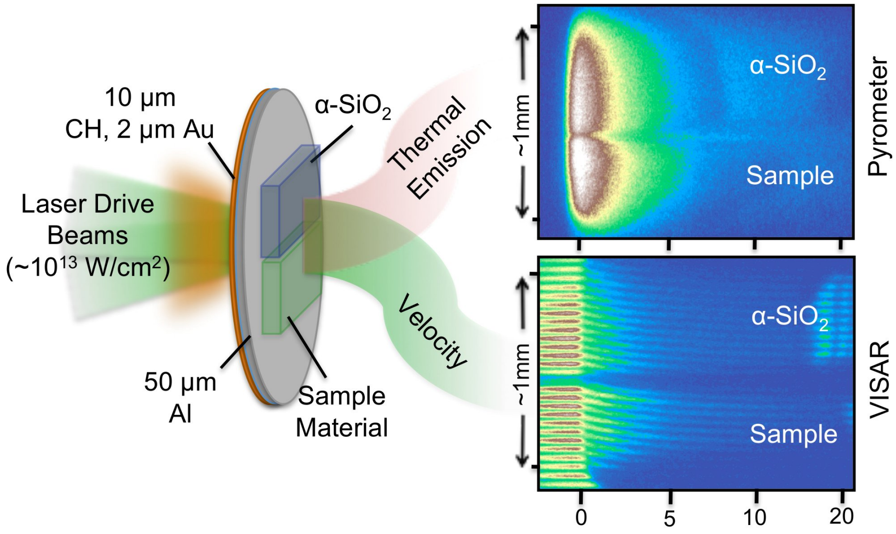

Figure 2.6. Target used for in-situ pyrometry calibration using a *z*-cut (observation along c-axis) α-SiO_2 standard. VISAR and SOP simultaneously observe velocity and spectral radiance, respectively in both materials. The known relationship between velocity and temperature along the α-SiO_2 Hugoniot is then used to develop a calibration (Figure 2.7) that may be applied to calculate temperature in the sample material.

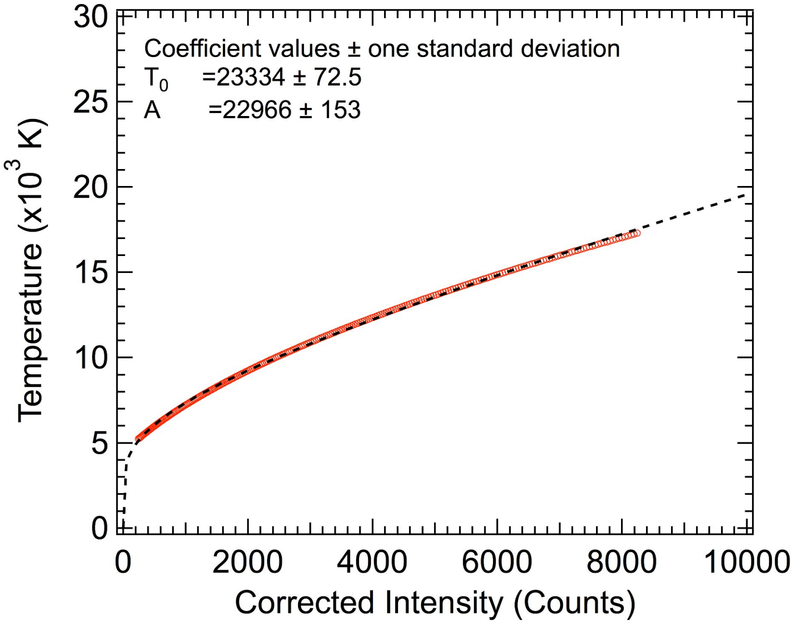

FIGURE 2.7. Example of experimentally-determined temperature-intensity relationship for a decaying shock in α-SiO_2. Red data points illustrate the measured data from a single shot which is then fit with the dashed curve described by equation 2.6. The resulting values of T_0 and A can then be applied to calculate the sample temperature for any other experiments using the same pyrometer configuration and settings.

The method of in-situ calibration using a quartz standard is preferable to the absolute calibration using a tungsten ribbon filament. This technique eliminates systematic errors introduced by the possibility of physical changes to the pyrometry system and ensures that calibration and experiment occur under identical conditions. Should the EOS of quartz be refined in the future, it is also a straightforward task to update results based on this standard. Since quartz is readily available and easily included with samples such as the one shown above, changes in pyrometer setup can be easily calibrated without losing valuable facility time or sacrificing shots which yield data on the sample of interest.

CONTRIBUTIONS TO UNCERTAINTY IN CALCULATED TEMPERATURE

There are many possible contributions to the cumulative error in calculated temperatures. Contributions include the expected signal-to-noise, accuracy of background subtraction and errors incurred by fits or interpolation of the data during processing, including fitting of the calibration curve that determines T_0 and A. These are typically small contributions to the uncertainty for high-quality data (a few percent or less in temperature).

In order to assign the self-emission observed at time t with a given shock velocity or pressure, the data recorded simultaneously by SOP and VISAR (on separate cameras) must be correlated in time. Calibrated timing fiducials are used for this purpose on each camera such that alignment to within ~100 psec is typically possible. If the fiducial is difficult to see or the rise in thermal emission broad enough that the shock breakout is difficult to determine, it can be challenging to achieve this accuracy. To quantify the potential error that could result from poor temporal correlation of the VISAR and SOP datasets, a trial study was done for a quartz calibration shot in which the SOP record was progressively offset from the velocity record. Misalignment of the datasets by 0.5 nsec results in an apparent temperature variation of ~750 K. This is expected to be an extremely conservative upper bound on timing error since this offset is ~five times larger than the typical time-resolution for these studies.

The final, and perhaps most significant source of error stems from the challenge of determining emissivity over the full spectral response of the pyrometer. Temporally evolving, wavelength-dependent changes in the optical properties of the sample may effectively alter the apparent intensity of the thermal emission and lead to erroneous temperature values. As discussed above and in appendix A, emissivity is determined by Kirchhoff's law as 1-*R(t)* by measuring the reflected intensity of the VISAR probe beam at 532 nm. Because light from the probe beam would contaminate the SOP data, this wavelength is selectively removed from the SOP spectral band, as shown in Figure 2.4. Out-of-band variation in sample emissivity is thus not taken into account by this treatment and may result in significant temperature error if the sample undergoes a change in optical properties (see Chapter 5) or if emissivity has significant wavelength-dependence (non greybody behavior).

Although multi-color temperature measurements represent a possible means of avoiding (or reducing) such uncertainty, they are challenging to implement for laser-driven shock experiments. Because laser-driven shocks are capable of achieving pressures many times higher than gas-gun studies, peak temperatures are often many eV. As shown in Figure 2.2, for the highest temperatures the relative energy distribution in the observed bands becomes increasingly less sensitive to temperature variation as the spectrum 'flattens' and thus makes it increasingly difficult to fit the data to a blackbody curve. Although the problem is lessened at lower temperature, the corresponding decrease in intensity is then typically the challenge for fast detectors. The solution is clearly to probe a larger bandwidth, however this is not currently feasible with the streak cameras used for these experiments. Effective 'two-color' temperature measurements have been made using the current system by placing an OG590 color-glass filter over half the field of view. The filter isolates the contributions of the two distinct regions of sensitivity illustrated in Figure 2.4 (λ>590 nm and λ<500 nm) without requiring separate detectors. This technique was not used consistently because the filter must be situated as close to the streak camera aperture as possible where there is very little space available to accommodate it. It is thus physically difficult to position the filter such that the edge does not cast a shadow or obscure the data or the timing fiducial, which enters the streak camera slit on one side. For samples such as the one illustrated in Figure 2.6, two color measurements are also not possible since each side of the field of view samples a different material. Multiple streak cameras may be a viable solution for multi-color pyrometery in the future.

The need to better constrain sample emissivity and understand changes in the optical properties of shock-compressed materials motivated exploratory experiments toward the development of a broadband reflectivity diagnostic.

EXPLORATION OF A TECHNIQUE FOR MEASURING BROADBAND REFLECTIVITY

Reflectivity measurements provide a means of probing the optical properties, hence the electronic structure of condensed matter. A temporally-resolved broadband reflectivity diagnostic using high-intensity, non-linear pumping of a standard optical fiber (Figure 2.8) was successfully demonstrated at the Janus facility. This diagnostic addresses the need for a sufficiently bright white-light source for high energy-density measurements on nanosecond time scales.

In these experiments, a ~10 nsec FWHM pulse from a 532 nm, Q-switched Nd:YAG laser is injected into a 23 meter, 50 μm diameter silica-core multimode fiber. Non-linear optical effects, including stimulated Raman scattering, four-wave mixing and self-phase modulation, lead to spectral broadening of the injected pulse [Dudley *et al.*, 2006; Gordon *et al.,* 1986; Mitschke *et al.*, 1986] and thus to an emission of light spanning a wavelength range of ~350 nm (Fig. 2.9). This white-light (supercontinuum) pulse is reflected off the sample at 27 degree incidence during dynamic loading. The reflected light is collected and spectrally dispersed by a prism, before being directed onto a streak camera. Changes in sample reflectivity can thus be observed simultaneously with VISAR, permitting direct correlation between the supercontinuum, velocity and laser reflectivity data. An additional spectrometer (Acton SpectraPro 2300i) yields a time-integrated record of the reflected supercontinuum spectrum for comparison with the streaked spectrum, and to aid with calibration. In initial tests, a 150 μJ injected pulse was sufficient to recover ~27 μJ at the detector, for an efficiency of approximately 18% which is more than adequate to study material properties over the nanosecond timescales characteristic of laser-driven compression experiments.

This new diagnostic greatly expands upon the frequently-employed single-wavelength measurements using the VISAR probe beam and can serve to constrain wavelength-dependent emissivity over the spectral range observed by the pyrometer described above. This technique is, however, difficult to employ and it is found that the nonlinear processes responsible for generation of the supercontinuum result in significant spectral and temporal structure in the white-light pulse (evident in the left panel of Figure 2.10, before the shock breakout). Future experiments using hollow-core optical fibers may help ‘smooth’ this spectrum by more efficiently mixing optical modes in the length of the fiber. Illumination of the sample by laser-ablation of a separate plastic or metallic foil may also prove a more practical means of studying optical reflectivity. The experiment briefly presented here has demonstrated proof-of-concept, but potentially superior alternative methods have yet to be explored.

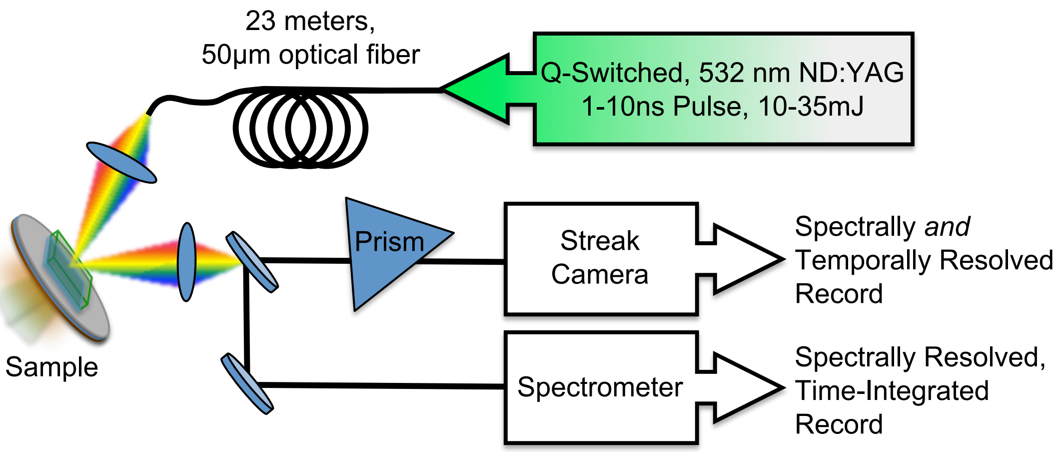

FIGURE 2.8. Supercontinuum generation by nonlinear effects in the optical fiber results in broadband output that is used to make temporally and spectrally-resolved reflectivity measurements of the sample.

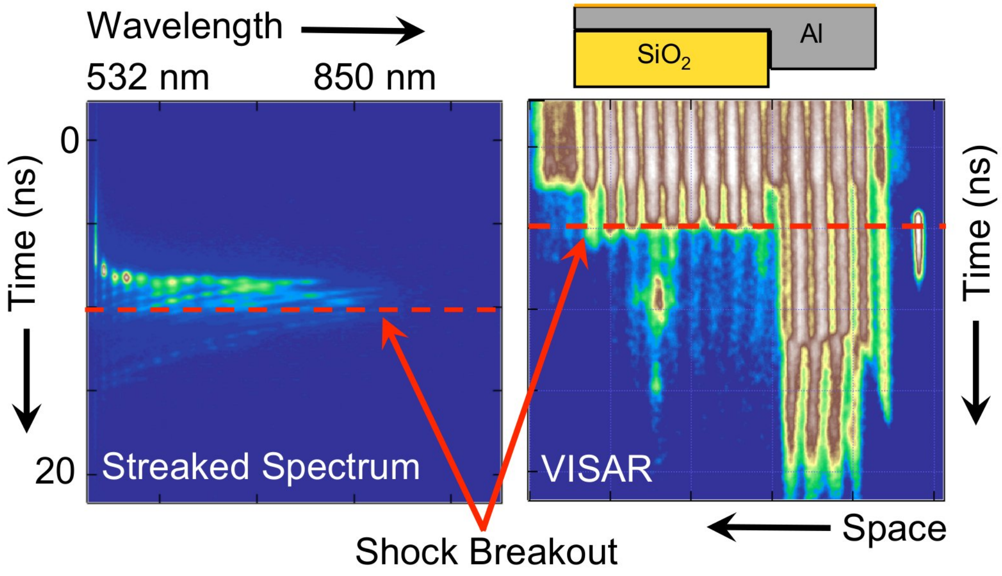

FIGURE 2.9. Example of the spectrum generated with the system described above, reflected from a driven quartz target. Spectral broadening begins from the pump wavelength (532 nm), and extends to an upper limit determined by the sensitivity of the streak camera photocathode near 850-875nm. The streaked spectrum and the VISAR record show that the sample is opaque over ~300 nm bandwidth upon breakout of the shock from the Al step.

CONCLUSIONS

A streaked optical pyrometer has been developed for use at the Janus Laser Facility. Both two-color and spectrally integrated temperature measurements have been successfully demonstrated for shock compression and ramp-loading experiments. Two possible calibration methods have been presented for extraction of absolute temperature from observation of the thermal emission from the sample and a proof-of-concept experiment has been presented to improve measurements of wavelength-dependent emissivity by measurement of broadband reflectivity. These new diagnostic tools represent complementary means of probing the thermal, optical and electronic properties of condensed matter and expand capabilities for conducting robust equation of state experiments at extreme conditions by laser-driven shock.

REFERENCES

Canup, R., Asphaug, E., *Nature*, **412**, 708 (2001).

Dudley, J.M., Genty, G., Coen, S., *Rev. of Modern Physics*, Volume **78**, (2006).

Gordon, J.P, *Optics Letters*, Vol. **11**, No. 10, 662-664 (1986).

Hicks, D.G. *et al.*, *Phys. Rev. Lett.,* **97**, 025502 (2006).

High Dynamic Range Streak Camera C7700 Instruction Manual and Test Report, Ver.1.3, 2006.7, 6660-401-02, Hamamatsu Photonic Systems, Bridgewater, N.J., 08807-0910.

Knudson, M.D., Desjarlais, M.P., *Phys. Rev. Lett.,* **103**, 225501 (2009).

Lambda 9 Specification Manual, Perkin Elmer Corp., Norwalk, CT, 06859-0010.

Luo, S.N., Akins, J.A., Ahrens, T.J., Asimow, P.D*.*, *J. Geophys. Res.*, **109**, B05205 (2004).

Lyzenga, G. A., Ahrens, T. J., Mitchell, A. C., *J. Geophys. Res*., **88**, 2431– 2444 (1983).

Melosh, J., Giant Impacts and the Thermal State of the Early Earth, in Origin of the Earth, H. Newsom and J. Jones, Eds., Oxford U. Press, p 69-83 (1990).

Miller, J.E. *et al*., *Rev. of Sci. Instrum*., **78**, 034903 (2007).

Mitschke, F.M., Mollenauer, L.F., *Optics Letters*, **11**, No. 10, 659-661 (1986).

OL Series 550 Standards of Spectral Radiance with Sapphire Windows, Specification Manual, Optronic Laboratories, Inc., Orlando, FL 32811.

Saxena, S.K., Shen, G., Lazor, P., *Science*, **264** (1994).

Spaulding, D.K., Hicks, D.G., Smith, R.F., Eggert, J.H., McWilliams, R.S., Collins, G.W., Jeanloz, R., *Proceedings: Shock Compression of Condensed Matter*, edited by M. Elert, M.D. Furnish, R. Chau, N. Holmes, and J. Nguyen, American Institute of Physics, 1071 (2007)

UniBlitz Mechanical Shutter and Driver User Manual, Version 1.3, Vincent Associates, Rochester, NY (1995).

Williams, Q., *et al.*, *Science*, **236**, 4798, 181-182 (1987).

SECTION II – EXPERIMENTAL RESULTS: SHOCK TEMPERATURE MEASUREMENTS ON MANTLE COMPOSITIONS

Chapter 3

Shock Compression of SiO_2: Experimental Validation with Quartz and Fused Silica

ABSTRACT

Laser-driven shock compression experiments were carried out on SiO_2 using both amorphous (fused silica) and crystalline (α-quartz) starting materials to validate calibration techniques for streaked optical pyrometry. Based on these results and previous work, a brief discussion is given of the high-pressure phase diagram, optical and thermodynamic properties along the respective shock Hugoniots. Data from this study are found to be in good agreement with previous work which identifies shock melting of fused silica at 4500 K and 70 GPa and melting of crystalline α-quartz at 5000 K and 115 GPa. Based on these observations, a discussion is given regarding the interpretation of anomalies in shock temperature data and the potential utility of optical pyrometry for identifying phase transitions under extreme conditions.

INTRODUCTION

Silica is perhaps the most fundamental 'building block' in planetary science, and is key to defining the thermo-chemical properties of planetary interiors. As one of the most abundant oxides in the Earth, it bonds with Mg, Fe and other elements to form the principle phases of the terrestrial crust and mantle and is likely to play an equally important role in the structure and dynamics of exo-planets.

Because of this importance, polymorphs of SiO_2 including the crystalline (quartz) form and amorphous (fused silica) have been studied extensively at high pressure under both static and dynamic conditions. The first dynamic compression studies were reported as early as 1962 by both Russian and American groups using explosive techniques [Adadurov *et al.*, 1962; Wackerle, 1962]. Shortly thereafter, the significance of naturally occurring high-pressure mineral phases was highlighted by the recognition of stishovite in Arizona's Meteor Crater [Chao *et al.*, 1962], providing one of the first opportunities for the application of shock-compression experiments to the understanding of geophysical phenomena [McQueen *et al.*, 1963]. Since then, a number of studies have mapped out the equation of state of SiO_2 with an abundance of data from static high-pressure techniques up to ~ 200 GPa as well as very recent laser-driven and magnetically accelerated flyer experiments which extend above 1 TPa [Hicks *et al.,* 2005; Knudson *et al.*, 2009]. The phase diagram of SiO_2 is consequently amongst the most fully characterized of the 'simple' oxides, leading to its recent use as reference material for studies of other materials [e.g. this work, Eggert *et al.*, 2008; Barrios *et al.*, 2010]. In reality, the chemical simplicity of SiO_2 belies rather complicated behavior, as it is known that several solid-solid phase transformations occur at low-pressure while other transformations persist in the liquid state as coordination environments evolve with pressure.

This chapter briefly outlines experiments on both fused silica and α-quartz starting materials carried out at the Janus laser facility (Lawrence Livermore National Lab). Measurement of shock temperatures for both polymorphs were used to validate the absolute pyrometry calibration described in the previous chapter by comparison to the existing Hugoniot temperature measurements of Lyzenga *et al.* [1983] and Hicks *et al.* [2006]. These studies were intended to test the performance and sensitivity of the SOP diagnostic and as a benchmark for subsequent experiments on other compositions. An introduction to the optical and thermodynamic properties of shocked SiO_2 is also given (partly from the current studies and partly from previous work) as these properties mirror the behavior of the Mg-silicate and Mg-oxide compositions presented in the subsequent chapters and serve as a reference for comparison of compositional end-member behavior. Finally, a discussion is given regarding the manifestation of phase transitions in shock temperature data along with some of the associated physical interpretations. High sensitivity to changes in thermal emission make optical pyrometry ideally suited to identifying a variety of ultra-high pressure transitions that affect the thermal, optical or electronic properties of the sample. An application to the case of shock melting in SiO_2 is presented here.

METHODS

SAMPLE PREPARATION

Samples were prepared from both single-crystal α-SiO_2 as well as fused silica (glass). The single-crystal samples were provided by Meller Optics (Providence, RI) as 2 cm diameter discs oriented with the faces perpendicular to the crystallographic c-axis (optic axis) to optimize optical probe measurements. The discs were polished by Valley Design Corporation (Santa Cruz, CA) to 137 μm thick and coated on both sides with an anti-reflection coating centered at 532 nm for the VISAR probe beam. The discs were diced into 1 mm^2 windows and mounted with Norland UV-curing optical adhesive on a 40-50 μm thick polished Al buffer which was coated on the reverse side with 2 μm of Au and a 10-12 μm polyimide (CH) ablation layer, as shown in Figure A1. The initial density of the single-crystal samples was taken to be 2.65 g/cm^3 (as per supplier's specifications) and the ambient index of refraction to be 1.546 [Vedam and Davis, 1967]. Fused silica samples were prepared in an identical manner and had an initial density of 2.203 g/cm^3 and ambient index of refraction of 1.461 [Malitson, 1965].

EXPERIMENTS

Experiments were carried out on the Janus laser at the Jupiter Laser Facility (Lawrence Livermore National Lab). Decaying shock waves were generated as described in appendix A, by ablation of the thin plastic layer backing the sample. Energies of up to ~ 400 J were delivered in 1-2 nsec pulses at 527 nm. Laser phase-plates ensured spatially uniform illumination and energy deposition for all experiments and were used to generate focused spot sizes of 0.28 and 1 mm^2. The resulting intensities were ~10^{13} W/cm^2.

Standard laser-shock diagnostics were employed, as outlined in appendix A, including velocity interferometry (VISAR) for measurements of shock velocity (U_S) and streaked optical pyrometry (SOP) for observation of self-emission from the sample from which temperature is extracted. Because the primary motivation for performing experiments on SiO_2 was to validate the pyrometer calibration against previous shock temperature measurements, temperatures reported below were extracted using the tungsten ribbon filament absolute calibration technique described in Chapter 2.

The data reported in the following sections represent only a small number of the quartz shots performed (specifically, those used for pyrometry validation). All experimental campaigns at both the Janus and Omega facilities have included additional quartz samples; however, since most of these were intended for relative pyrometry calibration (as described in Chapter 2) the temperatures for most shots were determined by comparison to the data from Hicks *et al.* [2006] and do add further information to the Hugoniot equation of state. The temperatures reported here were thus collected and analyzed independent of previous work.

RESULTS

The use of decaying (unsupported) shock waves allows a continuous segment of the shock Hugoniot to be traced in a single experiment. By measuring the evolution of shock velocity, U_S, pressure, density and internal energy can then be determined from the Rankine-Hugoniot equations (derived in appendix A) if the relationship between U_S and particle velocity, u_p, is known. In this case the previously measured relationship from Hicks *et al.* [2005] was used since the purpose of the experiments was not to measure the equation of state, but rather to compare shock temperature measurements with existing work. If the EOS is unknown *a priori*, it can be determined as will be shown in the following chapters using the impedance matching technique outlined in appendix A. Simultaneous observation of U_S and the intensity of the thermal emission can then be used to construct the pressure-temperature history of the sample and the corresponding *P-T* phase diagram as shown in Figure 3.1.

Because the decaying shock is continuously decreasing in amplitude as it propagates, the states observed at early time in a given experiment are those at the highest temperature and pressure. With time, lower *P-T* states along the Hugoniot are sampled until the shock reaches the sample-vacuum interface. Observations are made throughout the decay or until the reflectivity of the shock front and/or the intensity of the thermal emission reach their respective detection limits. As shown in Figure 3.1, the Hugoniots of both α-quartz and fused silica are seen to decrease smoothly as a function of pressure and temperature until they reach what is interpreted as the equilibrium melting curve, at which point the temperature is seen to rise as pressure continues to decrease. This thermal signature is addressed in detail below.

Temperatures obtained with the absolute calibration are seen to be in good agreement with gas gun and previous laser-driven shock experiments [Lyzenga *et al.*, 1983 and Hicks *et al.*, 2006, respectively], particularly at the lowest temperatures and pressures. This general agreement allows us to conclude that the pyrometry system established at the Janus facility performs as expected and with similar sensitivity to a comparable system at the Omega Laser Facility at the University of Rochester. The good agreement in the range of ~5000-8000 K is also encouraging since the melting curves of numerous materials of interest to planetary science and basic materials science are

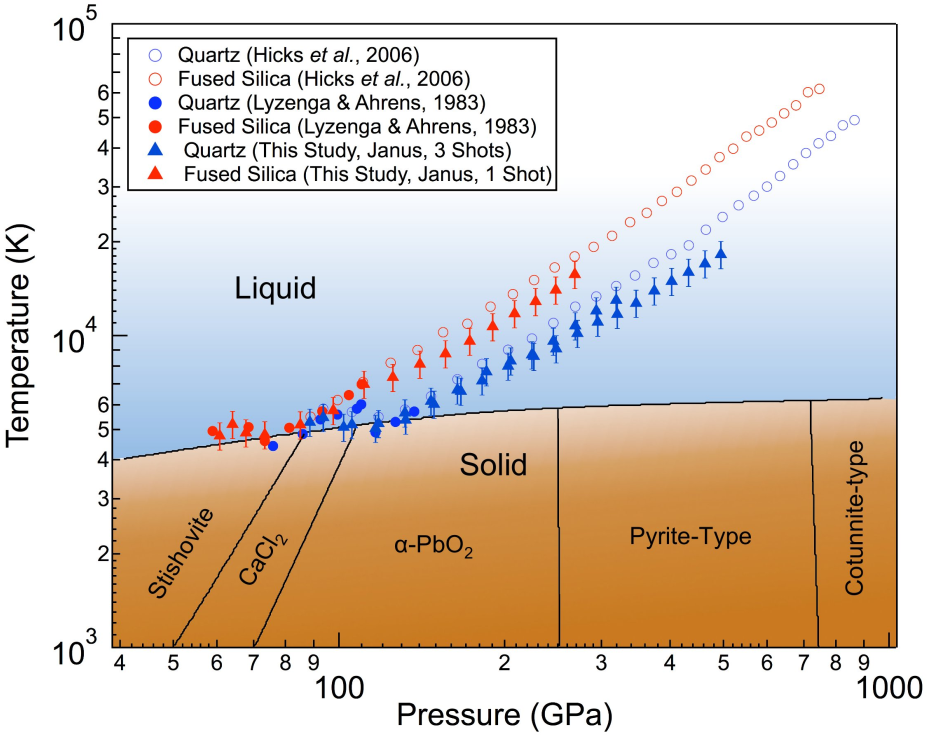

FIGURE 3.1. Pressure temperature phase diagram for SiO_2, showing the Hugoniots for both single-crystal α-SiO_2 (blue, lower temperature) and fused silica (red, higher temperature). Temperatures from the present study are shown as determined using the tungsten ribbon filament calibration technique described in Chapter 2. The absolute calibration results in good agreement with previous studies up to ~ 120 GPa, including measurements made using a different technique (Lyzenga et al., 1983). Differences above ~8000 K indicate reproducibility using the same methods at different laser facilities.

expected to fall roughly within this range at pressures of several Mbar. Sensitivity and accuracy at these temperatures are thus particularly important for explorations of high pressure melt transitions.

Agreement with previous experiments begins to diverge around ~8000 K and grows slightly with increasing temperature. This most likely results from the limited constraints on the slope of the temperature *vs.* intensity relationship (Figure 2.5) determined with the tungsten ribbon filament. This is believed to reflect deviation in the actual response of the pyrometer from the linear scaling assumptions used to calculate the number of counts for temperatures far above that of the calibration lamp. Although it is always possible that the temperatures reported by Hicks *et al.* [2006] are overestimates of the actual Hugoniot temperature, they are in better agreement than the data from this study with two separate EOS models for the SiO_2 Hugoniot (not shown) [Kerley, 1999; More *et al.*, 1988]. The general agreement between the temperature measurements made with the Janus pyrometer and those from previous studies serves to validate the experimental methods and calibration technique. Nonetheless, a calibration standard with a characteristic temperature closer to those achieved in actual experiments would be desirable. For this reason, the alternative quartz calibration technique presented in the previous chapter was favored for the work presented in Chapters 4 and 5.

OPTICAL REFLECTIVITY AND THERMODYNAMIC PROPERTIES

Optical reflectivity at 532 nm wavelength is measured simultaneously with shock velocity and temperature by comparing the reflected intensity of the VISAR probe beam with a reference intensity, as described in appendix A. The results from Janus and a summary of previous interpretations are presented here, not as new work but as a point of reference for the similar but more detailed analyses that follow in the subsequent chapters for which such direct comparisons are not possible. Figure 3.2 compares the present results with the earlier study of Hicks et al. [2006]. Reflectivity is seen to rise sharply with pressure and temperature above ~100 GPa, and to saturate at ~30% in both starting materials. The rise in the reflectivity of the shock front is indicative of the electronic behavior of the sample and is found to be more sensitive to the increase in temperature along the Hugoniot than to the rise in pressure. This can be understood by the fact that copious defects are generated just behind the shock front which act as 'donor levels' whose thermal ionization serves to promote electrons into the conduction band, contributing to high optical reflectivity but also to elevated conductivity. Defects thus act effectively as 'stair steps' across which thermally activated electrons may access previously inaccessible conduction states. As will be shown in the following chapter, a corresponding reduction in the electronic band-gap with pressure can further enhance the promotion of charge carriers.

Early shock studies noted the transformation of dielectrics into semiconductor-like materials with apparently high concentrations of free charge carriers and correspondingly elevated conductivity [Kormer, 1966]. Quantitative estimates of these values can be made from the reflectivity data by application of a coupled semiconductor and Drude-metal model as previously described by Hicks *et al.* [2003] and Celliers *et al.* [2010]. The Drude model defines the conductivity in terms of the carrier concentration, n_e, which is itself a function of temperature, T, and band-gap, E_g. By assuming that the scattering length for an electron is given by the average interatomic distance, according to the Ioffe-Regel criterion [Ioffe and Regel, 1960], the conductivity given by the Drude model can be used to calculate the complex index of refraction, which defines the Fresnel reflectivity of the shock front, R. Since, in practice, R is measured as a function of T and ρ, the reflectivity data can be fit with such a model in which the band-gap, E_g, and carrier concentration, n_e act as fitting parameters. Knowledge of the band-gap at ambient conditions typically provides an additional constraint.

Hicks *et al.* [2006] applied this model to their data (plotted alongside the current study in Figure 3.2) and conclude that conductivity increases by up to three orders of magnitude for a two-fold increase in temperature, reaching metallic-like values of ~1000 Ω-cm^{-1}. Molecular dynamics simulations [Laudernet *et al.*, 2004] are in close agreement with these results. By comparison with previous conductivity measurements from gas gun experiments [Kondo *et al.*, 1981] and as suggested by the sudden rise in R evident in both data sets above the inferred melting point, it is concluded that SiO_2 liquid behaves as a conductive, metallic fluid. This steady rise in electrical conductivity is attributed to a continuous and progressive dissociation of the molecular fluid over a large range of pressure and temperature- moving from what Hicks *et al.* term a 'bonded liquid' to an 'atomic fluid'. This conclusion is reinforced by observation of high specific heat over the same pressure-temperature regime, which the authors argue is indicative of the uptake of energy necessary to gradually break bonds in the liquid state. The data collected at the Janus facility as part of this study are seen to be in good agreement with the previous work and thus support this picture of the transformation of SiO_2 to a conductive liquid state at high pressures and temperatures.

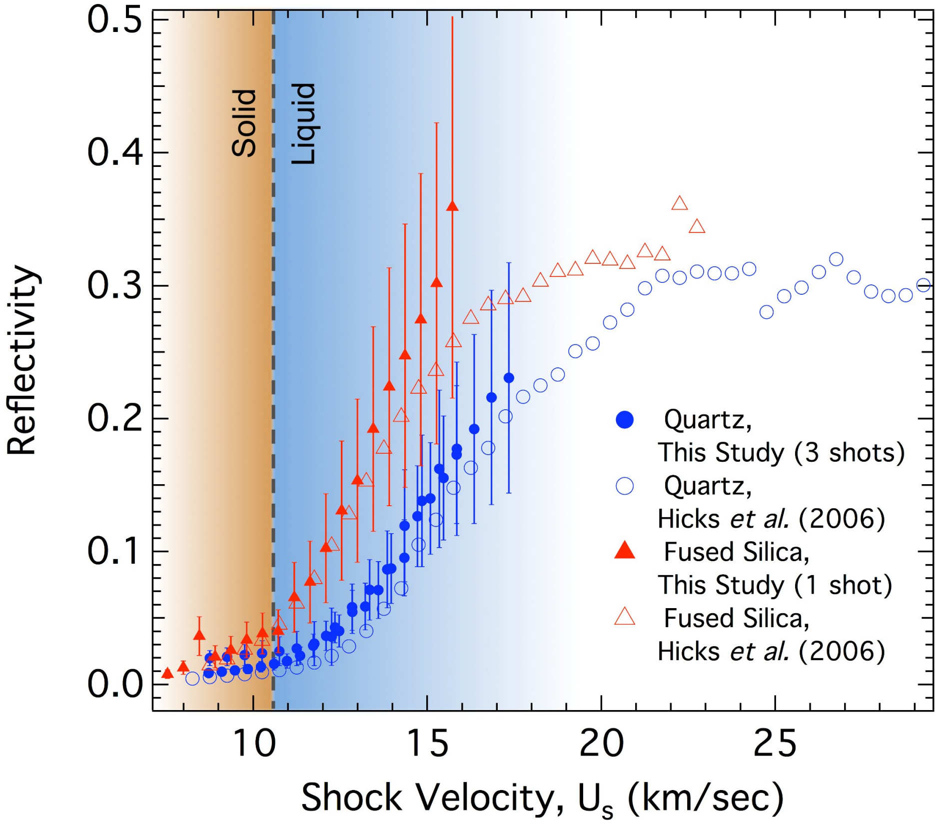

FIGURE 3.2. Optical reflectivity measured at 532 nm for single-crystal α-SiO_2 (quartz) and fused silica starting materials. Open symbols are data collected by Hicks *et al.* [2006] on the Omega laser. Data from this study (closed symbols) were collected on the Janus laser.

The possibility of conductive liquid behavior in silicate materials is of particular interest for geophysical models of magma oceans and the giant impact events that are thought to govern planetary growth and formation of the Earth-Moon system [Canup, 2001]. The occurrence of such a dramatic change in material properties at the ultra-high pressures and temperatures accessed by laser-driven shock underscore the potential utility of the technique for exploring phase transitions under extreme conditions. Experimental observation of such transitions are not always straightforward, however, and conflicting inferences from static and dynamic experiments remain controversial for many materials. In the following sections we turn to a discussion on the manifestation of phase changes in shock data and of the issues which must be considered for careful and accurate interpretation of these data, beginning with the present case: melting in SiO_2.

Investigation of Shock-Melting in SiO_2

The standard ‘observables’ in a shock compression experiment are the kinematic properties dictated by the Rankine-Hugoniot relations and are typically obtained by measurement of the shock or particle velocities. As shown above in Figure 3.2, transition to the liquid state in SiO_2 is accompanied by a rise in optical reflectivity indicative of a change in the electronic behavior of the sample. In this case, there is no measureable effect on the kinematic properties, meaning that this particular transition is only revealed optically. Because streaked optical pyrometry is sensitive to the thermal and optical properties of the material it is an ideal complement to velocity interferometry for revealing phase transitions that are ‘kinematically invisible’ (i.e. result in little or no change to the measured velocities).

Representative data corresponding to that discussed above is shown in Figure 3.3. Quartz and fused silica samples were mounted beside one another. Velocity, temperature and reflectivity were measured simultaneously as a function of time using the decaying shock technique. Although the shock velocity, U_S, is seen to decay smoothly, the same is not true for the intensity of the thermal emission, which rises at the points marked ‘a’ and ‘b’ in the figure. This rise corresponds to the upturn in temperature noted in Figure 3.1 as the Hugoniots of both starting materials reach the equilibrium melting curve.

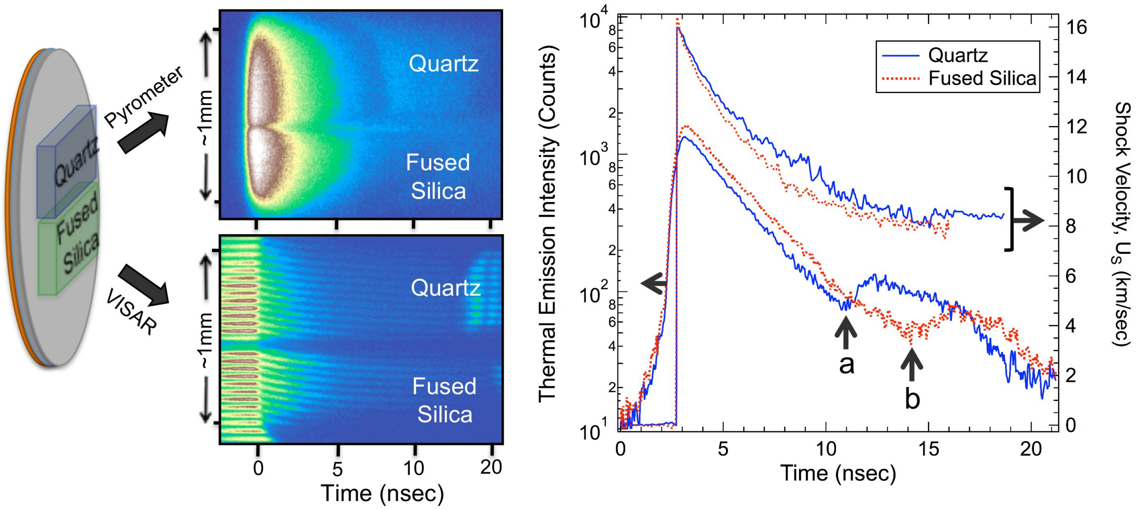

Figure 3.3. Shock velocity and thermal emission profiles corresponding to a portion of the data plotted in Figure 3.1. Quartz and fused silica were shot side-by-side using a decaying shock to probe the Hugoniot of both materials simultaneously. Pyrometry data (top, center) reveals a rise in thermal emission in both samples at the points marked ‘a’ and ‘b’ in the plot. The temperatures and pressures in each material at this point correspond closely with identification of shock melting in previous dynamic studies [Lyzenga *et al.*, 2006; Hicks *et al.*, 2006]. Note: the timescales for the line-outs in the right panel are offset by ~3 ns with respect to the raw data images (center).

Previous studies, including those summarized in Figure 3.1, have interpreted the apparent rise in temperature as indicating the presence of a metastable extension of the solid Hugoniot into the liquid regime- i.e. as superheated solid states generated when equilibrium melting is inhibited by the kinetics of the experiment [Lyzenga *et al.*, 1983]. Sound speed measurements carried out by Chhabildas and Miller [1985] appeared to confirm that the solid phase of SiO_2 persisted to conditions above the expected melting temperature. Although this effect has been reported for other materials [Boness *et al.* 1993, Williamson *et al.*, 1984] and explored extensively to interpret results from gas-gun experiments [Luo *et al.* 2003, 2004], it is still not fully understood. Achieving superheated states experimentally is generally considered difficult because of competition with heterogeneous nucleation at grain boundaries and defects (which tend to lower the energy barrier for melting). Under shock conditions, however, heating rates may be on the order of ~10^{13} K/sec since temperatures of ~5-50,000 K are typical of the results presented here, and this heating occurs in a small fraction of a nanosecond. The response of the sample to this rapid change in temperature will then be limited by homogeneous nucleation. In effect, the rate of heating is faster than the pace at which atoms may rearrange themselves as required for melting. The result is that the Hugoniot follows a trajectory as sketched in Figure 3.4, overshooting the equilibrium melting curve before finally recovering and proceeding in the new (liquid) phase.

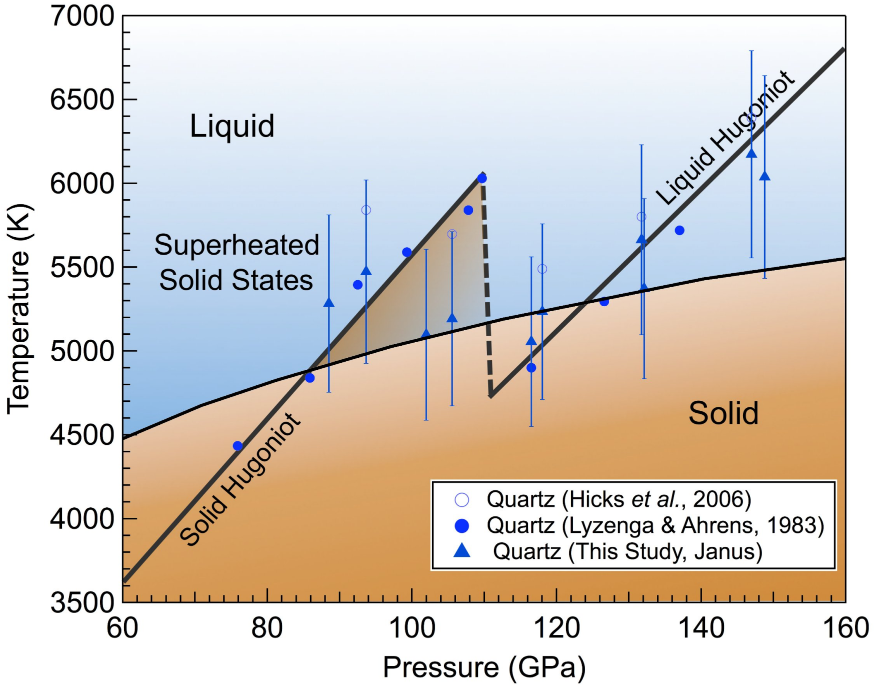

FIGURE 3.4. An enlarged view of Figure 3.1 where the single-crystal α-SiO_2 Hugoniot intersects the solidus. Gas-gun studies proposed that superheated solid states are generated along the Hugoniot due to the relative timescales for melting compared to the shock process [Lyzenga and Ahrens, 1983]. Laser driven shock studies, including the present data, appear to show a similar effect in SiO_2, however this may not be a universal trait for all materials, as discussed in the text and further in Chapter 4.

While superheating appears to provide a satisfying explanation for the shock behaviour of SiO_2 as well as a number of other materials, it is apparently not a universal signature of melt. Very recent decaying shock experiments in diamond, for instance, demonstrate that the temperature remains steady over a wide range of pressure as the Hugoniot reaches the expected melting curve, suggesting near equilibrium behavior through the mixed-phase region despite similar experimental kinetics [Eggert *et al.*, 2009]. It is apparent that the manifestation of phase transitions under shock loading must be carefully examined for different materials such that one may be confident of the actual phase sampled in a particular experiment. Given the rate-dependence of different types of transitions, it is also important to understand the possible kinetic barriers that may arise at the timescales characteristic of shock-compression.

GENERAL INTERPRETATION OF SHOCK-INDUCED PHASE TRANSFORMATIONS

The possibility that phase transformations might occur under shock compression was suggested in the early 1940's although the first systematic experimental study (investigating phase transitions in Fe) was not published until 1956 [Bancroft *et al.*, 1956; Duvall *et al.*, 1977]. As laboratory shock techniques were developed and improved, experiments were carried out which recovered small amounts of diamond from shock-compressed graphite [DeCarli, Jamieson, 1961] and stishovite from SiO_2 [DeCarli, Milton, 1965]. These results proved that stable high-pressure phases can and do form on the timescales of laboratory shock experiments. This possibility was not met with easy acceptance by researchers who had examined some of the same phenomena under static high-pressure and measured reaction rates orders of magnitude longer than the timescale of a shock. Since then, evidence of mixed-phase regions along the Hugoniot, changes in specific heat characteristic of thermodynamic transformation and electronic changes similar to those described above have been uncovered in many studies on a variety of materials. It is now universally accepted that phase transformation can be undergone via shock-compression. It is also recognized, however, that the transition from an ambient to a shocked state at high temperature and pressure must occur along a thermodynamic path determined by relaxation processes inherent to the material and the question of whether the shock probes an equilibrium state is a significant one.

In 1968, Kormer *et al.* reported that shock melting for a number of alkali halides demonstrated near-equilibrium behavior, closely tracking the expected melting curves rather than the metastable Hugoniot, similar to the case of diamond, reported above. At the same time, however, the community was struggling to understand the transformation of SiO_2 to stishovite, which was observed under shock compression [Wackerle, 1962; McQueen *et al.*, 1963] at roughly 4-5 times the pressure at which it had been identified in static experiments [Stishov *et al.* 1961]. Given these apparent contradictions, under what circumstances can the results of dynamic experiments be compared to those obtained using other techniques? The answer to this question appears to depend primarily on the type of transition considered and the pressure-temperature regime in which it occurs.

For transitions in which little or no ionic redistribution is necessary, high-pressure chemistry may occur quite rapidly (psec timescales) due to the relative ease of changing electronic distributions. In some cases, it is believed the shock may actually accelerate phase transitions by generation of large numbers of defects which act as nucleation sites. Reaction rates up to 10^{14} times greater than at ambient conditions are attributed to this mechanism [Kormer *et al.* 1966; Kormer, 1968; Duvall *et al.*, 1977].

Reconstructive transitions between solid crystalline phases require quite long timescales since the rearrangement of atoms into a new lattice configuration must occur. Such transitions are thus diffusion-limited, which helps explain the fact that the stishovite transition is seen to be overdriven. Care must thus be taken in interpreting segments of the Hugoniot in terms of the equilibrium solid polymorph at a given pressure. Possible exceptions to this rule are believed to include solid-solid transformations that can be achieved by shear alone along a preferred crystallographic axis. An example includes passage from the B1 (NaCl-type) structure to the B2 (CsCl-type) structure in which shear along the <111> plane can accomplish the transition [Jeanloz, 1986]. Coherent shear displacements (martensitic transformation) presumably dominates below the material's elastic limit. Localized shear may promote heterogeneous energy deposition along the shear zones, resulting in heating and potential thermal activation of chemical processes [Grady, 1980]. For most geologic materials, including those presented here, the elastic limit is ~10 GPa. Because laser-driven shocks typically explore pressure-temperature regimes 1-2 orders of magnitude higher than this, yielding is expected to occur uniformly with the material behaving in a fluid-like manner and such complications are avoided.

Under these circumstances, it appears that kinetics play less of a role and allow closer comparison of datasets obtained at different timescales. Indeed, for the case of SiO_2, EOS data collected with nuclear-driven shocks, laboratory explosive or gas-gun techniques, magnetically-driven flyers and laser-driven shocks are seen to be in excellent agreement though their characteristic timescales differ by ~ 4 orders of magnitude (from tens of μsec to ~1 nsec, respectively) [Hicks *et al.*, 2005]. Figure 3.1 and the data presented in the following chapters show similarly good agreement between gas-gun and laser-driven shock results (which differ by approximately one order of magnitude in duration). Together, these comparisons allow us to conclude that although laser-driven shock experiments occur on faster timescales than most other high-pressure techniques, the equation of state measurements obtained in this manner are directly comparable to those obtained using other experimental platforms.

EFFECTS OF MATERIAL TRANSFORMATIONS ON OPTICAL PROPERTIES

Because the primary focus of the present studies is on detecting phase transitions with shock temperature measurements, changes in the properties of the material which affect the optical characteristics of the sample or the emitted thermal radiation are a potential concern. The timescales for achieving thermal equilibrium are widely accepted to be orders of magnitude faster than the temporal resolution of the streaked optical pyrometry system ($\sim 10^{-10}$ sec) since thermal equilibration is achieved principally by phonon-phonon interactions which occur in $\sim 10^{-12}$-10^{-13} sec. Observations support this conclusion based on multi-color Hugoniot temperature measurements which show a Planck-like distribution. It is thus safe to assume that the self-emission sampled by the pyrometer represents thermal equilibrium and thus the actual temperature, even if the material is not in the equilibrium phase at a given temperature and pressure (e.g. in the case of the superheated solid).

The type of thermal signature observed in SiO_2 (Figure 3.3) has been almost universally attributed to melting in previous studies [as reviewed by Luo *et al.*, 2004]; however, as will be shown in the following chapters, similar apparent changes in temperature may occur for cases in which transition of the solidus is implausible. Because changes in the optical properties of the sample may affect the measured thermal emission, it is worth mentioning cases in which this may occur.

Since the temperatures reported here are spectrally integrated over ~ 500 nm (as described in Chapter 2), effects which may alter the total intensity are considered. The optical depth behind a reflecting shock front is expected to be small (~1 μm or less), meaning that measured thermal emission is expected to arise from the shock front itself and not from material far behind the shock which lies off the Hugoniot. Partial transparency of the shock to diffusely propagating radiation from the bulk sample may result in anomalous temperatures (Figure 3.5.A), however this is generally not considered to be the case as the VISAR probe beam provides an indication of the opacity of the shock at a wavelength which is central to the band observed by the SOP. Nonetheless, this possibility has been considered and contributes to the motivation for broadband reflectivity measurements that would capture any wavelength-dependence to the emissivity.

A second (similar) mechanism for anomalous temperature measurements was proposed by Zel'dovich *et al.* [1969a] in which the authors reported measuring brightness temperatures in CsBr which were many times lower than the anticipated values. Their explanation was that the recorded emission came not from the thermally equilibrated sample, but rather from 'cold' electrons which were not in thermal equilibrium with the lattice but which could be excited into the conduction band where they effectively 'screen' the equilibrium radiation from the bulk sample. Such an effect is easiest to achieve in materials with a small band-gap which helps promote excitation of the 'cold' valence electrons. Although the equilibration between the lattice and the electrons occurs by phonon interactions at the rate cited above (~10^{12}-10^{-13} sec), the characteristic time for electron excitation is estimated to be much slower (~10^{-9} sec). This is illustrated in Figure 3.5.B and also summarized by Kormer [1968]. This mechanism has been considered to explain deviations in temperature such as the one shown in Figure 3.3. Presumably such a mechanism would result in a strong deviation from a Planck-like distribution of thermal emission. Notable deviations are not typically reported for multi-color temperature measurements that have observed 'superheating' behavior.

A final effect that is known to occur upon phase transformation and which affects the thermal emission from a heated sample is recalescence. Recalescence is a sudden emission of heat- sometimes a visible glow- caused by the liberation of the latent heat of transformation as a material is cooled through a phase boundary. The phenomenon was seen in metal forging processes as the glow of hot steel was seen to suddenly and visibly change upon cooling. An early and very interesting paper was published by Rosenhain [1908] in which cooling experiments on quartz and fused silica at temperatures below 1000 K are interpreted as revealing at least one polymorphic phase transition indicated by the recalescence effect. The temporal evolution of temperature in these studies are qualitatively identical to that shown in Figure 3.3. Similar effects are also reported for supercooled liquids upon nucleation of crystallization which then causes the temperature of the liquid to rise to the equilibrium freezing point. Although the release of latent heat expected when the Hugoniot reaches the solidus in laser-driven shock experiments may contribute to at least some portion of the observed rise in temperature, it is difficult to disentangle this contribution from the potential kinetic effects ascribed to the superheating mechanism. It is also critical to point out that a decaying shock in the sample does *not* represent a continuous cooling from high temperature and thus a literal comparison to the recalescence effect is likely inappropriate. Nonetheless, because latent heat represents a thermodynamic signature of phase transformation, its potential contribution to shock temperature measurements must be kept in mind.

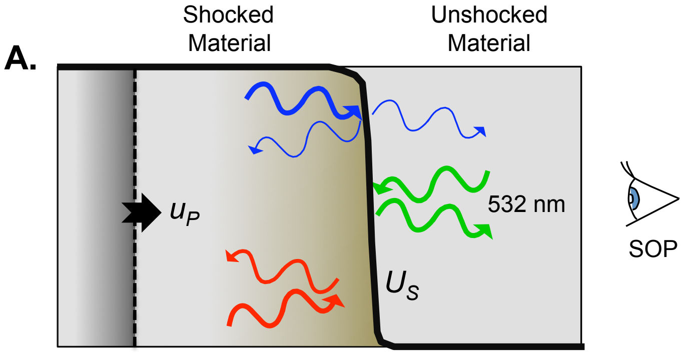

FIGURE 3.5.A Reflectivity (hence emissivity) of the shock front is typically measured at 532 nm. It is assumed that a reflective shock is opaque to thermal emission from the heated material far behind it, however the relative transparency/opacity of the shock to wavelengths away from 532 nm may potentially influence spectrally integrated temperature measurements.

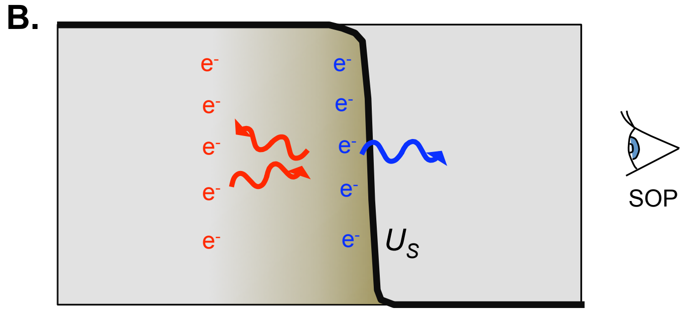

FIGURE 3.5.B A model proposed by Zel'dovich [1969], described in the text, proposes 'screening' of radiation from thermally equilibrated regions of the sample by 'cold' electrons which are not yet in equilibrium with the higher temperature lattice. This scenario results in anomalously low apparent temperatures since emission from the 'cold' electrons dominates the observation.

CONCLUSIONS

This chapter has presented laser-driven shock-compression results on α-quartz and fused silica samples. Absolute temperature measurements were made along the Hugoniots of both starting materials and are seen to be in good agreement with previous studies, validating the technique for absolute pyrometry calibration by comparison to a tungsten ribbon filament standard source. Reflectivity data for both samples reveals evidence that SiO_2 transforms to an electrically conductive liquid state. High-pressure melting is confirmed by streaked optical pyrometry, demonstrating this diagnostic as an extremely useful probe of the thermodynamic and optical properties of materials and a valuable tool for revealing phase transformations that are not necessarily detectable based on measurements of the kinematic properties of the material.

REFERENCES

Adadurov, G.A., Dremin, A.N. , Pershin, S.V., Rodionov, V.N., Ryabinin, Y.N., Shock compression of quartz, *Prikl. Mekh. Fiz.*, **4**, 81-89 (1962).

Akins, J.A., Ahrens, T.J., *Geophys. Res. Lett.*, **29**, 10, 1394 (2002).

Bancroft, D., Peterson, E.L., Minshall, S., *J. Appl. Phys.*, **27**, 291 (1956).

Barrios *et al.*, *Physics of Plasmas*, **17**, 056307 (2010).

Boness, D. A., Brown, J. M., *Proceedings, American Physical Society Shock Compression of Condensed Matter Topical Conference*, American Institute of Physics (1996).

Boness, D. A., Brown, J.M., *Phys. Rev. Lett.*, **71**, 2931– 2934 (1993).

Canup R. M., Asphaug E., *Nature,* **412**, 708–712 (2001).

Celliers, P., Ng, A., Xu, G., Forsman, A., *Phys. Rev. Lett.*, **68**, 15 (1992).

Celliers, P.M. *et al.,Phys. Rev. Lett.*, **104** (May, 2010).

Chao, E.C.T., Fahey, J.J., Littler, J., Milton, D.J., *J. Geophys. Res.*, **67,** 419-421 (1962).

Chhabildas, L.C., Miller, J.M., Release-adiabat measurements in crystalline quartz, *Sandia Rep. SAND85-1092,* Sandia National Laboratory, Albuquerque, NM (1985).

DeCarli, P., Jamieson, J.C., *Science*, **133**, 1821 (1961).

DeCarli, P., Milton, D.J., *Science*, **147**, 144 (1965).

Duvall, G.E., Graham, R.A., *Rev. Modern Phys.*, **49**, 3 (1977).

Eggert *et al.*, *Phys. Rev. Lett.,* **100,** 124503 (2008).

Eggert, J. H. *et al.*, *Nature Physics,* **6**, 40-43 (2009).

Grady, D. E. in *High Pressure Research: Applications in Geophysics*, Manghnani, M. H., Akimoto, S. Eds., Academic Press, Inc., New York (1977).

Grady, D.E., *J. Geophys. Res.*, **85**, B2, 913-924 (1980).

Hicks *et al.*, *Phys. Rev. Lett.*, **91**, 3 (2003).

Hicks, D.G. *et al., Phys. Plasmas,* **12**, 082702 (2005).

Hicks, D.G. *et al.*, *Phys. Rev. Lett.*, **97**, 025502 (2006).

Ioffe, A.F., Regel, A.R., *Prog. Semicond.*, **4**, 237 (1960).

Jeanloz, R., *Shock Waves and Impact Phenomena* (unpublished), (1986).

Kerley, G. I., *Equations of State for Composite Materials*, Albuquerque (1999).

Kondo, K., Ahrens, T.J., *J. Appl. Phys.*, **52**, 5084 (1981).

Kondo, K. *et al.*, *J. Appl. Phys.*, **54**, 8 (1983).

Kormer, S.B., Sinitsyn, M.V., Kirillov, G.A., Popova, L.T., *Zh. Eksp. Teor. Fiz.*, **49**, 135, 1965 [translation: *Sov. Phys. – JETP*, **22**, 97 (1966)].

Kormer, S.B., Usp. Fiz. Nauk, **94**, 641-687, 1964 [translation: *Soviet Phys Uspekhi*, **11**, 2 (1968)].

Laudernet, Y., Clérouin, J., *Phys Rev. B.*, **70**, 165108 (2004).

Luo, S.N. *et al.*, *Geophys. Res. Lett.*, **29**, 14, 1691 (2002).

Luo, S.N. *et al., J. Geophys. Res.*, **108**, B9, 2421 (2003a).

Luo, S.N., Ahrens, T.J., *Appl. Phys. Lett.*, **82**, 12 (2003b).

Luo, S.N. *et al.*, *Phys. Earth and Planetary Int.,*143–144, 369–386 (2004).

Luo, S.N. *et al.*, *J. Geophys. Res.*, **109**, B05205 (2004).

Lyzenga, G.A., Ahrens, T.J., *J. Geophys. Res.*, **88**, B3, 2431-2444 (1983).

Malitson, I.H., *J. Opt. Soc. Am.,* **55**, 10, 1205 (1965).

Marsh, S.P., ed., *LASL Shock Hugoniot Data*, University of California Press, Berkeley (1980).

McQueen, R.G., Fritz, J.N., Marsh, S.P., *J. Geophys. Res.*, **68**, 2319-2322 (1963).

More, R. M., Warren, K. H., Young, D. A., Zimmerman, G. B., *Phys. Fluids,* **31**, 3059 (1988).

Panero, W.R., Benedetti, L.R., Jeanloz, R., *J. Geophys. Res.,* **108**, B1, 2015 (2003).

Rosenhain, W., *Observations on Recalescence Curves*, National Physical Laboratory, (1908).

Stishov, S.M., Popova, S.V., New dense polymorphic modification of silica, *Geokh.*, **10**, 837-839 (1961).

Vedam, K., Davis, T.A., *J. Opt. Soc. Am.,* **57**, 1140 (1967).

Wackerle, J., *J. Appl. Phys.*, **33**, 3 (1962).

Williamson, S., Morou, G., Li, J.C.M., *Phys. Rev. Lett.*, **52**, 26 (1984).

Zel'dovich, Ya. B., Kormer, S.B., Urlin, V.D., *Zh. Eksp. Teor. Fiz.*, **55**, 1631-1639, 1968 [translation: *Soviet Phys.- JETP*, 28, 5 (1969a)].

Zel'dovich, Ya. B., Raizer, Yu. P., *Annu. Rev. Fluid Mech.*, 1, 385-412 (1969b).

Chapter 4
Shock Compression of Single-Crystal MgO

ABSTRACT

Magnesium Oxide (MgO) is a major mineral phase in the Earth's lower mantle and an important ceramic for industrial applications. Despite it being one of the 'simplest' binary oxides, its high-pressure behavior has been a subject of controversy for nearly 20 years with experiment and theory reaching widely discrepant conclusions. This chapter presents the results of laser-driven shock compression studies that span the Hugoniot from ~300 GPa to ~1500 GPa and reveal two transitions in the material. The possibility that these correspond to the long-predicted B1-B2 solid-solid transition and melting along the Hugoniot is discussed. The present data place a definitive upper bound on equilibrium melting and demonstrate that band-gap closure results in a metallic liquid state above ~600 GPa and 13,000 K. In addition, the present data extend the Hugoniot equation of state to 640 GPa.

INTRODUCTION

The high-pressure behaviour of MgO is of critical importance to planetary science as magnesium and oxygen are thought to be the two most abundant elements in the Earth's mantle. In the Earth, dissociation of $(Mg,Fe)_2SiO_4$ to perovskite ($MgSiO_3$) and periclase (MgO) is thought to be the cause of the seismic discontinuity observed at 660 km depth, while in the deepest mantle, uptake of Fe as magnesiowüstite $(Mg_x,Fe_{x-1})O$ is expected to play a fundamental role in moderating chemical processes across the core-mantle boundary.

Because MgO is the simplest oxide with a rocksalt (B1) structure, it has been the subject of numerous experimental and theoretical studies and often used as a proxy for the behaviour of other oxides and silicates. This apparent simplicity, however, masks its duplicitous nature since experiment and theory have thus far failed to converge on the high-pressure equation of state. It is, in many respects, *because* of its simplicity that it remains a challenging subject – the B1 structure results in highly ionic Mg-O bonds, making it isoelectronic with a noble gas (Ne), hence favoring an extremely large pressure-temperature stability field. Consequently, it has been predicted to remain a wide-gap insulator with low-compressibility and high melting temperature to very high pressure [Oganov *et al.*, 2003; Umemoto *et al.*, 2006; Belonoshko *et al.*, 2010]. Previous experimental work has demonstrated the stability of the B1 phase to at least 227 GPa under static high-pressure [Duffy *et al.*, 1995] making it one of the least polymorphic solids known and one of the reasons that it is a favorable choice as an experimental pressure standard [Speziale *et al.,* 2001; Wu *et al.*, 2008]. Meanwhile, the stability of MgO to high temperatures makes experimental exploration of the melting curve difficult; only two static high-pressure studies have been conducted below 35 GPa [Zerr and Boehler, 1994; Zhang *et al.,* 2008] and are seen to be in disagreement (Figure 4.1).

Several dynamic studies have been carried out, providing a surprisingly large number of Hugoniot data points up to ~ 200 GPa. [Vassiliou *et al.*, 1981; Svendsen *et al.*, 1987; Zhang *et al.*, 2008; Duffy *et al.*, 1995; Marsh, 1980]. Although the study by Svendsen *et al.* included temperature measurements, shock melting was not observed. This has left the high-pressure melting curve poorly constrained by experiment and thus in the hands of theorists who have applied a number of differing techniques to attempt to resolve this challenging problem.

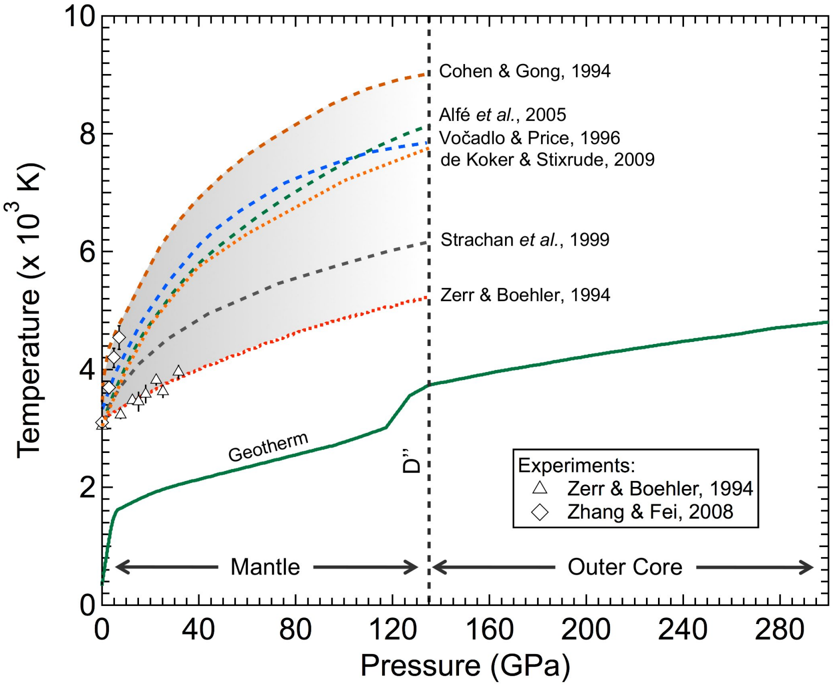

FIGURE 4.1. Experimental and theoretical techniques have thus far failed to definitively constrain the melting temperature of MgO at terrestrial core-mantle boundary (CMB) conditions (vertical dashed line). The range of published predictions for the MgO melt curve is shown as the shaded grey region. At the CMB, the highest and lowest predictions differ by ~4300 K. Laser-driven shock experiments can constrain these estimates by identifying the intersection of the Hugoniot with the equilibrium melting curve at pressures of several hundred GPa.

Because it is one of the 'simplest' oxides, MgO is more conducive to testing computationally demanding techniques than other, more complicated compositions and has been the subject of much theoretical work. Theoretical approaches have done little, however, to resolve the discrepancies between experimental predictions for the melting temperature of MgO at the core-mantle boundary of the Earth (illustrated above in Figure 4.1). Given the chemical simplicity of MgO, the evident disagreement amongst theoretical techniques would cast doubt on their ability to properly predict the behavior of more complicated oxides (Mg,Fe)O or (Mg,Fe)SiO_3. The most recent computational studies using First-Principles Molecular Dynamics (FPMD) simulations based on Density Functional Theory (DFT) appear to have improved consensus amongst theoretical predictions [e.g., de Koker *et al.*, 2009; Alfé, 2005; Tangney and Scandolo, 2009]. This new work increasingly points to a systematic underestimation of the melting temperature by Zerr and Boehler [1994]. It is clear, however, that further experimental constraints are called for at higher pressure to validate or reject the theoretical predictions and to constrain the inputs for geodynamic models with any certainty. Though the expectations for melting of MgO at high pressure differ widely, there is consensus that the solid is stable to temperatures well above that of the terrestrial geotherm. Knowledge of the melting temperature remains a critical parameter for planetary modeling, despite this, since viscosity models often scale with homologous temperature (T/T_M) where T_M is the actual melting temperature [Weertman and Weertman, 1975]. Models of chemical differentiation of the early mantle (even if it occurs at temperature above the mantle solidus) thus depend on knowing the end-member melting temperatures of the constituents.

Laser-driven shock compression provides a means of accessing the necessary conditions to test predicted material behaviour and indeed, identification of shock melting has been one of the primary motivations of the work presented here. This chapter presents the compiled results from an extended shock-wave study of MgO and discusses the possible observation of two phase transitions along the Hugoniot at ~450 and ~600 GPa. Possible mechanisms for these transitions are discussed, including correlation with the B1-B2 structural transformation in the solid and the likelihood of shock melting. Interpretations based on the implications of the thermodynamic and optical properties of the material over a wide range of pressure and temperature are given and it is shown that the liquid is metallic due to band-gap closure above ~600 GPa.

METHODS

SAMPLE PREPARATION

Targets were prepared from synthetic single-crystal samples of <100> oriented MgO, prepared by MTI corporation. The samples were greater than 99.9% pure with an initial density at ambient conditions of 3.584 g/cm^3 and ambient index of refraction of 1.743. Samples were polished to 300 μm thick and cut into 1 mm^2 windows which were then treated with a 532 nm anti-reflection optical coating for laser interferometry measurements. The windows were mounted with a thin layer (<5 μm) of transparent, Norland UV-curing optical adhesive on a 50 μm thick polished Al buffer which was coated on the reverse side with 2 μm of Au and a 10-12 μm CH ablator layer, as shown in Figure A1. Targets used to measure the equation of state had a 32 μm, anti-reflection coated α-SiO_2 window interposed between the sample and the Al buffer as an impedance-matching standard while targets for temperature calibration had a 137 μm-thick, anti-reflection coated α-SiO_2 window mounted beside the sample for comparison of radiance profiles.

EXPERIMENTS

Experiments were carried out at the Janus and OMEGA laser facilities (Lawrence Livermore National Lab and University of Rochester, Laboratory for Laser Energetics). Laser intensities of ~10^{13} W/cm^2 were used to ablate the thin plastic layer backing the target assembly as described in appendix A. At the Janus facility (LLNL), two beams were employed for all experiments with 600 μm diameter spot-size. Delivered energy was ~300-465 J in a 1-2 nsec square pulse. At the Omega facility, 6 beams were used with an 800 μm spot-size, delivering ~850 J in a 1 nsec square pulse. Laser phase-plates ensured spatially uniform illumination and energy deposition for all experiments.

Standard laser-shock diagnostics were employed, as outlined in appendix A, including velocity interferometry (VISAR) for measurements of shock velocity (U_S) and streaked optical pyrometry (SOP) for observation of self-emission from the sample from which temperature is extracted. Temperatures were determined using both the absolute tungsten ribbon filament calibration and the relative α-SiO_2 calibration technique (Chapter 2). Attempts to correlate results from the earliest experiments on MgO relative to later shots based on corrections to the tungsten filament calibration result in poor agreement, as discussed below. Shots from all campaigns in which the α-SiO_2 calibration was employed were found to be in good agreement.

RESULTS

HUGONIOT EQUATION OF STATE DATA FOR MgO

The impedance matching technique used to extract equation of state data for MgO in these experiments is fully described elsewhere [McQueen, 1970; Celliers *et al.*, 2005] and is summarized in appendix A. Hugoniot data for crystalline MgO has previously been reported at pressures up to ~ 200 GPa [Vassiliou *et al.*, 1981; Svendsen *et al.*, 1987; Zhang *et al.*, 2008; Duffy *et al.*, 1995; Marsh, 1980]. With the exception of one, results from all of these studies support the picture that MgO is extremely stable in a single (B1) phase to pressures of many hundreds of GPa. The most recent study by Zhang *et al.* [2008] suggests otherwise, reporting evidence for a transition with a volume change of 1.9% in the vicinity of 170 GPa based on a single U_S-u_p datum and re-analysis of two earlier data points from Vassiliou *et al.*.

For the present study, two EOS points were determined by impedance matching to an α-SiO_2 standard. The Hugoniot of MgO was defined by a weighted linear fit which includes the two points determined by laser-shock and all available single-crystal data from the previous studies. It was found that the data are well-fit by the single linear relation, shown in Figure 4.2. The slight offset suggested by Zhang *et al.* near 170 GPa remains enigmatic and is ignored in the fit, as there is no additional evidence for a phase transition at these pressures but several suggestions that the B1 phase of MgO should remain stable to higher pressures [e.g. Duffy *et al.,* 1995]. Although our results do not rule out the possibility of phase transitions between 200 and 600 GPa, the quality of the single linear fit and the magnitude of the uncertainties in our U_S/u_p data indicate no evidence of any significant discontinuity below 200 GPa. If there *is* a transition with significant volume change between 200 and 600 GPa, the fact that our data fall on the linear extrapolation from the low-pressure data would be purely fortuitous. Pressures and densities in this study were thus determined from this linear U_S-u_p Hugoniot.

TABLE 4.1 – Equation of State Data For MgO From This Study

Starting Material	Shot	ρ_0 (g/cm^3)^a	U_S (km/sec)	u_p (km/sec)	P (GPa)	ρ (g/cc)
Single Crystal	MgO6	3.584	18.82 (0.49)	9.48 (0.42)	639 (30)	18.41 (0.46)
Single Crystal	MgO7	3.584	18.88 (0.49)	8.96 (0.40)	606 (28)	17.98 (0.45)

a. Initial density taken from Robie et al, 1978.

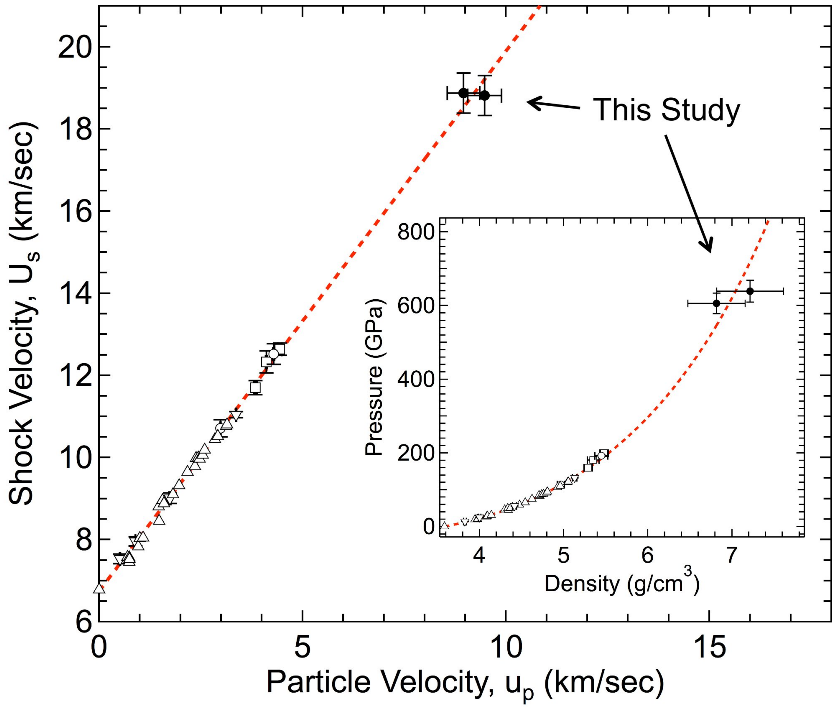

FIGURE 4.2. *Us-Up* Hugoniot data for MgO. Laser-driven shock data from this study (from table 4.1) are plotted as black circles with errors bars at the highest velocities. Data below u_p = 5 km/sec are from gas gun experiments (Marsh, 1980; Vassiliou *et al*., 1981; Svendsen & Ahrens, 1987; Duffy *et al*., 1995; Zhang *et al*., 2008). The dotted line is the fit, defined by $Us = (6.743 \pm 0.070) + (1.316 \pm .017)Up$. Inset: Corresponding pressure-density Hugoniot.

OBSERVATION OF PHASE TRANSITIONS ALONG THE HUGONIOT

Unsupported (decaying) shocks were employed for all experiments, with the exception of those used to measure the equation of state, for which longer laser pulses were used to obtain quasi-steady pressure profiles. As discussed in appendix A, the advantage of decaying shock waves is that they permit traversal of phase boundaries that intersect the shock Hugoniot. In this case, the primary motivation was to identify the temperature at which the Hugoniot intersects the equilibrium melt curve in order to constrain the discrepant predictions from earlier studies.

Due to the wide electronic band-gap, it was difficult to generate a reflecting shock front such that shock velocity (hence pressure) could be observed for any length of time. In experiments with satisfactory (reflecting) VISAR records, shock velocity, U_S was seen to decay smoothly as a function of time. The SOP records, however, reveal two anomalies which were repeatably produced over several experimental campaigns at both the Janus and Omega laser facilities. Representative thermal emission histories are shown in Figure 4.3. At time t = 5.5 nsec, the shock front reaches the sample, having traversed the aluminum buffer separating the drive surface from the material. As time progresses, the amplitude of the shock decreases, resulting in a temperature record which diminishes correspondingly. A subtle and somewhat prolonged deviation in temperature occurs between ~8 and 10 nsec and can be seen as a change in slope in the temperature profiles (labeled ‘2’ in Figure 4.3). An additional, more pronounced anomaly occurs between ~11 and 12.5 nsec, where the temperature rises quite dramatically before resuming a smooth decay until the end of the experiment.

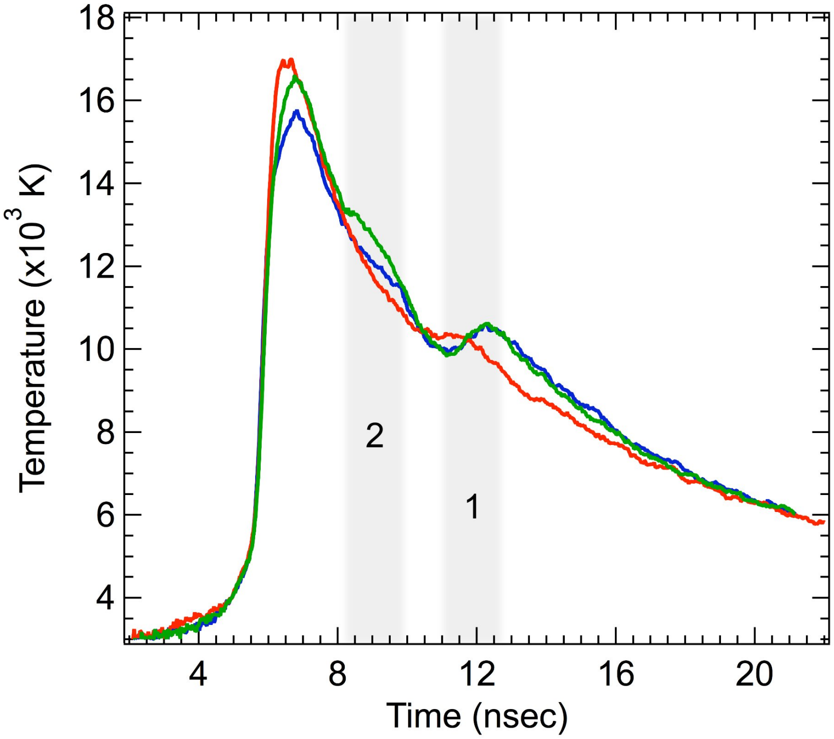

FIGURE 4.3. Examples of three SOP records from shots completed on the Janus laser in August of 2009. Two anomalies, labeled 1 and 2, are consistently observed as temperature decays in time. The most pronounced (1), occurs at ~450 GPa as shown in Figure 4.4, while the more subtle change in slope (2) occurs repeatably between ~580 and 650 GPa. Both anomalies were also confirmed by later experiments on the Omega laser.

Applying the Hugoniot equation of state determined above, pressure is calculated from the Rankine-Hugoniot jump conditions as a function of U_S and can then be correlated with the simultaneously observed temperature to produce a pressure-temperature phase diagram (Figure 4.4).

Although the data collected at the Omega laser continue to pressures of ~1500 GPa, here we plot only the data below 1000 GPa in order to emphasize the relationship of the current study and existing predictions which extend as high as ~600 GPa. There are two major transitions predicted to occur in the vicinity of our observed temperature anomalies. These are the B1-B2 solid-solid structural transformation and equilibrium melting. It is clear from Figure 4.4 that existing predictions are suggestive of potential agreement with these observations. In this case, the discrepancy in temperature between the studies of Belonoshko *et al.* [2010] and de Koker *et al.* [2009] coincidentally suggest that either event in the data might agree well with their respective predictions for the equilibrium melt curve. We carefully examine the implications of either possibility based on our pressure-temperature observations as well as the evolution of the thermodynamic and optical properties which can be extracted from our data.

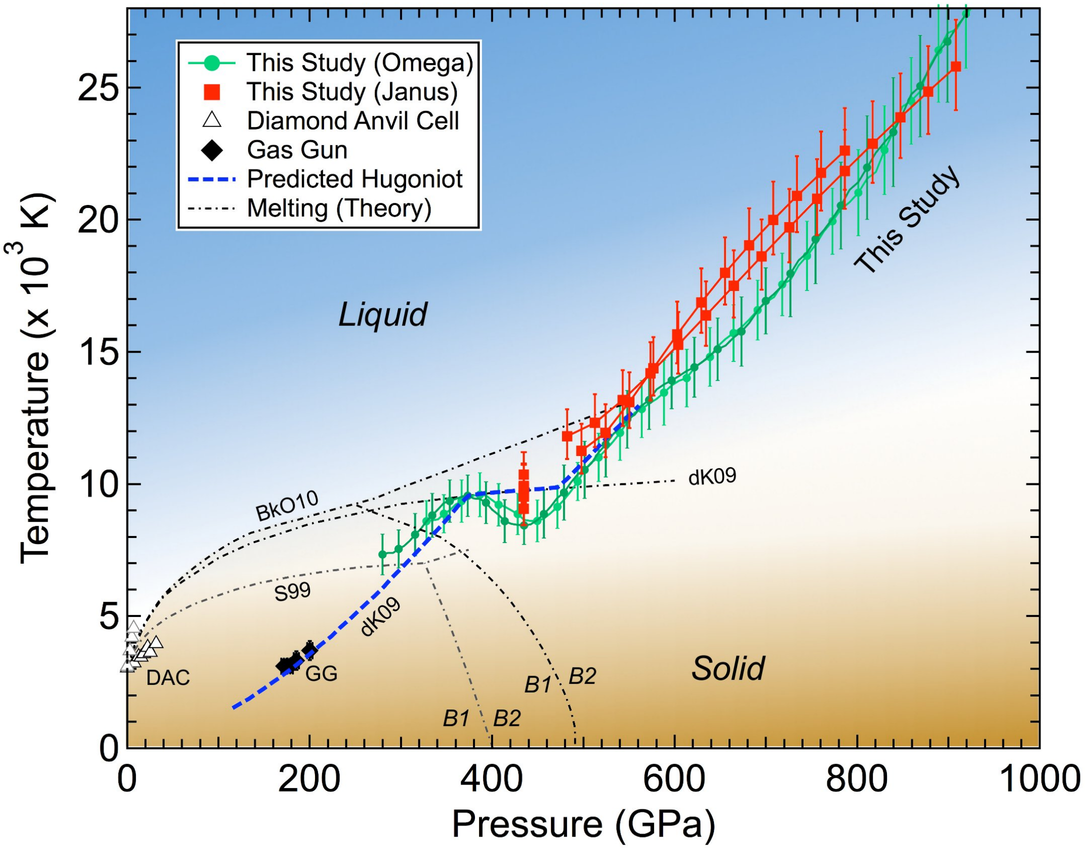

FIGURE 4.4. Pressure-Temperature phase diagram of MgO. The temperature deviation labeled '1' in Figure 4.3 is seen here between ~375 and 450 GPa. The deviation labeled '2' in Figure 4.3 corresponds to the change in slope in the *P-T* Hugoniot, evident here between ~550 and 700 GPa. DAC: Diamond anvil-cell studies [Zerr and Boehler, 1994; Zhang *et al.,* 2008]. GG: Gas Gun results [Svensen & Ahrens, 1987]. BkO10, S99, dK09: Theoretical melt curves and predicted B1-B2 phase boundaries [Belonoskho *et al.*, 2010; Strachan *et al.*, 1999; de Koker *et al.*, 2009, respectively]. Blue dashed line is the predicted Hugoniot [de Koker *et al.*, 2009]. Differences in measured temperature between the Janus and Omega Data are discussed below.

Based on expectations from SiO_2 (Chapter 3), the most straightforward interpretation of our data is to associate the very pronounced change in temperature near 400 GPa with melting. In this case, the deviation in temperature would correspond with the superheating mechanism outlined in the previous chapter and/or with a change in emissivity across the melt transition. If the Hugoniot generates super-heated solid states (near the temperature maximum at 380 GPa), then the data would appear to suggest that the calculated melt curve from de Koker *et al.* only slightly overestimates the actual melting temperature. In addition, their estimate of the latent heat of melting closely describes what would be the offset between the intersection of the solid and liquid segments of the Hugoniot with the equilibrium melt curve. This apparent agreement would make it easy to accept this interpretation without further consideration were it not for the existence of the second (more subtle) anomaly where the *P-T* Hugoniot appears to change slope near 580 GPa. In this case, the data would appear to track the melt slope predicted by Belonoshko *et al.* [2010] between ~580 and 700 GPa. If this second anomaly corresponds to melt, then the first would have to represent a solid-solid transition. Since the B1-B2 transition is predicted to occur at similar pressure, this possibility must be considered.

The B1-B2 transition in MgO corresponds to a change from an NaCl-type (rocksalt) structure with 6-fold coordination to a CsCl-type structure with 8-fold coordination in the solid phase. Similar transitions are known or predicted to occur in a number of ionic crystals, hence the B1-B2 transition in MgO has been the subject of many theoretical studies which have called for its occurrence at pressures ranging anywhere from 205 GPa [Bukowinksi, 1985] to as high as 1050 GPa [Chang and Cohen, 1984]. More recent predictions [Strachan *et al.*, 1999; Drummond *et al.*, 2002; Oganov *et al.*, 2003a, b; Belonoshko *et al.*, 2010] have narrowed the range to ~400-500 GPa at 0 K and all of these studies agree that the transition has a negative Clapeyron slope. Two of these studies generally bracketing the others are plotted in Figure 4.4. The prediction by Strachan *et al.* would suggest that melting along the Hugoniot occurs from the B1 phase, while the higher temperature melting curve of Belonoshko *et al.* would suggest melting from the B2 phase.

In all experiments, temperature is observed over a wider range of phase space than pressure since the sample continues to emit thermal radiation below the critical pressure at which the shock is no longer reflective to the VISAR probe laser. Experiments in which the temperature decays to the pyrometer detection limit (~4000 K) show no further signs of obvious anomalies at pressures below 400 GPa. Conversely, experiments on the Omega laser achieved conditions as high as ~1500 GPa and 50,000 K but no further anomalies were noted between 700 and 1500 GPa. These observations indicate that melting must almost certainly correlate with one of the two anomalies. However, in order to determine a self-consistent interpretion for both, we turn to an examination of the evolution of the optical and thermodynamic properties along the Hugoniot corresponding to the observations already described.

ELECTRONIC PROPERTIES AND OPTICAL REFLECTIVITY

Optical reflectivity at 532 nm was measured simultaneously with U_S and T as described in appendix A. The reflectivity serves as a probe of the electronic behavior of the material and the evolution of reflectivity may be linked to changes in the sample's electrical conductivity and band-gap with a basic semiconductor model. Again, predictions have been made regarding the onset of metallic behavior and indicate that MgO should remain insulating in the solid B2 phase to remarkably high pressure (20.7 TPa, according to Oganov *et al.* [2003]) but should be metallic in the liquid phase with the density of states at the Fermi level increasing with temperature [Karki *et al.*, 2006]. The increased mobility of electrons in the liquid state is suggested to be due to formation of 'interatomic bridges' by the charge-density distributions as the normally spherical distributions around the oxygen atoms are disturbed by atomic disorder in the fluid [*ibid.*]. Based on these expectations we might expect the onset of metallicity to occur as the Hugoniot passes into the liquid state. Distinct changes in optical reflectivity may thus help constrain the actual melt transition. Such behavior would be consistent with previous studies, including the case of SiO_2, described in the previous chapter [Hicks *et al.*, 2006].

The measured optical reflectivity is plotted in Figure 4.5. The low pressure cutoff at ~500 GPa corresponds to the point at which a reflecting shock could no longer be seen in the VISAR and thus the detection limit for *R*, which is a small fraction of a percent. Above 600 GPa, the reflectivity can be seen to rise steadily with pressure, corresponding to an increasing electronic population in the conduction band and a decreasing band-gap.

Conductivity and band-gap analyses were carried out by Peter Celliers (Lawrence Livermore National Laboratory) using the combined semiconductor/Drude metal model outlined in Chapter 2 and fully described by Celliers *et al*. [2010]. This model has been successfully applied to a number of laser-driven shock studies [e.g Hicks *et al*., 2003; Eggert *et al.,* 2009]. Fitting the observed reflectivity yields an estimate of the band-gap and conductivity as a function of pressure. The results are shown in Figure 4.5.

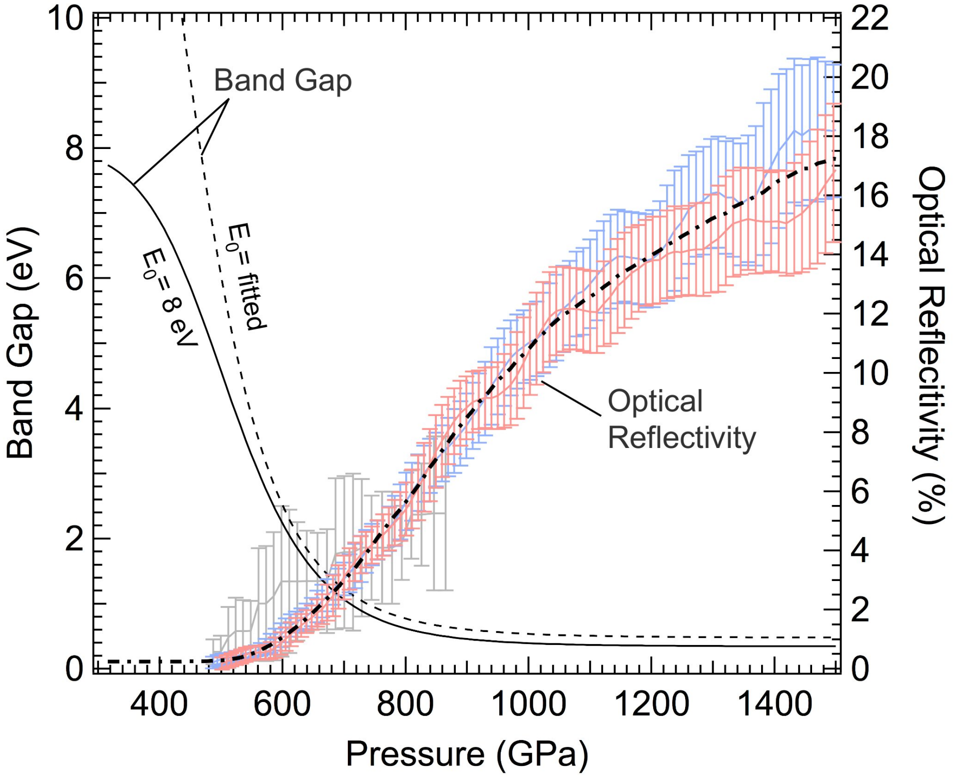

FIGURE 4.5. Optical Reflectivity (right) and band gap (left) as a function of pressure. Compiled optical reflectivity data from Janus are plotted in grey (500-875 GPa). Data from two shots on the Omega laser are plotted in red and blue. The band gap is predicted by a fit to the reflectivity data as described in the text. The dotted line is the band gap resulting from a fit in which the intial gap energy, E_0, is left as a free parameter. The solid line results from fixing the intial band gap at the expected ambient value for the B1 phase, $E_0 = 8$ eV at $P = 0$ [Umemoto *et al.* 2006]. Either model for the band-gap as a function of pressure produces the dash-dot curve through the reflectivity data.

The fit demonstrates that the increase in reflectivity of the shock front can be understood by the onset of metallic-like behavior above ~600 GPa. Below this threshold, the material is found to be insulating and the reflectivity is sufficiently low that it can be explained by bound electron effects which contribute to the complex index of refraction and are thus captured in the Drude formulation introduced above. The associated carrier densities suggested by the model in the the low-reflectivity regime (< 600 GPa) are $\leq 10^{19}$ to 10^{20} cm^{-3}. This matches predicted carrier densities of ~10^{19} cm^{-3} for the B2 phase at comparable pressures and temperatures [Umemoto *et al.,* 2006].

An early study by Ahrens [1966] noted a ~100-fold increase in electrical conductivity (measured directly) in MgO samples shocked to 92 GPa. This was attributed to shock-induced charge defects in the material. In the current study, conductivity is also seen to rise by ~ 2 orders of magnitude, beginning near 500 GPa and reaching calculated values greater than 100 Ω-cm^{-1} by ~700 GPa. In this case, the Drude model suggests thermal activation of charge carriers across an ever shrinking band-gap rather than shock-induced charge defects as the mechanism responsible for generating metallic-like conductivity in the range of 600 GPa and above. The fact that the decrease in band-gap and increase in conductivity implied by the model occur over a range of pressure may indicate an increasing fraction of metallic (hence probably liquid) MgO and a decreasing fraction of insulating (solid) MgO. Whether attributed purely to the electronic state of the sample, partly to the physical state (molten *vs.* solid), or both, the onset of high reflectivity and metallic-like conductivity appears to coincide well with the second anomaly described in the temperature data near 600 GPa.

ESTIMATION OF THERMODYNAMIC PROPERTIES ALONG THE HUGONIOT

Further information can be gleaned by estimation of the isochoric specific heat along the Hugoniot. C_v can be extracted from the slope of the Hugoniot using the measured temperatures from the SOP. The method can be understood by considering that an infinitesimal section of the Hugoniot can be approximated as the sum of an isentropic compression step and an isochoric heating step such that $\Delta E_H \approx \Delta E_S + \Delta E_V$ and $\Delta T_H \approx \Delta T_S + \Delta T_V$ where subsripts *H, S*, and *V* refer to changes along the Hugoniot, isentrope and isochore, respectively. Using the definitions $P = -(\delta E/\delta \mathrm{V})_S$ and $\gamma = -(V/T)(\delta T/\delta \mathrm{V})_S$, we can then write

$$C_v = \left(\frac{\Delta E_H - \Delta E_S}{\Delta T_H - \Delta T_S} \right) \approx \left(\left. \frac{\partial E}{\partial V} \right|_H + P \right) \Big/ \left(\left. \frac{\partial T}{\partial V} \right|_H + \gamma \frac{T}{V} \right) \tag{4.1}$$

All quantities on the right-hand side of equation 4.1 are either measured or calculated directly from the Rankine-Hugoniot jump conditions with the exception of the Gruneisen parameter, γ. Because γ cannot be determined independently from our data, we apply the value estimated by de Koker *et al.* [2009].

Where the trend in temperature reverses near ~380 and ~420 GPa the sign of the derivative *dT/dV* changes suddenly, causing equation 4.1 to diverge. This is not expected to reflect the actual behavior of C_v but rather suggest that the assumptions used in constructing eqn. 4.1 break down for sudden temperature reversals. In Figure 4.6, the calculated values of C_v are plotted from 450 GPa and above, where the temperature begins to increase continuously.

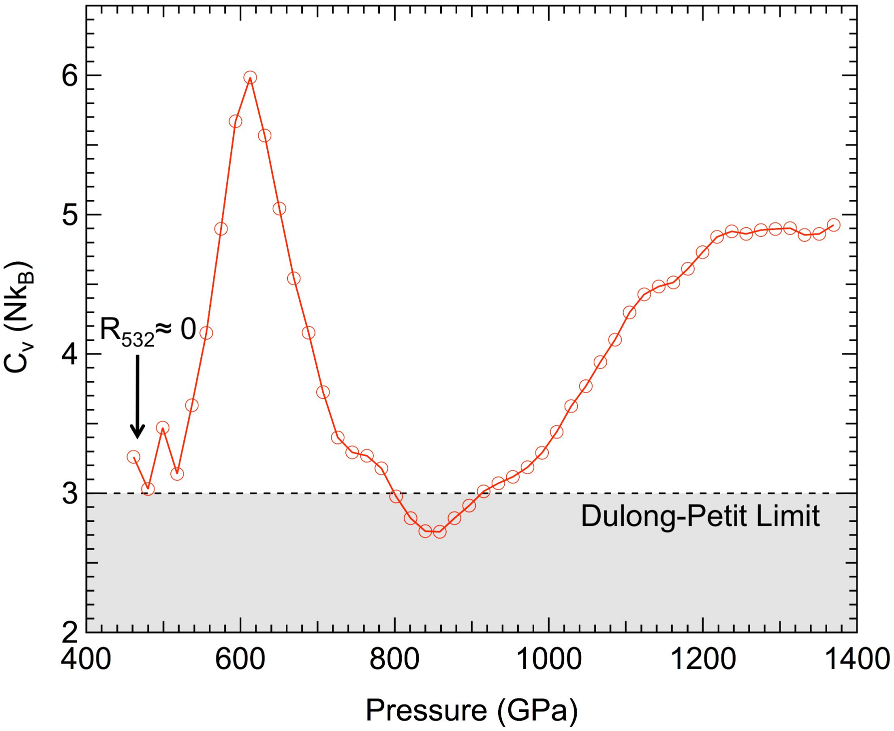

FIGURE 4.6. Average specific heat as a function of pressure along the MgO Hugoniot. Where the shock is reflecting, above ~475 GPa, C_v may be extracted from the slope of the Hugoniot as described Chapter 3. The peak just above 600 GPa suggests a transition consistent with melt along the Hugoniot while the gradual rise in C_v at high pressures may signal changes in bonding in the liquid, possibly associated with formation of an atomic fluid.

The results reveal a distinct peak in specific heat near 600 GPa followed by an approximate recovery of the Dulong-Petit value and then a gradual rise with pressure above ~1000 GPa. Values of specific heat exceeding the Dulong-Petit limit are predicted at high pressure and temperature for MgO as well as for the silicate components in the terrestrial mantle [de Koker *et al.*, 2009; Karki *et al.*, 2006] but a sharp deviation such as the one noted here would appear to be indicative of an energetically intensive phase transition in which the system 'soaks up' energy without a significant increase in temperature (since C_v is classically defined as $C_v=(dE/dT)_v$). This is manifested in Figure 4.4 by the fact that the slope of the *P-T* Hugoniot shallows between ~550 and 700 GPa. This could be indicative of a changing coordination environment in the liquid, as many predictions call for. Hicks *et al.* [2006] report a similar peak in C_v following melting in SiO_2, as well as a similar rise at the highest pressures. For SiO_2, the peak is attributed to the energetics of bond-breaking in the liquid as the material transforms from a 'bonded fluid' state to an 'atomic fluid' state in which bond breaking is essentially complete. The gradual rise in C_v at the highest pressures is likely to be due to an increasing electronic contribution to C_v as the reflectivity and conductivity rise.

Although not entirely unambiguous, these results point to the second, more subtle anomaly in the data as a real thermodynamic transition in MgO, consistent with a gradual change in the nature of the chemical bonding between ~500-700 GPa. The difficulty in interpreting specific heat from the slope of the Hugoniot near the first anomaly does not rule out the existence of elevated values of C_v around 400-450 GPa but does preclude specific conclusions about the thermodynamic nature of that transition.

DISCUSSION

The electronic behavior and specific heat inferred from the reflectivity and temperature data support the conclusion that the material is in a metallic, fluid state above 600 GPa. If the second (more gradual) anomaly represents melting, the Hugoniot would pass from an insulating B2 phase to a conductive liquid phase, consistent with predictions for the behavior of both solid and liquid [Chang and Cohen, 1984; Liu *et al.*, 2010; Karki *et al.*, 2006]. The carrier densities predicted by the Drude model formulation further support this conclusion and agree with predictions for an insulating B2 phase. The peak that occurs in the specific heat between ~500-700 GPa is not entirely unambiguous with regard to distinguishing which anomaly corresponds to melting. While an uptake of latent heat should occur upon melting, the possibility of bond-breaking in the liquid cannot be discounted. If melting does occur near 600 GPa, the lower, more pronounced, transition would need to be explained as a solid-solid transition.

The B1-B2 transition is predicted to result in a volume change, $V/V_0 \sim 4.6$-4.8% [Oganov *et al.*, 2003b; Strachan *et al.*, 1999]. This is somewhat worrisome for the present interpretation since our equation of state data do not suggest any significant volume change between the earlier gas-gun studies and the two points reported here. This could point to error in the data or may indicate that the actual volume change is smaller than predicted and thus not resolved by the fit to U_S-u_p suggested by our two measurements at high pressure. As mentioned above, our data do not definitively rule out the existence of a volume change, though agreement with the single linear fit would be fortuitous if one does occur. At the same time, the relative agreement between the P-T slope of the Hugoniot and the predicted slope of the B1-B2 phase boundary is tantalizing, however interpreting the deviation near 450 GPa as a literal tracking of the phase boundary may be misleading. As discussed in the previous chapter, an apparent rise in temperature may be attributed to kinetic effects and superheating upon melting because of the fast heating rates. It is not immediately evident that a solid-solid transition should result in a similar effect. If, however, the change from 6-fold to 8-fold coordination associated with a B1-B2 transition were to result in a change in the optical properties, an *apparent* deviation in temperature could result from a change in emissivity (ε) . The reflectivity data suggest that deviations from $\varepsilon = 1$ are negligible in the vicinity of the first anomaly in the data but do not necessarily capture changes that might occur away from the 532 nm probe wavelength.

What we can conclude is that the data place a definitive upper bound on equilibrium melting, commensurate with the predictions of Belonoshko *et al.* [2010] and demonstrate that band-gap closure results in a metallic liquid state above ~600 GPa and 13,000K. This indicates that the first anomaly, near 450 GPa occurs between insulating phases. Although this supports the interpretation that the lower-pressure transition corresponds to traversal of the B1-B2 phase boundary (albeit manifested in a somewhat surprising manner), the possibility of melting followed by an initially slow rise in conductivity cannot be definitively ruled out. Additional measurements that may help resolve the nature of the first anomaly include the spectrally-resolved reflectivity measurements introduced in the previous chapter. Further experiments on samples of different initial density (in particular, porous or glass samples) would also permit more extensive exploration of the equilibrium phase boundary and further distinction of gradual changes in liquid structure.

ADDITIONAL JUPITER LASER FACILITY EXPERIMENTS

The earliest campaign in which the SOP was fielded at the Janus facility was also the first in which temperature anomalies were observed and for which reflecting VISAR data was collected for MgO. Because achieving reflecting shocks at the Janus facility proved difficult, experiments were repeated over several subsequent campaigns. These later experiments revealed apparent inconsistencies in the calibration for the initial MgO temperature results and a significant effort was made to understand the apparent difference in the various determinations of the temperature at the first anomaly. It is concluded that the temperatures for the initial Janus experiments with reflecting VISAR traces (plotted above 500 GPa in Figure 4.4) are likely to overestimate temperature along the Hugoniot as a result of corrections which must be applied to the thermal emission data for these first two MgO shots. Comparison of both calibration techniques described in Chapter 2 as well as a number of experiments on other materials taken with different SOP parameters support this conclusion. This has important implications for the analysis of other SOP data taken with varying SOP configurations if data are to be compared across campaigns and motivates the brief discussion that follows here.

Frequent changes were made to the configuration of the SOP during the first campaign, as attempts were made to optimize and understand its performance. Consequently, the variable parameters listed in Chapter 2 were frequently changed from shot to shot, requiring corrections to compare data to the calibration and to subsequent experiments. Corrections for the variable system parameters were determined empirically using the Tungsten ribbon filament and are summarized in appendix B, Figure B2. These describe how the measured intensity scales with variable streak camera sweep speed, gain setting and CCD exposure time. If more than one of these corrections must be applied to a given data-set to extract temperature it is found that the results are in poor agreement with data that do not require such corrections. This indicates coupling between the scaling relationships in Figure B2 that cannot be properly accounted for unless *all* possible combinations of variable parameters are calibrated. Because these corrections directly multiply the measured number of counts in the SOP record, coupling between them quickly leads to incorrect temperatures. This is believed to be the case for the two shots from Janus for which reflecting VISAR records were collected and which are plotted in Figure 4.4 and is expected to explain the offset between the Janus and Omega data.

Based on these results, subsequent campaigns were conducted in a manner so as to avoid unnecessary corrections. This is done by maintaining consistent camera settings throughout a given campaign and regulating intensity levels with ND filters instead of electronic gain. In addition, calibrations have been carried out under identical conditions to the shots whenever possible, which favors the α-SiO_2 calibration technique outlined in Chapter 2.

CONCLUSIONS

Decaying shock experiments were carried out on single-crystal MgO samples over a range of pressure and temperature exceeding 1000 GPa and ~45,000 K. The observations reveal two transitions centered near 400 and 600 GPa. The data appear to constrain earlier discrepant predictions for the high-pressure phase diagram of MgO by placing a definitive upper-bound on equilibrium melting. The likelihood that the lower-pressure transition (near 400 GPa) corresponds either to melting or to traversal of the B1-B2 solid-solid phase boundary has been discussed. Above 600 GPa, MgO is seen to transform from an insulating to a conductive fluid state, with band-gap closure resulting in metallic-like conductivity (~100 Ω-cm^{-1}). These results suggest that magnesiowüstite has a melting temperature roughly twice that of the geotherm at the core-mantle boundary of the Earth and may thus be less likely to contribute to partial melt than previous studies have suggested.

REFERENCES

Aguado, A., Madden, P.A., *Phys. Rev. Lett.*, **94**, 068501 (2005).

Ahrens, T.J., *J. Appl. Phys*., **37**, 2532-2541 (1966).

Alfe, D. *et al.*, *Phys. Rev. B*, **72**, 7 (2005).

Baraffe, I., Chabrier, G., Barman, T., *Astronomy & Astrophysics,* **482**, 315 (2008).

Baraffe, I., Chabrier, G., Barman, T., *Reports on Progress in Physics*, **73** (2010).

Belonoshko, A. B., Arapan, S., Martonak, R., Rosengren, A., *Phys. Rev. B*, **81**, 054110 (2010).

Boness, D.A., Brown, J.M., *Proceedings of the Conference of the American Physical Society, Shock Compression of Condensed Matter*, Seattle, Washington (1996).

Bukowinski, M.S., *J. Geophys. Res.,* **85**, B1 (1980).

Bukowinski, M. S., *Geophys. Res. Lett.,* **12**, 536 (1985).

Celliers, P.M. *et al.*, *Physics of Plasmas,* **11**, L41 (2004).

Celliers, P. M., Collins, G.W., Hicks, D. G. and Eggert, J. H., *J. Appl. Phys.,* **98**, 113529 (2005).

Celliers, P.M. *et al.,Phys. Rev. Lett.*, **104** (May, 2010).

Chang, K.J., Cohen, M.L, *Phys. Rev. B*., **30**, 8 (1984).

Cohen, RE., and Gong, Z., *Phys. Rev. B*, **50**, 12301-12311 (1994).

Cohen, R.E., Weitz, J.S., in *Properties of Earth and Planetary Materials at High Pressure and Temperature*, Geophysical Monograph 101, American Geophysical Union (1998).

Drummond, N. D., Ackland, G. J., *Phys. Rev. B,* **65**, 184104 (2002).

Duffy, T.S., Hemley, R.J., Mao, H.K, *Phys. Rev. Lett.*, **74**, 1371 (1995).

Duffy, T.S, Ahrens, T.J., *J. Geophys. Res.-Solid Earth,* **100**, 529 (1995).

Eggert, J. H. *et al.*, *Nature Physics,* **6**, 40-43 (2009).

Guillot, T., *Annual Review of Earth and Planetary Sciences,* **33**, 493 (2005).

Hicks *et al.*, *Phys. Rev. Lett.*, **91**, 3 (2003).

Hicks, D.G. *et al.*, *Phys. Rev. Lett.*, **97**, 025502 (2006).

Ioffe, A.F., Regel, A.R., *Prog. Semicond.*, **4**, 237 (1960).

Karki, B., Bhattarai, D., Stixrude, L., *Phys. Rev. B*, **73**, 174208 (2006).

Liu Z.J. *et al., Phys. Status Solidi B*, **247**, No. 1, 157–162 (2010).

Luo, S.N. *et al.*, *J. Phys.: Condens. Matter,* **16,** 5435 (2004).

Luo, S.N., Ahrens, T.J., *Physics of the Earth and Planetary Interiors,* 143-44, 369 (2004).

Marsh, S.P., ed., *LASL Shock Hugoniot Data*, University of California Press, Berkeley (1980).

McQueen, R.G., Marsh, S.P, Taylor, J.W., Fritz, J.N, Carter, W.J., in *High-Velocity Impact Phenomena*, edited by R. Kinslow, Academic Press, New York (1970).

Oganov, A.R., Gillan, M.J., Price, G.D., *J. Chem. Phys.*, **118**, 10174 (2003a).

Oganov, A.R., Dorogokupets, P.I., *Physical Review B,* **67**, 11 (2003b).

Robie, R.A., Hemingway, B.S., Fisher, J.R., *U.S. Geological Survey Bulletin*, 1452, 456 pp., (1978).

Schubert, G., Turcotte, D.L., Olsen, P., Mantle Convection in the Earth and Planets, Cambridge University Press, Cambridge (2001).

Speziale, S., *et al., J. Geophs. Res.*, **106**, B1, 515-528 (2001).

Strachan, A., Cagin, T., Goddard, W.A., *Phys. Rev. B*, **60**, 15084 (1999).

Svendsen, B., Ahrens, T.J., *Geophysical Journal of the Royal Astronomical Society* **91**, 667 (1987).

Tangney, P., Scandolo, S., *J. Chem Phys.,* **131**, 124510 (2009).

Umemoto, K., Wentzcovitch, R.M., Allen, P.B., *Science* **311**, 983 (2006).

Valencia, D., O'Connell, R.J., Sasselov, D., *Icarus,* **181**, 545 (2006).

Vocadlo, L. and Price, G.D., *Phys. Chem. Miner.*, **23**, 42 (1996).

Vassiliou, M.S., Ahrens, T.J., *Geophys. Res. Lett.* **8**, 729 (1981).

Weertman, J., Weertman, J.R., *Annu. Rev. Earth Planet. Sci.*, **3**, 293-315 (1975).

Wu, Z. *et al., J. Geophys. Res.*, **113**, B06204 (2008).

Zerr, A., Boehler, R., *Nature*, **371**, 506 (1994).

Zhang, L., Fei, Y.W., *Geophys. Res. Lett.,* **35** (2008).

Zhang, L., Gong, Z.Z., Fei, Y.W., *Journal of Physics and Chemistry of Solids,* **69**, 2344 (2008).

Chapter 5

Shock Compression of $MgSiO_3$: First Observations of a Liquid-Liquid Phase Transition in Silicate Melt

ABSTRACT

The high-pressure material properties of $MgSiO_3$ play a central role in the thermo-chemical and structural evolution of planetary bodies as the primary constituent of the terrestrial mantle and prototypical chondritic composition. In this study we present results from laser-driven shock compression experiments that suggest the presence of an abrupt liquid-liquid phase transition in $MgSiO_3$. The results demonstrate that the melt transforms to a metallic liquid phase with an increase in density of ~10% between 300 and 400 GPa and over a wide range of temperature, suggesting complex liquid chemistry in magmas at multi-Mbar pressures. In addition, the present results extend the Hugoniot equation of state of $MgSiO_3$ single-crystal and glass to 950 GPa and place constraints on the equilibrium melt curve, a subject of longstanding controversy in the geophysical community.

INTRODUCTION

The physical and transport processes of magnesium-silicate liquids are of fundamental importance for accurately describing the geodynamic and petrogenic processes governing the formation and evolution of terrestrial planets [Canup, 2001; Agee 1998]. Perovskite, $(Mg_x, Fe_{1-x})SiO_3$ is thought to be the most prevalent mineral in the Earth's mantle and has been the subject of numerous static high-pressure studies. Many of these have focused on understanding the recently discovered solid-solid transformation from perovskite to post-perovskite [Murakami *et al.*, 2004] and the potential influence on seismic anisotropy at the Earth's core-mantle boundary. Shock wave studies on porous Mg-silicate compositions were first reported by Simakov and Trunin [1973] up to 230 GPa. Several more recent gas-gun studies have refined the Hugoniot equation of state up to similar pressures [Marsh, 1980; Akins *et al.*, 2004; Luo *et al.*, 2004; revisited by Mosenfelder *et al.*, 2009] and although a small handful of these experiments are inferred to have achieved melting, expectations for the liquid equation of state are due almost entirely to theory [e.g. de Koker and Stixrude, 2009, Stixrude *et al.* 2005].

This chapter presents evidence that the Mg end-member, $MgSiO_3$ undergoes a significant phase transition in the liquid state under conditions encountered in extra-solar planetary interiors and in giant impact events. These results demonstrate that complex chemistry persists in magmas (silicate liquids) to extreme conditions (many Mbar and T>1 eV) and introduces the possibility that liquid-liquid phase separation may play an important role in rapid chemical partitioning and convective processes that govern the equilibration of mantle and core in early planetary evolution.

The possible ubiquity of 'polyamorphism'- i.e, the existence of liquid states of the same composition but distinct densities and entropies- has recently been the subject of much discussion, though typically in the context of supercooled materials [McMillan, 2004, 2007; Brazhkin, 1997; Poole *et al*, 1997]. Direct experimental evidence of super-solidus liquid-liquid transitions is, at present, limited to very few cases, most notably that of phosphorous [Katayama, 2000, 2004; Monaco *et al.*, 2003]. Such transitions have been suggested to occur in other materials on the basis of theory [Boates *et al.*, 2009] and indirect experimental evidence such as melting curve maxima [e.g Mukherjee *et al.*, 2007; Ross *et al.*, 2006]. While liquid-liquid transitions have been speculated to occur in silicates and other materials with open tetrahedral structures [Poole *et al.*, 1997; Ohtaka *et al.*, 2004, Saika-Voivod *et al.*, 2001, 2004], they have not previously been observed experimentally. Changes in structure related to increasing coordination in $MgSiO_3$ glass have been documented to a few tens of GPa [Gaudio *et al.*, 2008, Wilding *et al.*, 2004] however the evolution of density at higher pressures has been expected to occur smoothly. The present results demonstrate that this is not the case at extreme pressures and temperatures, and provide the first direct evidence of an abrupt transition to a high-density liquid phase in a silicate melt.

METHODS

SAMPLE PREPARATION

Single-crystal samples were prepared from a natural specimen of colorless Sri Lankan enstatite [Zoysa, 1985] and were cut and polished to form 300 μm thick, $1mm^2$ windows which were then treated with a 532 nm anti-reflection optical coating for laser interferometry measurements. The windows were mounted with a thin layer (<5 μm) of transparent, Norland UV-curing optical adhesive on a 50 μm thick polished Al buffer which was coated on the reverse side with 2 μm of Au and a 10-12 μm CH ablator layer, as shown in Figure A1. Targets used to measure the equation of state had a 32 μm α-SiO_2 window interposed between the sample and the Al buffer as an impedance-matching standard (described below).

Glass samples of similar dimension were identically prepared from two batches of source material. Glass chips from the study of Luo *et al.* [2004], prepared using the techniques described therein (equimolar melting of MgO and SiO_2 powders) were provided by Paul Asimow (Caltech). Glass spheres were prepared by Jean Tangeman using the gas-levitation technique, as described by Wilding *et al.* [2004b], and were provided by Sarah Gaudio (UC Davis). Samples were sliced into plates, polished to a thickness of ~265 μm and treated with an anti-reflection coating centered 532 nm.

ELECTRON MICROPROBE ANALYSIS OF SAMPLE MATERIALS

Chemical analysis of the sample materials was carried out using the Cameca SX-51 microprobe system in the Earth and Planetary Science Department at UC Berkeley. The standards employed were San Carlos Olivine (Mg, Fe), Chesterman Diopside (Si) and Grass Valley anorthite (Al). The synthetic glass samples were compared to the single-crystal composition to ensure that all experiments were performed with samples as close to pure enstatite composition as possible. As shown below in table 5.1, the samples have stoichiometry close to that of the pure Mg end-member in the Enstatite-Ferrosilite system.

TABLE 5.1: Oxide Weight Percents Obtained by Electron Microprobe Analysis

Sample	SiO_2	TiO_2	Al_2O_3	Cr_2O_3	FeO	MnO	MgO	CaO	NiO	Na_2O	Sum
Single-Crystal	56.81	0.02	2.10	0.001	0.42	0.01	38.14	0.12	0.01	0.01	97.641
Glass: Batch 1	61.17	--	0.006	--	0.007	--	39.31	--	--	--	100.49
Glass: Batch 2	60.36	--	0.190	--	0.02	--	40.48	--	--	--	101.05

LASER PARAMETERS

Experiments were carried out at the Janus and OMEGA laser facilities (Lawrence Livermore National Lab and University of Rochester, Laboratory for Laser Energetics). A 1-2 nsec square pulse of intensity ~10^{13} W/cm^2 was used to ablate a thin plastic layer backing the target assembly as described in appendix A. The laser pulses contained ~200-700 J at 527 nm (Janus facility) and ~700-1100 J at 351 nm (Omega facility) to generate a decaying shock in the sample material. Laser phase plates were used to ensure uniform ablation across the sample and hence a spatially uniform shock profile over a circular area 600-800 μm in diameter (at Janus and Omega, respectively).

Finally, Hugoniot equation of state (EOS) data for the high-pressure phase of both glass and single-crystal samples was determined by the impedance matching technique in the manner of Celliers *et al.* [2005] and using an α-SiO_2 standard of known EOS [table 5.2]. Absolute temperatures were determined using the α-SiO_2 calibration technique (Chapter 2).

RESULTS

MANIFESTATION OF A PHASE TRANSITION IN THE LIQUID STATE

Representative data from an experiment on the single-crystal starting material are shown in Figure 5.1. At time $t = 0$, the shock arrives in the sample material, bringing it to an initial high-pressure, high-temperature state. Since the shock is unsupported, shock velocity and thermal emission decrease with time until $t \sim 3$ nsec when both quantities are seen to rise sharply as the Hugoniot traverses what we interpret as a liquid-liquid phase boundary. The rise in U_S (~0.7 km/sec) corresponds to a volumetric change in the material as dictated by the Rankine-Hugoniot relations, while the simultaneous change in thermal emission indicates an apparent change in temperature which we attribute to a possible change in sample emissivity across the transition. An identical transition was repeatably observed in experiments with glass starting materials, where the lower initial density of the glass (2.74 g/cm^3) relative to the single-crystal (3.22 g/cm^3) allows higher temperatures to be achieved for a given shock pressure. Experiments on the glass thus transit the proposed phase boundary at higher P/T conditions and allow us to define the slope, dP/dT. Data from 6 experiments at the Janus facility are plotted in Figure 5.2.

Using the observed change in U_S to determine $\Delta\rho$ along the Hugoniot of the single-crystal starting material, we find that the high-pressure phase is ~7.2 ± 2.6% more dense than the corresponding low-pressure phase, while for the glass, $\Delta\rho = 12 \pm 3.9\%$ (Figure 5.2, inset). Given dP/dT ($=1.55\pm0.68\times10^7$ Pa/K)[1], we can also estimate the latent heat L, and change in entropy ΔS, associated with the transition from the Clausius-Clayperon relationships ($dP/dT=\Delta S/\Delta V$ and $dP/dT=L/T\Delta V$) in which all other quantities are observables. In transiting from the low-pressure to high-pressure phase, we find L=-35.7±14 kJ/mol of atoms and dS=-3.5±1.5 J/mol of atoms·K for the single crystal and L=-92.2±40 kJ/mol of atoms and dS=-5.67±3 J/mol of atoms·K for the glass. Taken together, these observations indicate that with increasing pressure, the Hugoniots of both starting materials pass through an abrupt phase transformation characterized by increased density and decreased entropy.

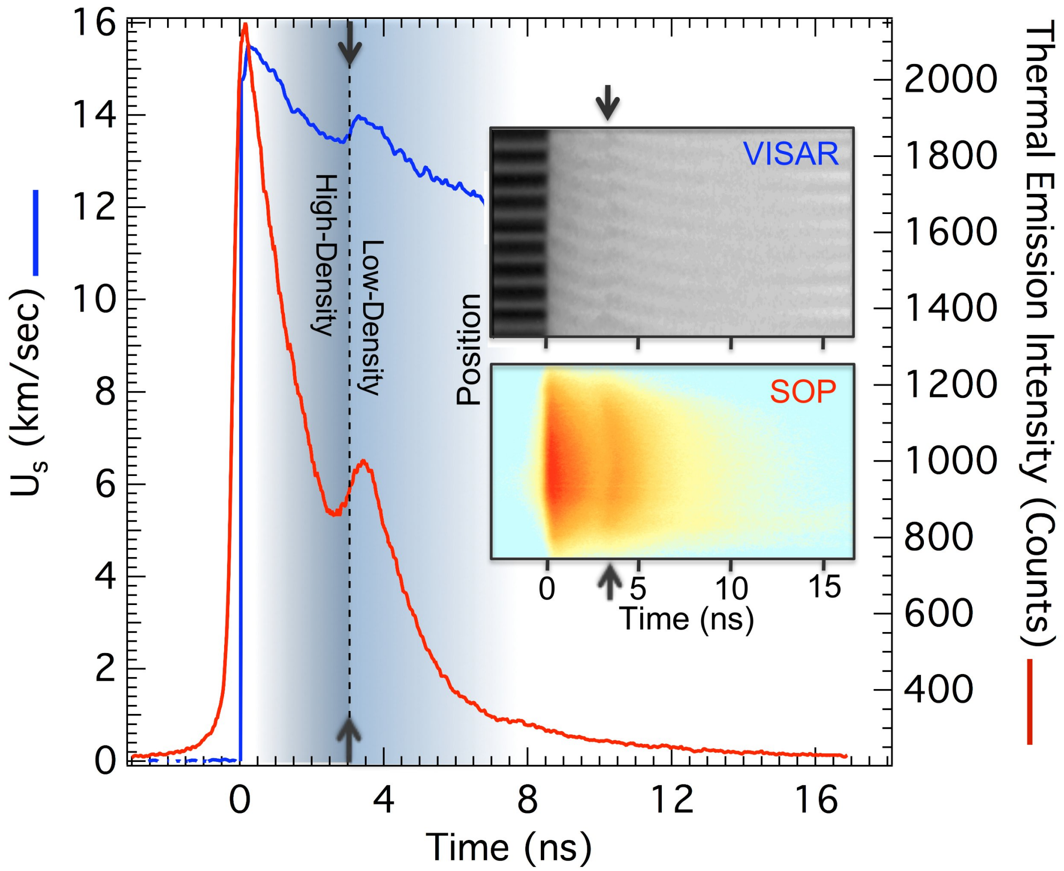

Fig. 5.1. Representative example of the temporal evolution of shock velocity and temperature across the observed transition. Both quantities exhibit a sharp discontinuity (visible between 2 and 4 nsec) as the Hugoniot intersects the liquid-liquid phase boundary, signifying a large change in density and latent heat, shown here for an experiment in a single-crystal sample. Inset: Arrows indicate the transition in the raw data images from which the profiles in the main figure are extracted.

---

[1] Because the phase boundary plotted in Figure 5.2 has been determined by connecting the midpoint of both observations, errors presented here are estimates obtained by artificially modifying dP/dT within the limits of the temperature errors (shaded bands in Figure 5.2).

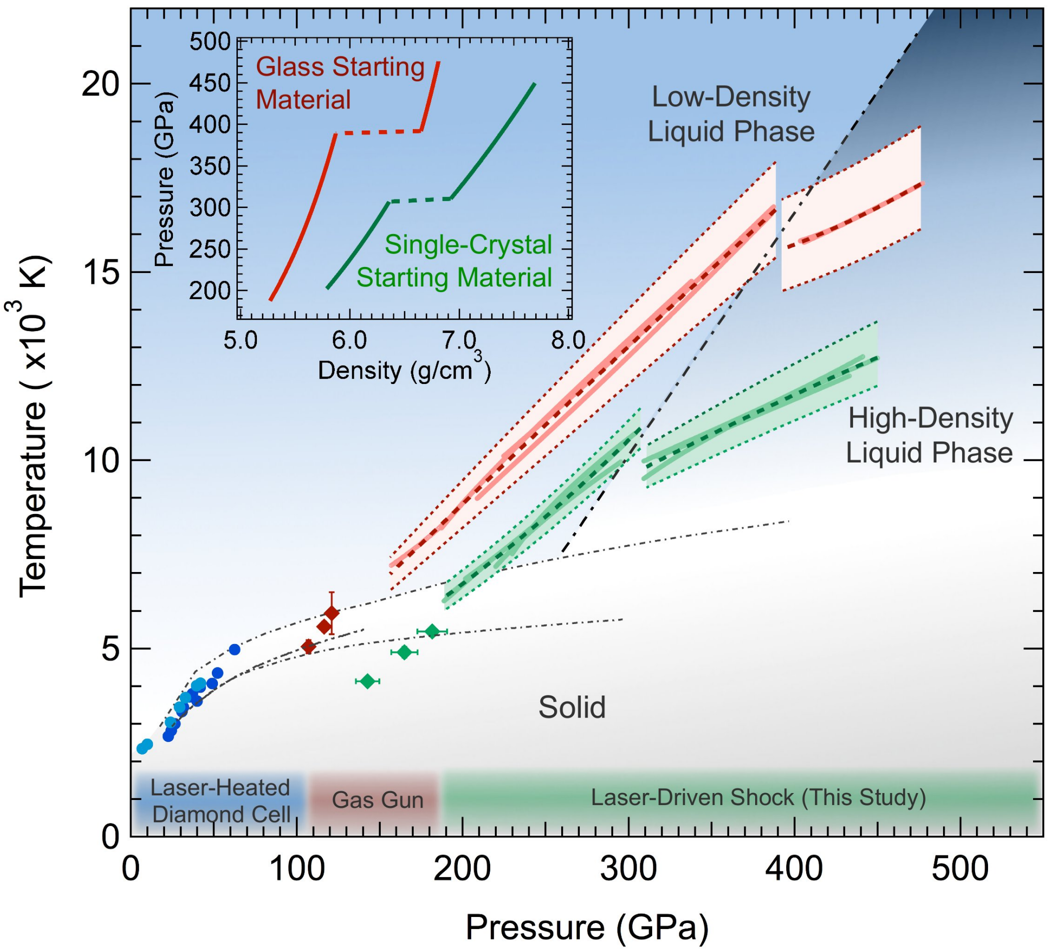

Fig. 5.2. Pressure-Temperature phase diagram for $MgSiO_3$. Liquid-liquid phase transition (dash-dot line) manifests itself as a discontinuity in apparent temperature and density along the shock Hugoniot for single-crystal and glass starting materials (green and red bands, respectively, showing data from 3 shots in each case). Thin, grey lines are predicted melt curves [Stixrude and Karki, 2005; Belonoshko *et al.*, 2005; de Koker, Stixrude, 2009]. Green and red diamonds: gas gun data for single-crystal and glass, respectively [Akins and Luo, 2004; Luo and Akins, 2004)]. Blue circles: laser-heated diamond anvil cell melting data [Shen, Lazor, 1995; Zerr, Boehler, 1993]. Inset: measured pressure-density Hugoniot relationship showing the large increase in density across the phase boundary depicted in the main figure.

HUGONIOT EQUATION OF STATE DATA FOR $MgSiO_3$ LIQUID

Hugoniot equation of state (EOS) data were obtained for $MgSiO_3$ in the high-density liquid phase by impedance matching using an α-SiO_2 standard, as previously described by McQueen [1970] and as discussed in appendix A. For these experiments, a 32 μm-thick window of α-SiO_2 was interposed between the Al pusher and the sample material as shown in Figure A1.

The transition from the low-density liquid Hugoniot to the high-density liquid Hugoniot is defined by introducing two points, *a* and *b,* which do not represent measured EOS points but rather the limits of each phase (Figure 5.3). The Hugoniot of the low-density liquid phase is taken to be defined by the existing gas-gun data from Mosenfelder *et al.* [2009], which thus fixes point *a* based on our observed velocity from decaying shock experiments as the Hugoniot passes into the low-density phase (upper inset, Figure 5.3). Similarly, the shock velocity at point *b* is defined by our VISAR data; however, it remains to define the associated particle velocity, u_P by fitting a linear relationship to our data for the high-density, high-pressure phase.

Here we note that the difference in shock velocity, ΔU_S, between points *a* and *b* may be used as a constraint to better define the slope of the Hugoniot for the high-pressure phase than a simple linear fit to our six data points alone. We do this by treating point *b* as an 'adjustable' data point and allowing our fit to the U_S-u_P data in the high-density phase to vary slightly. With each iteration, we test the resulting P-u_P relationship, until it can be reflected about point *b* such that it intersects the fixed point *a* and simultaneously reproduces the correct ΔU_S (Figure 5.3, middle inset). This method is analogous to the impedance matching construct described in appendix A, and results in a self-consistent Hugoniot for the high-pressure phase which satisfies the constraints imposed by the observed discontinuity in U_S. Although a simple linear fit to our measured EOS points (ignoring the fictive point *b*) results in a very similar result, the ΔU_S at the phase boundary is better reproduced by the iterative fitting technique described here. An identical technique was applied to data collected for the glass starting material.

In this study we have employed the equation of state for α-SiO_2 given by Hicks *et al.* [2006], however it should be noted that a more recent EOS has been published [Knudson *et al.*, 2009] which proposes a modification to Hicks *et al.*. While the choice of quartz EOS has a direct effect on the pressures determined using the impedance matching technique, the potential difference in this study is expected to be small given that the initial densities of the $MgSiO_3$ sample materials (particularly the glass) are close to that of α-SiO_2, resulting in a small impedance mismatch. The difference in α-SiO_2 EOS becomes more significant when used in this manner as the density difference between the sample and standard increases.

TABLE 5.2 – Equation of State Data For $MgSiO_3$ From This Study

Starting Material	Shot[b]	ρ_0 (g/cm^3)[a]	U_S (km/s)	u_p (km/s)	P (GPa)	ρ (g/cm^3)	Temperature (K)
Single Crystal	En16 (J)	3.22	16.76 (0.42)	10.14 (0.5)	547.22 (30)	8.15 (0.29)	14486 (1190, 880)
Single Crystal	En17 (J)	3.22	15.76 (0.42)	9.30 (0.5)	471.95 (28)	7.85 (0.31)	13149 (995, 802)
Single Crystal	En18 (J)	3.22	15.36 (0.39)	8.9 (0.36)	440.19 (25.5)	7.66 (0.16)	12544 (935, 744)
Single Crystal	En21 (J)	3.22	14.98 (0.46)	8.52 (0.54)	410.97 (28.5)	7.47 (0.27)	11966 (850, 700)
Single Crystal	CEOS1 (Ω)	3.22	17.95 (0.28)	11.15 (0.35)	644.46 (23)	8.5 (0.2)	--
Single Crystal	CEOS2 (Ω)	3.22	20.25 (0.26)	13.15 (0.34)	857.45 (24.5)	9.18 (0.2)	--
Glass	Eng3 (J)	2.74	17.07 (0.45)	10.38 (0.56)	485.69 (29)	6.98 (0.3)	17590 (1563, 1209)
Glass	Eng4 (J)	2.74	16.47 (0.34)	9.89 (0.42)	446.1 (21.5)	6.86 (.22)	16632 (1465, 1169)
Glass	GEOS1 (Ω)	2.74	21.35 (0.17)	13.3 (0.22)	778.03 (15.5)	7.26 (0.1)	--
Glass	GEOS2 (Ω)	2.74	23.27 (0.17)	14.76 (0.22)	941.20 (16.8)	7.49 (0.1)	--

a. Initial density taken from Akins et al., [2003], and Gaudio et al., [2008]. Uncertainty in initial density is estimated as ±0.01 g/cc for all samples.; b. J, Ω denotes facility at which experiments were carried out (Janus laser, Jupiter Laser Facility, LLNL and Omega Laser, University of Rochester, respectively).

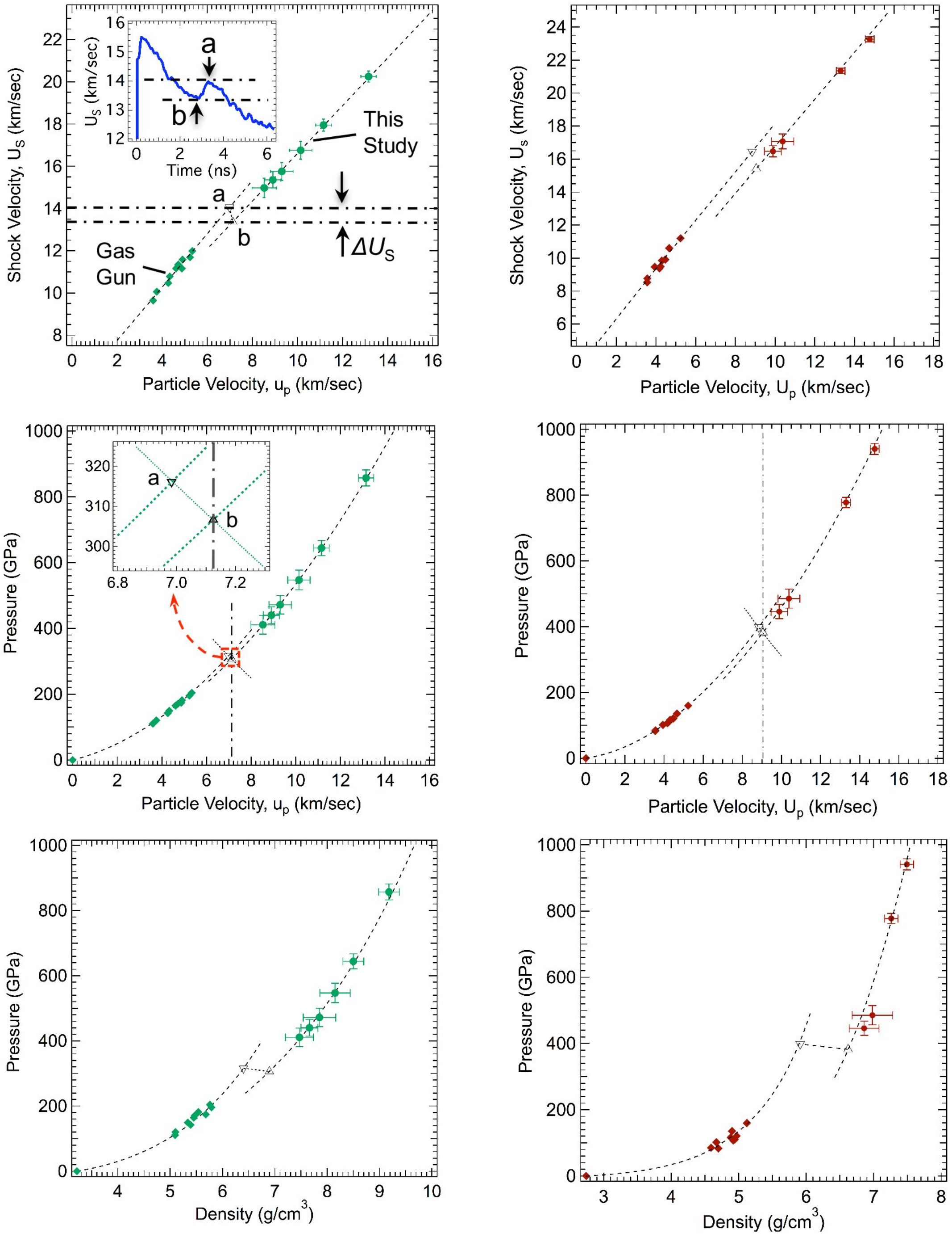

FIGURE 5.3. Hugoniot Equation of State Data for $MgSiO_3$, including points listed in table 5.2. Left column: single-crystal data. Right column: glass data. Data from this study constrain the EOS of the high-pressure liquid phase in both starting materials and are in the right-hand side of each plot, depicted with error bars. Data in the low-pressure phase (without error bars) are from gas-gun studies [Akins *et al.*, 2004 and Luo *et al.* 2004, renalyzed in Mosenfelder *et al.* 2009]. Insets: points ‘a’ and ‘b’, used to constrain the high-pressure EOS, as described in the text.

OPTICAL REFLECTIVITY AND ELECTRONIC PROPERTIES

Optical reflectivity is measured at a wavelength of 532 nm by comparing the reflected intensity of the VISAR probe beam with a reference intensity. The reference signal is obtained by splitting the probe beam before it encounters the sample such that the original shape and intensity of the probe is recorded as a function of time on one side of the VISAR record. The reflected intensity is then divided by the reference and normalized to the known pre-shock reflectivity of the Aluminum buffer (0.85).

The reflectivity in both starting materials is seen to rise with pressure, similar to the behavior reported in the previous chapters for MgO and SiO_2. In the $MgSiO_3$ single-crystal, the break in slope (Figure 5.4) separating the region of low reflectivity from high reflectivity closely matches the pressure of the observed phase transition which suggests that the material transformation is related to a change in electronic behavior. In the glass, however, the reflectivity rises well before the phase transition. Because the glass starting material has a lower initial density, the Hugoniot is at higher temperatures at a given pressure compared to the single-crystal. This introduces the possibility that the higher reflectivities in the glass between 200 and 400 GPa may be largely induced by thermal excitation of electrons.

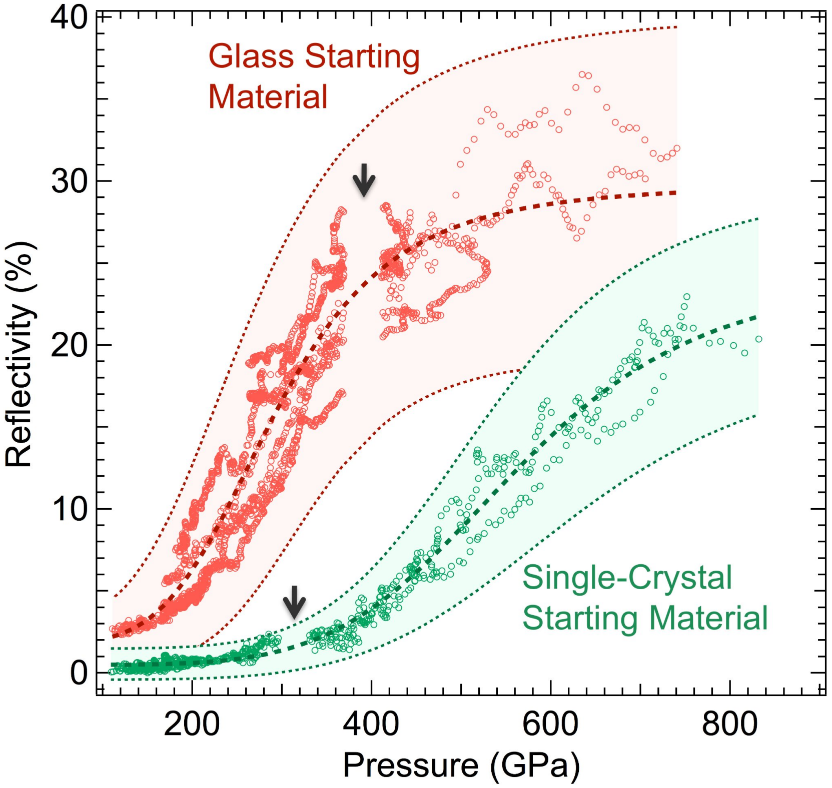

Fig. 5.4. Observed optical reflectivity at 532nm as a function of pressure. Experiments along the single-crystal Hugoniot reveal that optical reflectivity at 532 nm is less than ~2% in the low-pressure phase but rises sharply upon transition to the high-pressure phase (shown by the arrows), indicating metallic-like conductivity. The enhanced reflectivity in low-pressure phase (below 400 GPa) for the glass starting material is likely due to a contribution of thermally excited electrons, owing to the higher temperatures achieved along the glass Hugoniot.

ESTIMATION OF THERMODYNAMIC PROPERTIES ALONG THE HUGONIOT

Thermodynamic properties along the Hugoniot are investigated with the goal of providing a comparison with previous experiment and theory for $MgSiO_3$ liquid and to better elucidate the possible nature of the proposed transition. Estimates are limited in accuracy by the relatively large uncertainties in measured temperature, particularly at the highest pressures, however the results are qualitatively valuable in providing additional information about the possible mechanisms at hand.

As for the case of MgO, the shock temperature measurements in $MgSiO_3$ permit an estimation of specific heat, C_v, based on the slope of the Hugoniot. In this case, a second method of determining C_v is also made possible by comparing the differences in internal energy and temperature (ΔE_H and ΔT_H) between the glass and single-crystal Hugoniots at constant volume where internal energy is defined by the third Rankine-Hugoniot jump condition such that C_v is given simply as

$$C_v = \left.\frac{\Delta E_H}{\Delta T_H}\right|_V = \left.\frac{E_{Glass} - E_{Single-Crystal}}{T_{Glass} - T_{Single-Crystal}}\right|_V \tag{5.1}$$

Because the Hugoniots of the two starting materials only overlap over a small range of density, this technique is applicable to only a portion of our data in the low-pressure phase (5.8-5.9 g/cm^3, as shown in Figure 5.2, inset). Equation 5.1 has an advantage over the technique outlined in Chapter 4 in that it does not require prior knowledge of the Gruneisen parameter. In fact, the resulting values of C_v may be used to calculate the Gruneisen parameter independently using the following relation:

$$\gamma = \frac{V}{C_v}\left(\frac{dP}{dT}\right)_V \tag{5.2}$$

Applying equation 5.1 where the data overlaps in volume in the low-pressure phase gives C_v ~ 5.6 -5.8 Nk_B. This is in reasonable agreement with predicted values of ~4.5-5 [de Koker and Stixrude, 2009]. Plugging these results into equation 5.2 yields a Gruneisen parameter that increases slightly with pressure from $\gamma \sim 1.29$-1.31, also in reasonable agreement with previous experiments [Mosenfelder *et al.*, 2009] and theory [de Koker and Stixrude, 2009; Stixrude *et al.*, 2005]. By comparison, the slope method (equation 4.1) gives an average value of C_v ~ 5.08-5.25 Nk_B for the low-pressure phase assuming a (pressure-independent) value for γ of 1.3.

Since the data in the high-pressure phase do not overlap in volume (see inset, Figure 5.2), only the 'slope method' described in Chapter 4 (equation 4.1) is applicable for determining C_v. Because this technique does not allow an independent determination of γ, the value obtained from equation 5.2 was applied for this calculation ($\gamma = 1.3$).

As shown in Figure 5.5, the results suggest an increase in C_v across the transition of ~3.5 fold, attaining values on the order of ~18 Nk_B. This result may need to be treated with caution for several reasons since it relies on several quantities that are rather poorly constrained. First, γ is expected to increase with pressure [deKoker and Stixrude, 2009; Stixrude *et al.*, 2005; Mosenfelder *et al.*, 2009], however the effect of a phase transition may result in unexpected deviations, to which C_v could be sensitive. In addition, the large uncertainty in measured temperature in the high-pressure phase (Figure 5.2) is imposed on corresponding estimates of specific heat. If the deviation in the SOP data across the transition is caused by a significant change in the spectral dependence of the emissivity rather than a real change in temperature, C_v would likely be over-estimated for the high-pressure phase. This possibility discourages detailed speculation based on the magnitude of the change in specific heat, although qualitative conclusions may be drawn from the apparent increase.

Elevated specific heat indicates that the phase transition is associated with a large uptake of energy that does not go into raising the temperature. This may be caused by several factors. The high optical reflectivity in the high-pressure phase (Figure 5.4) suggests a large number of mobilized carriers which would be expected to give rise to a large electronic contribution to C_v. An increase may also imply passage of the Hugoniot through a mixed-phase region, in which case the energy required to undergo transformation may be taken up over a broad pressure range. If this is so, then the apparently abrupt nature of the transition suggested by the VISAR would only be indicative of the *onset* of transformation. Unfortunately, the data do not support specific discrimination between these possible contributions, but do suggest a change in the nature of the bonding states in the high-pressure liquid.

The thermal expansion coefficient, α, may also be estimated using the shock temperature measurements. α is approximated according to the difference in the two Hugoniots at constant pressure as

$$\alpha = \frac{1}{V}\left(\frac{\partial V}{\partial T}\right)_P \approx \left.\frac{\Delta \ln V}{\Delta T}\right|_P \tag{5.3}$$

Results are shown in Figure 5.5, below. α is seen to decrease across the proposed transition, which can be understood in terms of the large apparent difference in temperature and corresponding collapse to high-density in the high-pressure phase. Again, the accuracy of estimates in the high-pressure phase is influenced by the large uncertainty in temperature.

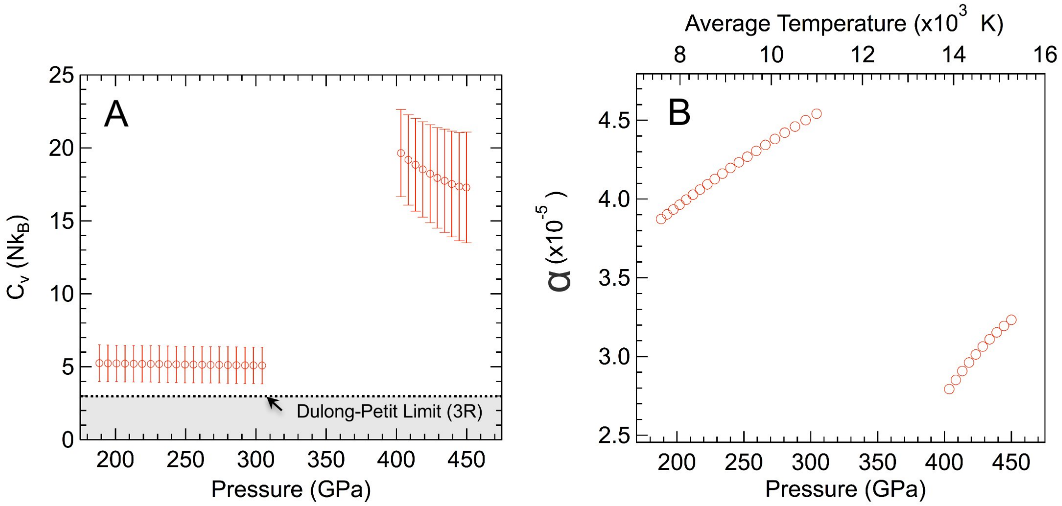

Fig. 5.5. Estimates of specific heat, C_v, and thermal expansion coefficient, α. Panel A: Averaged estimates of specific heat are in reasonable agreement with previous studies in the low-pressure phase for a constant Gruneisen parameter (γ=1.3). C_v appears to increase by ~3.5 fold across the transition. Error bars include only the uncertainties in the measured quantities in equation 4.1 and do not necessarily reflect the validity of our assumption of constant γ, nor the potential for erroneous temperature measurements in the high-pressure phase due to the possibility of a change in emissivity. Panel B: Estimate of the thermal expansion coefficient at constant pressure.

Discussion

Alternative Interpretations

It is clear from the repeatably observed signature illustrated in Figure 5.1 that the material undergoes a significant transition, however the limited number of observable quantities in laser-shock experiments means that the results are not totally unambiguous with regard to the actual mechanism (or mechanism*s*) at hand. Given the paucity of data for super-solidus transitions of the nature proposed here, a number of alternative interpretations were considered but found to be inconsistent with the experimental observations.

Melting Along the Hugoniot

Melting of $MgSiO_3$ at high pressures remains a controversial yet critical problem for the geophysical community and while decaying shock experiments such as these are ideally suited to identify melt along the Hugoniot, several factors lead us to believe that our data is entirely in the molten phase and that the observed transition cannot be attributed to melting. The evolution of the thermal emission shown in Figure 5.1 is evocative of the signature associated with melt in shock studies on other materials resulting from the generation of super-heated solid states as the Hugoniot intersects the solidus [Boness and Brown, 1995; Luo *et al.,* 2003]. Indeed, as shown in Chapter 3, a similar signature occurs in the data for SiO_2 and, in that case, agrees closely with previous estimates of shock melting. Despite this apparent similarity, the observed change in density at the transition in $MgSiO_3$ is much larger than that expected from earlier experiments on the same composition in which melting was inferred [Akins *et al.*, 2004; Luo *et al.*, 2004]. In addition, the known (or expected) melting temperatures of the oxide components, SiO_2 and MgO, fall at lower temperatures than the discontinuities observed in our data, as discussed in the previous chapters. The same is true for all existing theoretical predictions for the melting of $MgSiO_3$ (fig. 5.2 and references therein). Finally, the fact that a reflecting shock is maintained over the entire pressure range of our observations suggests that the material is likely molten throughout based on comparison to other studies (including those in the previous chapters) in which the liquid state is seen to be metallic. The low reflectivity in the single-crystal samples below ~300 GPa may indicate that we are approaching the melting curve, however there is no direct evidence for any further discontinuities at the lowest pressures observed.

Despite the fact that we do not directly observe melting, our data do place constraints on the discrepant predictions for the equilibrium melt curve. That neither VISAR nor SOP show signs of further discontinuities below 300 GPa implies that our lowest temperature observations represent an upper bound on Hugoniot melting. The proposed phase boundary for the liquid-liquid transition also implies a maximum in the equilibrium melt curve in the vicinity of ~250 GPa and ~5000-6000 K based on the relative densities of the liquid phases. In fact, early discussions of liquid-liquid transitions were, in large part, motivated by the need to understand melting curve maxima and the two are often associated [McMillan, 2004, 2007]. Such complicated behavior of the melt curve may also suggest further solid-solid transformations beyond the well-known post-perovskite phase, although the present data do not allow speculation as to the pressures at which these may occur.

A HIGH-PRESSURE, HIGH-TEMPERATURE GLASS TRANSITION? – CONSIDERATION OF A KINETIC MODEL

The possibility that the data represent a high-pressure manifestation of the glass-transition was also considered- e.g. from a low-temperature, low-pressure glassy state to a high-pressure, high-temperature liquid (relaxed) state. At the elevated temperatures of all of our experiments we conclude that our samples achieve a relaxed, liquid state based on comparisons of estimated shock rise-times with available viscosity data for silicate compositions.

Because the temperature at which the glass transition occurs for a given material is rate-dependent, we must compare the time-temperature regime for shock experiments with the expected viscous response (relaxation time) of the material. This time is defined by the Maxwell relationship which linearly relates relaxation time (τ) to shear viscosity (η) such that

$$\tau = \eta / G_\infty \tag{5.4}$$

with the infinite frequency shear modulus $G_\infty = 10^{10}$ Pa. G_∞ is assumed to have negligible temperature and pressure dependence [Bansal and Doremus, 1986; Bucaro and Dardy, 1974; Moynihan, 1995] and is thus treated as a constant. The same is not true for η, which is sensitive to temperature, pressure and composition. Examples of the temperature dependence of τ resulting from the above relationship are shown below (Figure 5.6).

Differences in viscosity as a result of composition diminish with increasing temperature such that, plotted in Arrhenius space ($\log_{10}\tau$ vs. $1/T$) , the tau curves converge for high temperature and short relaxation times [Dingwell and Webb, 1989]. Although there appears to be no experimental data for $MgSiO_3$, the τ-curve should be similar to diopside ($MgCaSi_2O_3$) and likely lies between those for diopside and SiO_2. The expected convergence at high temperature nonetheless suggests relaxation times many orders of magnitude faster than experimental timescales in the temperature range of the observed transition, relative to the zero-pressure curves.

Risetimes for these experiments were estimated to be between ~33 psec and 100 psec. The upper bound is based on the fact that the shock breakout is not resolved in VISAR data, and these have a temporal resolution of ~100 psec. Alternatively, rise-times of less than ~33 psec result in a shock front approaching the limit of optical depth required to sustain a reflecting shock at the wavelength of the VISAR probe beam (532 nm). The region of plausible risetime is shown in pink in Figure 5.6, suggesting relaxed states for the temperatures measured (shown in tan). Although Dingwell and Webb [1989] suggest that unrelaxed behaviour may commence up to 2 $\log_{10}$ units above the τ-curve for a given material, it is clear that even by those standards, our experiments fall well above the expected glass transition conditions relative to the 1 atm values.

The viscosities of depolymerized melts of similar composition such as diopside are expected to increase with increasing pressure [Scarfe *et al.*, 1979] while the reverse is true – at least over a finite pressure range – for highly polymerized melts (e.g., albite composition, $NaAlSi_3O_8$) [Kushiro *et al.*, 1976; Kushiro, 1978; Scarfe *et al.*, 1987]. At modest pressures, the pressure dependence of melt viscosity may exhibit maxima (e.g., diopside and peridotite [Reid *et al.*, 2003; Liebske *et al.*, 2005]) or minima (e.g., albite [Funakoshi *et al.*, 2002]). The effect of pressure is not well-characterized for multi-component silicate melts and has not been experimentally measured for these compositions at very high pressures because of limitations in techniques commonly employed for such measurements (torsion bar, parallel plate, falling sphere) [Scarfe *et al.*, 1979; Avramov, 2007; Reid, 2003]. The possibility of maxima in pressure-viscosity relationships would seem to preclude the perils of blindly extrapolating to pressures achieved in shock compression experiments from existing results. We can, however, estimate the change in viscosity relative to the 1 atm values necessary to compete with the high temperatures and match the timescales of our experiments such that the glass transition might occur under actual experimental conditions.

From Figure 5.6, it is clear that to intersect plausible experimental risetimes at temperatures of ~1 eV, the viscosities of diopside and SiO_2 would have to undergo a pressure-driven increase of ~9 orders of magnitude and ~5 orders of magnitude, respectively. Although first-principles calculations [Wasserman *et al.*, 1993; Wan *et al.*, 2005; Karki *et al.*, 2010] suggest that the effect of pressure on relaxation time may be significant, direct comparison of these studies is difficult because of varying assumptions made therein. Extrapolation of these theoretical results to the conditions of laser-shock experiments thus seems an unsatisfactory and uncertain means of distinguishing relaxed *vs.* unrelaxed behavior under experimental conditions. Hence, to further test the possibility of a kinetically activated transition, we turn to the following qualitative test of a simple Arrhenius-type activation model based on the Clapeyron slope of the proposed phase boundary in pressure-temperature space.

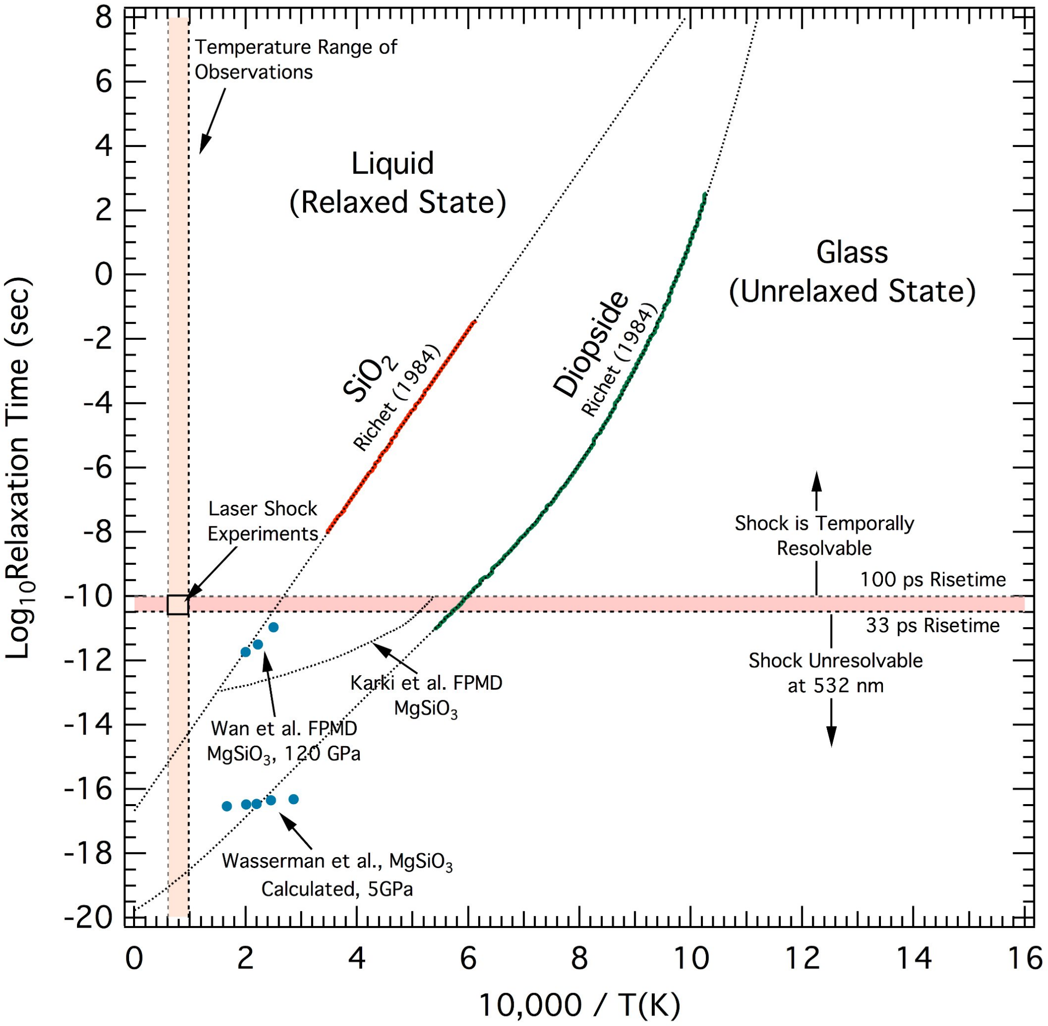

Fig. 5.6. Relaxation times as a function of temperature. Laser-driven shock experiments are seen to lie in the relaxed regime at the high temperatures of our experiments compared to experimental viscosity data for dioside ($CaMgSi_2O_6$), quartz (SiO_2) and first-principles calculations from Wasserman, 1993, Wan, 2005 and Karki, 2010.

TESTING AN ARRHENIUS-TYPE ACTIVATION MODEL

Structural relaxation in a material can be described by assuming that the rate of equilibration of enthalpy is proportional to the deviation from the equilibrium value [Moynihan, 1995] such that

$$\tau \sim \tau_0 \exp\left(\frac{-\Delta H^*}{RT}\right) \tag{5.5}$$

where τ_0 is a constant, ΔH^* an activation enthalpy and R, the ideal gas constant. Assuming the relaxation time, τ, should be the same for shock observations on both the glass and single-crystal starting materials (since the experimental timescales characteristic of the rise-time of the shock are identical in both cases), we can equate the exponential terms where our observations intersect the proposed phase boundary (illustrated schematically in Figure 5.7, below) at (P_1, T_1) and (P_2, T_2). With $\tau_1 = \tau_2$ and

$$\Delta H^* = E^* + PV^* \tag{5.6}$$

$$\tau_1 = \tau_2 \Rightarrow \frac{E^* + P_1V^*}{RT_1} = \frac{E^* + P_2V^*}{RT_2} \tag{5.7}$$

therefore,

$$E^*\left(1 - \frac{T_1}{T_2}\right) = \frac{T_1}{T_2}P_2V^* - P_1V^* \tag{5.8}$$

Since we observe $T_1<T_2$, the left-hand side of (5.8) is positive, requiring

$$\frac{T_1}{T_2}P_2V^* > P_1V^* \Rightarrow \frac{T_1}{T_2} > \frac{P_1}{P_2} \tag{5.9}$$

however this can only be true if the magnitude of the temperature difference is less than the magnitude of the pressure difference between the observations (i.e. a Clapeyron slope < 1 in the *P/T* space of Figure 5.7). Zero Clapeyron slope is permitted for $V^*= 0$ and, similarly, a slope of 1 implies $E^*= 0$. A slope greater than 1 would require E^* and V^* to have opposite signs. A simple activation model thus appears incapable of explaining transitions that are predominantly pressure-driven (with a slope >1), as with the present experimental data, but may be appropriate for temperature-driven relaxation processes. That the experimentally observed Clapeyron slope appears inconsistent with a kinetically activated transition further supports the conclusion that the observed low-pressure phase represents a relaxed state and is not a manifestation of the glass-transition.

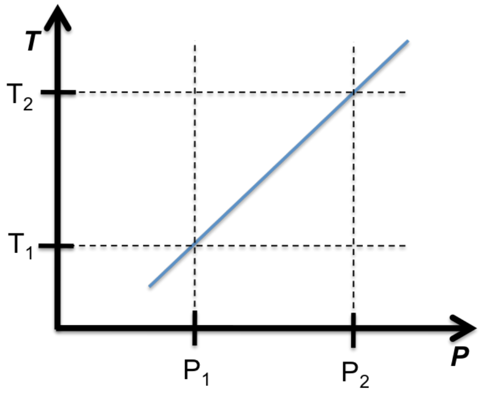

Fig. 5.7. Schematic phase boundary for test of Arrhenius activation model. Shown here is a schematic representation of the phase boundary depicted in Figure 5.2, defining the relationship between T_1 and T_2, P_1 and P_2 for equations 5.7-5.9, above.

POSSIBILITY OF DISSOCIATION

Simulations have predicted dissociation of $MgSiO_3$ into its oxide components with an increase in density at pressures exceeding those of our observations [Umemoto *et al.*, 2006]. Although the estimated rise in specific heat across the transition would be consistent with the energetics of bond-breaking, we reject dissociation as the observed mechanism based on expectations from experiment [Robie *et al.*, 1978] and theory [Umemoto *et al.*, 2006] that the reaction $MgSiO_3 \rightarrow MgO + SiO_2$ results in increased entropy and positive change in enthalpy. Though the literature values for this reaction are similar in magnitude (ΔH= 38.2 kJ/mol, ΔS= 4.9 J/mol·K at $P = 0$, $T = 1000$ K), they are opposite in sign to the latent heat and change in entropy implied by our observed phase boundary. This suggests that a dissociative transition with an increase in density should have a negative Clapeyron slope and is thus inconsistent with the present data. The observed change in density is also ~3 times larger than that calculated by Umemoto *et al.* [2006] for dissociation to the high-pressure polymorphs of MgO and SiO_2.

CONCLUSIONS

The present results represent the first direct observation of a liquid-liquid phase transition in a silicate material, characterized by a metallic, high-pressure phase ~10% more dense than the corresponding low-pressure phase. These results, along with other recent observations [Katayama *et al.*, 2000, 2004], hint that such transitions may represent a fundamental piece of liquid chemistry that has not yet been fully appreciated. The transient presence of metallic-silicate melt in early planetary evolution would have significant implications for models of planetary formation, particularly if density-driven phase separation can occur between distinct liquid states. If this is the case, as the data suggests, liquid-liquid transitions may represent a previously unrecognized means of partitioning chemical species which are soluble in either phase and may serve to enhance convection, influencing core formation, geodynamo effects, and the processes governing mantle-core equilibration.

REFERENCES

Agee, C.B., Crystal-liquid density inversions in terrestrial and lunar magmas, *Phys. Earth Planet. Inter*., **107** (1–3), 63– 74 (1998).

Akins, J.A., *Dynamic compression of minerals in the MgO-FeO-SiO2 system*, Ph.D. thesis, Calif. Inst. of Technology., Pasadena, Calif. (2003).

Akins, J. A., Luo, S.-N., Asimow, P. D., and Ahrens, T. J., *Geophys. Res. Lett.*, **31** (2004).

Avramov, I., *J. of Volcanology and Geothermal Research*, **160**, 165-174 (2007).

Bansal, N.P., Doremus R.H., <u>Handbook of Glass Properties</u>, Academic Press, New York, London, pp 680 (1986).

Barker, L.M., Hollenbach, R.E., *J. Appl. Phys.,* **43**, 4669 (1972).

Barnes, A. *et al*., *Phys. Rev. Lett*., **103**, 225702, (2009).

Belonoshko, A. B., and Dubrovinsky, L. S., *Geochim. Cosmochim. Acta,* **60**, 1645-1656 (1996).

Belonoshko, A.B. *et al.*, *Phys. Rev. Lett.,* **94,** 195701 (2005).

Belonoshko, A.B. *et al.*, *Phys. Rev. B*, **81**, 054110 (2010).

Boness, D.A., Brown, J.M., *Phys. Rev. Lett.*, **71**, (1993).

Bucaro, J.A, Dardy, H.D., *J. Appl. Physics* **45**, pp. 5324–5329 (1974).

Brygoo, S. *et al.*, *Nature Materials* **6**, 274 (2007).

Canup R. M. and Asphaug E., *Nature*, **412**, 708–712 (2001).

Celliers, P.M., *et al.*, *Rev. Sci. Instrum*., **75**, 4916 (2004).

Celliers, P. M., Collins, G.W., Hicks, D. G. and Eggert, J. H., *J. Appl. Phys.,* **98**, 113529 (2005).

de Koker, N. P., Stixrude, L., and Karki, B.B., *Geochim. Cosmochim. Acta,* **72**, 1427-1441 (2008).

de Koker, N., Stixrude, L., *Geophys. J. Int.,* **178,** 162–179 (2009).

Dingwell, D., Webb, S., *Phys. Chem. Minerals*, **16**, 508-516 (1989).

Dingwell, D., Webb, S., *Eur. J. Min.,* **2**, 427-449 (1990).

Eggert, J.H. *et al.*, *Phys. Rev. Lett.,* **100,** 124503 (2008).

Fiquet, G., D. Andrault, A. Dewaele, T. Charpin, M. Kunz, and D. Haüsermann, *Phys. Earth Planet. Inter.*, **105**, 21-31 (1998).

Fiquet, G., A. Dewaele, D. Andrault, M. Kunz, and T. Le Bihan, *Geophys. Res. Lett.*, **27***,* 21-24 (2000).

Funakoshi, K *et al.*, Viscosity measurements of albite melt under high pressure using an in situ X-ray radiography technique, *Proceedings of the AIRAPT-17*, eds. Manghnani, Nellis, Nicol, 1023-1026 (2000).

Funamori, N., Sato, T., *Earth and Planetary Science Letters,* **295**, 435–440 (2010).

Gaudio, S. *et al., Geochimica et Cosmochimica Acta,* **72**, 1222–1230 (2008).

Ghiorso, M.S., and Kress, V.C., An equation of state for silicate melts. II. Calibration of volumetric properties at 105 Pa, *Am. J. Sci***.,** **304**, 679-751 (2004).

Ghiorso, M. S., An equation of state for silicate melts. III. Analysis of stoichiometric liquids at elevated pressure: shock compression data, molecular dynamics simulations and mineral fusion curves, *Am. J. Sci.,* **304**, 752-810 (2004).

Goncharaov, A. *et al.*, *Phys. Rev. Lett.,* **101**, 095502 (2008).

Gong, Z., Fei, Y., Dai, F., Zhang, L., and Jing, F., *Geophys. Res. Lett.,* **31**, (2004).

Greaves, G.N. *et al.*, *Science,* **322**, 566 (2008).

Guignot, N., Andrault, D., Morard, G., Bolfan-Casanova, N., and Mezouar, M., *Earth Planet. Sci. Lett.,* **256**, 162-168 (2007).

Hama, J., and K. Suito, *J. Geophys. Res.*, **103**, 7443-7462 (1998).

Heinz, D.L., Jeanloz, R., *J. Geophys. Res*., **92**, 11 437 (1987).

Hicks, D.G. *et al.*, *Physical Review B,* **78**, 174102 (2008).

Hicks, D.G., T.R. Boehly, J.H. Eggert, J.E. Miller, P.M. Celliers, and G.W. Collins, *Phys. Rev. Lett.,* **97**, 025502 (2006).

Hicks, D.G. *et al., Phys. Plasmas,* **12**, 082702 (2005).

Hirose, K., *Rev. Geophys.,* **44**, RG3001 (2006).

Hui, H., *Viscosity of Silicate Melts*, Ph.D. Thesis, U. of Michigan, Ann Arbor, MI (2008).

Katayama, Y. *et al., Nature* (London) **403**, 170 (2000).

Katayama, Y. *et al., Science*, **306**, 848 (2004).

Knittle, E., Jeanloz, R., *Geophys. Res. Lett*., **16**, 421 (1989).

Knudson, M.D., Desjarlais, M.P., *Phys. Rev. Lett.,* **103**, 225501 (2009).

Kudoh, Y., Ito, E., and Takeda, H., *Phys. Chem. Miner.,* **14**, 350-354 (1987).

Kushiro, I., *Earth and Planetary Science Letters*, **41**, 87-90 (1978).

Kushiro, I., Yoder Jr., H.S., Mysen, B.O., *J. Geophys. Res.,* **81**, 6351–6356 (1976).

Kress, V.C., Williams, Q., Carmichael, I.S.E., *Geochimica et Cosmochimica Acta*, **53**, pp. 1687-1692 (1989).

Labrosse, S., Hernlund, J.W., Coltice, N., *Nature*, **450**, 866-869 (2007).

Lay, T., Garnero, E.J., and Williams, Q., *Phys. Earth Planet. Inter.,* **146**, 441-467 (2004).

Liebske, C., *Earth and Planetary Science Letters*, **240**, 589-604 (2005).

Li, B., and Zhang, J., *Phys. Earth Planet. Inter.,* **151**, 143-154 (2005).

Luo, S.-N., Ahrens, T. J., *Physics of the Earth and Planetary Interior,s* 143–144, 369–386 (2004).

Luo, S.-N., Akins, J. A. , Ahrens, T. J., and Asimow, P. D., *J. Geophys. Res.*, **109** (2004).

Lyzenga, G. A., Ahrens, T.J., Mitchell, A.C., *J. Geophys. Res.,* **88**, 2431 (1983).

Marsh, S. P., *LASL Shock Hugoniot Data,* 658 pp., University of California Press, Berkeley, (1980).

McMillan, P.F., *J . Mater. Chem.*, **14**, 1506-1512 (2004).

McMillan, P. F. *et al.*, *J. Phys. Condens. Matter,* **19**, 415101 (2007).

Miller, J. E. *et al.*, *Rev. Sci. Instrum.,* **78**, 034903 (2006).

Monaco, G., Falconi, S., Chichton, W. A., and M. Mezouar, *Phys. Rev. Lett.,* **90**, 255701 (2003).

Mosenfelder, J.L., Asimow, P.D., Frost, D.J., Rubie, D.C. and Ahrens, T.J., *J. geophys. Res.,* **114**, B01203, (2009).

Moynihan, C.T., Structural Relaxation and the Glass Transition, *Rev. in Mineralogy*, **32**, MSA, ed. Stebbins, McMillan, Dingwell (1995).

Mukherjee, G., Boehler, R., *Phys. Rev. Lett.,* **99**, 225701 (2007)

Murakami, M., K. Hirose, K. Kawamura, N. Sata, and Y. Ohishi, *Science*, **304**, 855-858 (2004).

Navrotsky, A., Thermodynamic Properties of Minerals, from Mineral Physics and Crystallography: A Handbook of Physical Constants, American Geophysical Union (1995).

Oganov, A. R., Brodholt, J.P., and Price, G.D., *Earth Planet. Sci. Lett.,* **184**, 555-560 (2001).

Oganov, A. R., and S. Ono, *Nature*, **430**, 445-448 (2004).

Ohtaka, O. *et al.*, *Phys. Rev Lett.*, **92**, 155506-1 (2004).

Reid, J. *et al., Physics of the Earth and Planetary Interiors,* **139**, 45–54 (2003).

Richet, P., *Geochim. Cosmochim. Acta*, **48**, 471-483, (1984).

Rigden *et al.*, *J. Geophys. Res.*, **93**, No. B1, 367-382 (1988).

Robie, R.A., Hemingway, B.S., Fisher, J.R., *U.S. Geological Survey Bulletin*, 1452, 456 pp., (1978).

Ross, N. L., and R. M. Hazen, *Phys. Chem. Miner.,* **17**, 228-237 (1990).

Saika-Voivod, I., Sciortino, F., and Poole, P.H., *Physical Review E*, **63**, 011202 (2001).

Saika-Voivod, I., Sciortino, F., Grande, T and Poole, P.H., *Physical Review E,* **70**, 061507 (2004).

Saxena, S. K., L.S. Dubrovinksy, F. Tutti, and T. Le Bihan, *Am. Mineral.,* **84**, 226-232 (1999).

Scarfe *et al.*, Changes in Viscosity and Density of Melts of Sodium Disilicate, Sodium Metasilicate and diopside composition with Pressure, *Carnegie Inst. Wash. Yearb.*, **78**, 547-551 (1979).

Scarfe *et al.*, Pressure Dependence of the Viscosity of Silicate Melts, in *Magmatic Processes: Physicochemical Principles*, Mysen BO (ed), 59-67 (1987).

Shim, S.-H., and T. S. Duffy, *Am. Mineral.,* **85**, 354-363 (2000).

Simakov, G. V., and R. F. Trunin, On the existence of overdense perovskite structures in magnesium silicates under conditions of high pressure, *Izvestiya Earth Physics (English Translation),* **9**, 603-604 (1973).

Shen, G., Lazor, P., *J. Geophys. Res.,* **100**, 17 699 (1995).

Spaulding, D.K., Hicks, D.G., Smith, R.F., Eggert, J.H., McWilliams, R.S., Collins, G.W., Jeanloz, R., *Proceedings: Shock Compression of Condensed Matter*, eds. M. Elert, M.D. Furnish, R. Chau, N. Holmes, and J. Nguyen, American Institute of Physics, 1071 (2007).

Stixrude, L., Lithgow-Bertelloni, C., *Geophys. J. Int.*,**162** , 610 (2005).

Stixrude, L., Karki, B., *Science*, **310**, 297-299, (2005).

Stixrude, L., de Koker, N., Sun, N., Mookherjee, M., Karki, B.B., *Earth and Planetary Science Letters,* **278**, 226–232 (2009).

Sweeney, J.S., Heinz, D.L., *Geophys. Res. Lett.*, **20**, 855 (1993).

Tsuchiya, J., T. Tsuchiya, and R.M. Wentzcovich, *J. Geophys. Res.,* **110**, (2005).

Umemoto, K., Wentzcovitch, R.M., Allen, P.B., *Science,* **311**, 983 (2006).

Vanpeteghem, C. B., J. Zhao, R.J. Angel, N.L. Ross, and N. Bolfan-Casanova, *Geophys. Res. Lett.*, **33**, (2006).

Wan, J. T. K., T.S. Duffy, S. Scandolo, and R. Car, *J. Geophys. Res.,* **112**, (2007).

Wang, Y., D.J. Weidner, R.C. Liebermann, and Y. Zhao, *Phys. Earth Planet. Inter.,* **83**, 13-40 (1994).

Wasserman *et al.*, *Earth and Planetary Science Letters*, **114**, 373-384 (1993).

Wilding *et al., Chemical Geology,* **213**, 281– 291 (2004).

Wilding M. C., Benmore C. J., Tangeman J. A. and Sampath S., *Europhys. Lett.,* **67**, 212–218 (2004b).

Williams, Q., and E. J. Garnero, *Science,* **273**, 1528-1530 (1996).

Wolf G.H., McMillan, P.F., *Reviews in Mineralogy and Geochemistry*, **32**;1, p. 505-561 (1995).

Zel'dovich, Y.B., Raizer, Y.P., *Physics of Shock Waves and High-Temperature Hydrodynamic Phenomena*, Dover Publications, New York (1966).

Zerr, A., Boehler, R., *Science* **262**, 553 (1993).

Zoysa, E. G., Colourless enstatite from Embilipitiya, Sri Lanka, *Journal of Gemmology,* **14**, 419-425 (1985).

Structure, Dynamics and Properties of Silicate Melts, eds. J. F. Stebbins, P. McMillan, and D. Dingwell, *Reviews in Mineralogy*, **32**, Mineralogical Society of America, Washington, D.C. (1995).

Conclusions

The properties of silicate melt are expected to have played a critical role in the physical and thermal evolution of the Earth, particularly in the Hadean magma ocean that may have been generated by late-stage giant impact events and during the subsequent equilibration of mantle and core [e.g. Walter and Trønnes, 2004; Benz and Cameron, 1990; Melosh, 1990]. The physical properties of these liquids may continue to play a role today as remnant pockets of partial melt at the core-mantle boundary (CMB) [Lay *et al.*, 2004; Williams *et al.*, 1996; Labrosse *et al.*, 2007]. The results that have been presented here help to constrain the ultra-high pressure behavior of three of the most important minerals in the Earth's interior, and shed new light on their possible role in the evolution of several-Earth mass extra-solar planets. These results demonstrate that complex chemistry persists in silicate and oxide liquids at the conditions of deep planetary interiors and that changes in the liquid state may occur abruptly, contrary to common assumptions. The conclusions that follow consider the results presented in Chapters 3-5 as a collection and discuss implications for the past and present thermal state of the Earth's mantle as well as the relevance to the structure and dynamics of super-Earth planets.

Although the results presented here have primarily examined pressures in excess of those encountered in the Earth, they help to address some of the many outstanding questions about the early evolution and present-day nature of the Earth's mantle. Knowledge of end-member melting temperatures is particularly critical, even when considering the solid state, since viscosity models applied for planetary modeling to describe chemical differentiation often scale with homologous temperature (T/T_M) where T_M is the actual melting temperature [Weertman and Weertman, 1975]. The data that have been presented constrain controversial predictions for the melting behavior of MgO and $MgSiO_3$, showing that the pure compositions melt at ~8000 K and ~6000 K, respectively at the core-mantle boundary pressure (135 GPa). The data also suggest positive dT/dP melt slopes at the CMB pressure for SiO_2 and MgO, indicating that the liquid phases of both materials remain less dense than the isochemical solid throughout the Earth's mantle. The same is likely true for $MgSiO_3$, although a previous study has suggested a density inversion very near CMB pressures [Akins *et al.*, 2004] which the present data cannot definitively support nor dismiss.

The relative densities of the liquid and solid determine dynamic stability. Since present day seismic anisotropy at the CMB has been interpreted as pockets of remnant melt [Lay *et al.*, 2004], the data support the conclusion that chemical partitioning must be invoked to explain the dynamic stability of these pockets over geologic time. At low pressures, iron is preferentially partitioned into the melt relative to the crystals and if this persists at high pressures, the resulting magma would likely be more dense than the coexisting solids. Using reasonable estimates for the partitioning coefficient of Fe in perovskite, molecular dynamics calculations have suggested that this should be a sufficient mechanism for explaining negatively buoyant partial melt [Stixrude *et al.*, 2009]. Although these conclusions are not entirely unexpected, previous experimental data have provided few definite constraints on high-pressure melting.

Because the data appear to support higher melting temperatures than most previous predictions for MgO and $MgSiO_3$, the presence of other chemical constituents must also be invoked in order to lower the eutectic by > 1500 K if perovskite is to melt at the CMB temperature (~4000 K). Shock temperature measurements support $MgSiO_3$ as the more likely candidate for partial melt in the lower mantle and show that the melting temperature of pure MgO is nearly twice the estimated temperature of the CMB at the same pressure. Together, these conclusions indicate that the D" layer in the Earth may truly represent a sort of 'Goldilocks zone', teetering on the very edge of phase stability for sustaining partial melt. Given the observed melting temperatures suggested by our data, an extra-solar planet may not need to be more than a few Earth masses to have a mantle adiabat that permits a larger liquid stability field [Valencia *et al.*, 2006]. Any significant stable layer of melt within such a planet would result in a convective style potentially very different from what is expected in the present day Earth, and would also radically effect coupling between the core and mantle.

Such coupling is largely governed by the transport properties of the lower-mantle constituents. The data presented here have major implications for the electrical and thermal conductivity of molten magnesium-silicates and oxides. As was shown, all three materials demonstrate a large rise in optical reflectivity in the liquid state that can be interpreted as a likely combination of band-gap closure and thermal excitation of charge carriers. The result is that SiO_2, MgO and $MgSiO_3$ all show evidence of a change in electronic behavior commensurate with an insulator-metal transition at or near the melt transition. With the presence of mobile electrons, the thermal conductivity is typically enhanced by up to an order of magnitude at high temperatures and pressures.

The presence of metallic-like melt in an early magma ocean may call for revisiting ideas about core-mantle interaction in planetary models. An interesting early idea was put forth that the Earth's core is actually composed of the same materials as the mantle but which have undergone densification and pressure-induced metallization [Ramsey, 1949]. Geodetic, seismic and compositional constraints, of course, suggest this cannot be the case in the Earth, but it is nonetheless interesting to rephrase Ramsey's postulation by asking what role a metallic silicate layer may play in mediating core-mantle exchange and what affect this may have on an early geodynamo. In any event, the results in the preceding chapters suggest that the liquid transport properties are radically different than what might be expected from solid-state experiments.

Equally unexpected behavior has been has been shown in Chapter 5, in which an entirely new kind of phase transition is presented for $MgSiO_3$, previously unreported for any silicate material. The possibility of (potentially first-order) isochemical liquid-liquid phase separation has not previously been considered in planetary models but would have significant implications given the large density difference between the liquid phases (~10%). Preferential solubility of other chemical species in one or the other of the liquid phases may represent a previously unrecognized means of efficient chemical partitioning during mantle equilibration. At such elevated temperatures, low viscosity would be expected to contribute to high Rayleigh number which, coupled with the large volume change of the transition, would favor vigorous convection in a liquid mantle. The thermodynamic nature of the transition encourages convection since hot (presumably buoyant) material can convert to the low-density phase at greater depth than a correspondingly 'cooler' packet of material which would have to rise further before crossing the phase boundary (see Figure 5.2). Further experiments are needed to determine the precise structural nature of the transition however its very observation makes it clear that the physical chemistry of mantle constituents holds surprises at conditions that are not unrealistic for extra-solar planetary interiors. This observation, along with the small handful of other reported liquid-liquid transitions cited in Chapter 5 also hints that such transitions may, in fact, be common in liquids but have largely escaped identification until now due to the experimental difficulties in studying liquid structure over as broad a range of pressure and temperature as are accessible by laser-driven shock compression.

The possibility of liquid-liquid transitions, metallic-like conductivity of molten silicates and oxides and complex liquid structure are all traits that would be unexpected based on lower-pressure studies. Although it is reasonable to ask whether the results presented here have predictive value when considering more complex compositions, such unexpected behavior reinforces the fact that there is a good deal of previously unrecognized complexity in the physical and chemical behavior of even relatively 'simple' compositions. Further experiments similar to those presented here would be desirable with samples introducing a known fraction of iron in order to quantify the effects of this component on the material properties described above.

The technique of applying laser-driven shocks to study material properties at extreme conditions is very new and, as yet, relatively unrecognized by the high-pressure geophysical community. The studies presented here demonstrate the utility of this method for exploring the conditions of planetary interiors at pressures and temperatures far beyond what is achievable with other experimental methods. Streaked optical pyrometry has been shown to be a powerful tool for recognizing the occurrence of phase transformations in materials and for extracting thermodynamic data, all of which is critical to informing models and interpretations of planetary evolution. Because such experiments currently represent the only such method for exploring the conditions of extra-solar planetary interiors in the laboratory, it is hoped that these studies and the many that will surely follow contribute to a more holistic understanding of planetary origins and evolution.

References

Akins, J. A., Luo, S.-N., Asimow, P. D., and Ahrens, T. J., *Geophys. Res. Lett.*, **31** (2004).

Benz, W., Cameron, A. G. W., *Terrestrial Effects of the Giant Impact*. In Origin of the Earth (H. E. Newsom and J. H. Jones, eds.), pp. 61-67. Oxford Univ., New York (1990).

Canup, R.M., *Icarus*, **168**, 2, 433–456 (2004).

Garnero, E. J., Helmberger, D. V., *Phys. Earth Planet. Inter.*, **91**, 161– 176 (1995).

Höink, T., Schmalzl, J., Hansen, U., *Geochem. Geophys. Geosyst.*, **7**, 9 (2006).

Jeanloz, R., Roufosse, M., *J. Geophys. Res.*, **87**, 10, 763– 10, 772 (1982).

Labrosse, S., Hernlund, J.W., Coltice, N., *Nature*, **450**, 866-869 (2007).

Lay, T., Garnero, E.J., Williams, Q., *Physics of the Earth and Planetary Interiors*, **146**, 441-467 (2004).

Melosh, J., *Giant Impacts and the Thermal State of the Early Earth*, In <u>Origin of the Earth</u> (H. E. Newsom and J. H. Jones, eds.), pp. 69-83. Oxford Univ., New York (1990).

Mosenfelder, J.L., Asimow, P.D., Ahrens, T.J., *J. Geophys. Res.-Solid Earth,* **112**, B6 (2007).

Ramsey, W.H., *On the Nature of the Earth's Core*, *Geophys, J. Int.*, **5**, 9, 409-426 (1949).

Ringwood A. E., *Earliest History of the Earth-Moon System*. In <u>Origin of the Earth</u> (H. E. Newsom and J. H. Jones, eds.), pp. 101–134. Oxford Univ., New York (1990).

Stixrude, L., Karki, B., *Science*, **310**, 297-299, (2005).

Stixrude, L. *et al.*, *Earth and Planetary Science Letters,* **278**, 226-232 (2009).

Valencia, D. *et al., Icarus*, **181**, 545–554 (2006).

Walter, M.J., Trønnes, R.G., *Earth and Planetary Science Letters,* **225**, 253–269 (2004).

Weertman, J., Weertman, J.R., *Annu. Rev. Earth Planet. Sci.*, **3**, 293-315 (1975).

Williams, Q., Garnero, E.J., *Science*, **273**, 5281, 1528-1530 (1996).

Zerr, A., Boehler, R., Nature (London), **371**, 506 (1994).

SECTION III – APPENDICES

Appendix A
Experimental Techniques and Methods

LASER-DRIVEN SHOCK WAVES: GENERATING HIGH-PRESSURE STATES

Laser-driven shock waves are generated by ablation of an absorbing material from the target assembly by a high-intensity (~10^{13} W/cm^2) laser pulse with a duration of ~1-6 nanoseconds. The ablated material forms a plasma that expands upstream, back toward the drive laser. Conservation of momentum results in the creation of a pressure disturbance that propagates downstream toward the sample and rapidly steepens into a shock front before reaching the sample material. The laser-absorbing layer is typically a vapor-deposited polyimide-type plastic (CH), 10-15 μm thick. Beneath this plastic layer, a thin coating of gold helps attenuate x-rays from the laser-generated plasma. Laser phase plates define the focused spot size of the drive beams, and thus the shocked area of the sample, while ensuring uniform intensity distribution and a planar shock profile (i.e. spatially smooth in the transverse direction). In a typical experiment, the shocked area is ~1 mm^2 which determines the characteristic sample dimensions (~1 mm^2 in area and ~100-300 μm in thickness)[1]. If the sample is transparent, optical diagnostics (described below) may be used to observe the temporal evolution of the shock in the sample.

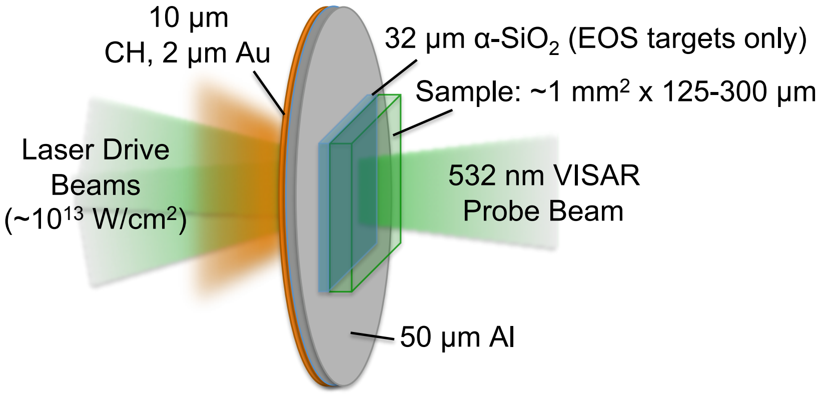

FIGURE A1. Illustrating a typical target assembly for a laser-driven shock experiment. Experiments intended to measure the equation of state of the sample (as described below) include a thin α-SiO$_2$ window interposed between the Al buffer and the sample.

For a given initial density, the locus of end-states achieved by driving the sample to increasingly higher pressure defines a pressure-volume relation which we call the Hugoniot. The relationship of the physical variables defining the Hugoniot may be simply related by conservation laws, as derived in the following section.

---

[1] Rarefactions propagate inward from the edges of the sample inward with a velocity comparable to the shock velocity. Therefore, these dimensions ensure that an undisturbed shock front may be observed over a zone ~1 mm – 2*(thickness) ≈ 400-800 μm in diameter at the back surface of the sample.

DERIVATION OF RANKINE-HUGONIOT EQUATIONS

At the shock front, conservation of mass, linear momentum and energy must be obeyed, such that we can relate the physical quantities on either side of the shock by simple relations dictated by the associated conservation laws.

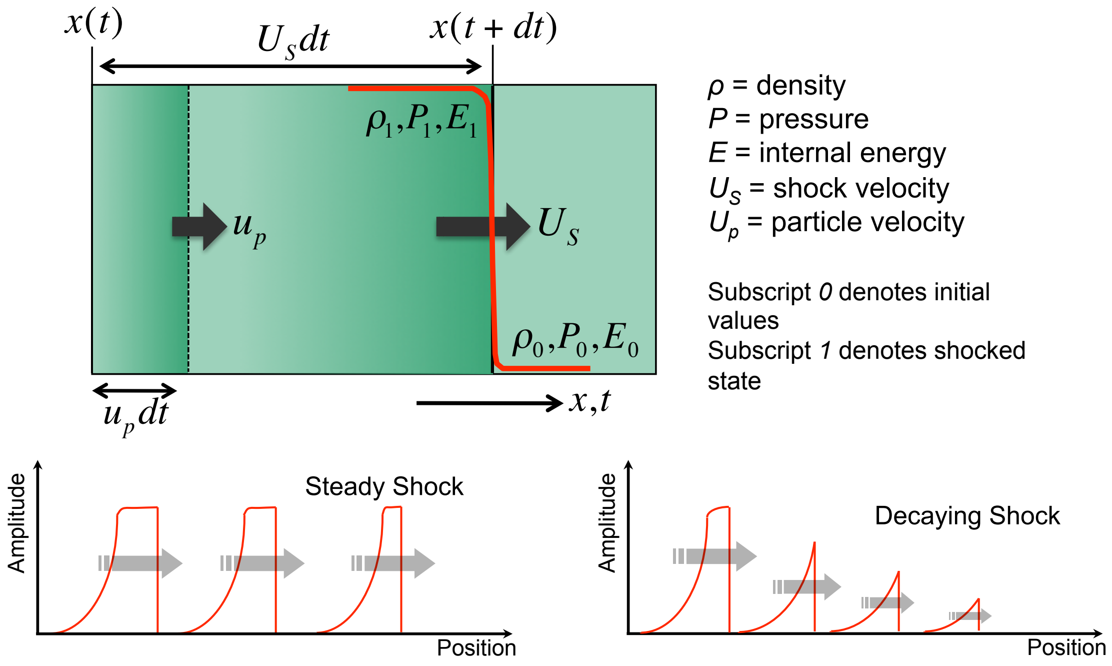

FIGURE A2. Schematic of shock propagation through a medium. Top: illustration accompanying derivation of the Hugoniot jump conditions, defining conservation of mass, momentum and energy across the shock front. Bottom panels: A steady shock maintains constant pressure as a function of time or distance in the material. A decaying shock is overtaken by a rarefaction wave, resulting in decreasing amplitude as a function of time and distance.

Because mass cannot be created or destroyed, the mass in any initial volume must be equal to the mass in the compressed volume behind the shock front. We derive conservation laws by expressing all quantities per unit area and per unit mass and using the schematic shown in the top panel of Figure A2. If the shock travels from position *x(t)* to *x(t+dt)* in time *dt*, the initial mass in this volume is given by $\rho_0 U_S dt$ (initial density times a volume defined by the distance the shock travels in time *dt*). In the same time interval, the original location of the shock moves forward by a distance $u_p dt$. Thus the final mass in the compressed volume is $\rho_1(U_S-u_p)\,dt$. Equating these terms, we obtain

$$\rho_0 U_S = \rho_1 (U_S - u_p) \tag{A1}$$

Conservation of momentum can be expressed by considering that pressure, P_1, is defined as force per unit area. Applying Newton's second law, *F=ma*, we can write

$$F = ma \Rightarrow \rho_0 U_S dt \left(\frac{u_p}{dt} \right) \tag{A2}$$

where the mass in our unit volume is $\rho_0 U_S\, dt$ and acceleration is u_p/dt. Pressure along the Hugoniot is then

$$P_1 - P_0 = \rho_0 U_S dt\left(\frac{u_p}{dt}\right) \Rightarrow P_1 - P_0 = \rho_0 U_S u_p \tag{A3}$$

During compression, work is done on the system that raises its energy. Part of this work goes into changing the internal energy while part of it increases the kinetic energy, the latter being due to the mass of the sample having been accelerated to a particle velocity, u_p. Conservation of energy allows us to equate the work done with the change in energy as

$$-P\Delta V = \Delta E_{Internal} + \Delta E_{Kinetic} \Rightarrow -\left(P_1 - P_0\right)\left(V_1 - V_0\right) = \left(E_1 - E_0\right) + \frac{1}{2}u_p^2 \tag{A4}$$

where the kinetic term ($1/2mv^2$) is per unit mass, hence 1/2 u_p^2. This term can be re-written in terms of density (hence specific volume, $V=1/\rho$) by substituting from eqn. A1 such that the internal energy of the system along the Hugoniot is given as

$$E_1 - E_0 = \frac{1}{2}\left(P_1 + P_0\right)\left(V_0 - V_1\right) = \frac{1}{2}P\Delta V \tag{A5}$$

This equation then tells us that half of the work done on the sample goes into accelerating it to its particle velocity, and for P_0 and $E_0 = 0$, the internal energy is given simply as $E_1 = 1/2\ u_p^2$. We are thus left with the canonical 'Rankine-Hugoniot' jump-conditions:

1. Conservation of Mass	$\rho_0 U_S = \rho_1(U_S - u_p)$
2. Conservation of Momentum	$P_1 - P_0 = \rho_0 U_S u_p$
3. Conservation of Energy	$E_1 - E_0 = \frac{1}{2}\left(P_1 + P_0\right)\left(V_0 - V_1\right)$

These equations contain five variables such that experimental determination of any two of them (typically U_S and u_p) is sufficient to define the Hugoniot Equation of State (EOS) of the sample if the initial conditions (ρ_0, P_0, E_0) are known. Conveniently, in the absence of phase transitions, the relationship between U_S and u_p is found to be linear for most materials with 'normal' compressibility (i.e. bulk modulus which increases with compression). As discussed in Chapter 2, the Hugoniot equations do not specify the temperature of the sample that must therefore be measured separately.

In these studies, short laser pulses (1-2 ns) were typically employed such that the resulting shock is unsupported after a short time. The shock is followed by a rarefaction (or release) wave that can overtake the shock front by virtue of the fact that it travels through compressed material (i.e. moving with finite velocity, u_p). As this occurs, the shock front decays in amplitude as shown in the lower right panel of Figure A2. Decaying shock fronts allow observation of a continuum of Hugoniot states in a single experiment because of the continuously decreasing amplitude of the shock and are thus ideally suited for experiments seeking to traverse phase transitions. Because each high-pressure state is achieved upon compression, the Rankine-Hugoniot conditions may be applied to temporally resolved data to determine the evolution of the sample as function of time (hence pressure).

LASER FACILITIES

Experiments were carried out on the Janus platform at the Jupiter Laser Facility at Lawrence Livermore National Labs (LLNL) and at the OMEGA facility at the Laboratory for Laser Energetics (LLE) at the University of Rochester, in New York. The Janus laser is a two-beam Nd:glass laser capable of delivering ~1 kJ/beam at 1053 nm. Our experiments employed the frequency-doubled wavelength (527 nm), in which case each beam can deliver up to ~350 J/beam for a 2 ns pulse. The OMEGA facility is also a Nd: glass system, but is significantly larger in scale, comprising 60 beams capable of delivering ~30 kJ of energy at 351 nm. Both beams were employed at the Janus facility, while up to 6 beams were used at OMEGA based on the energy required to achieve the desired pressure and because of the planar sample geometry.

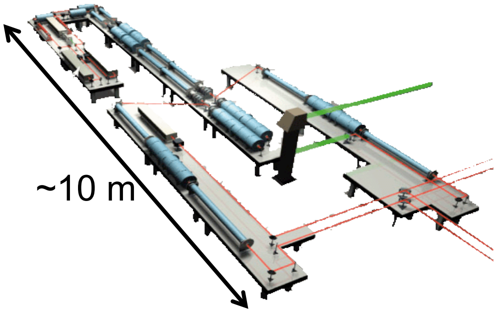

FIGURE A3. The Janus laser is a two-beam Nd:glass laser operated at the Jupiter Laser Facility at LLNL. The beams propagate to a vacuum chamber containing the sample in an adjoining room. Image courtesy jlf.llnl.gov.

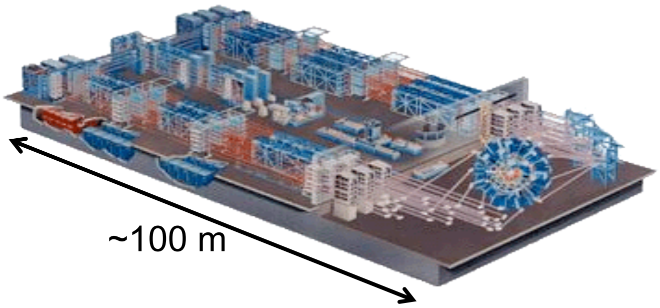

FIGURE A4. The OMEGA facility is a sixty-beam Nd:glass laser operated at the Laboratory for Laser Energetics at the University of Rochester, NY. The individual beams are arranged in a linear manner (in the left portion of the image). The sample is contained in a spherical vacuum chamber (depicted on the right). Image courtesy lle.rochester.edu.

CHARACTERIZING THE HIGH-PRESSURE STATE: OPTICAL DIAGNOSTICS

The evolution of the shock front, hence the high-pressure state in the sample, is measured using spatially and temporally-resolved optical diagnostics (~10 μm/pixel and 100 ps, respectively). The primary observable quantities in a shock-compression experiment are typically shock velocity (U_S) or particle-velocity (u_p) and thermal emission; however, advanced diagnostics have been and are currently being developed for particular spectroscopic, imaging and particle-physics applications. In the studies presented here, shock velocity and optical reflectivity were measured using a Velocity Interferometry System for Any Reflector (VISAR) while thermal emission was recorded by Streaked Optical Pyrometry (SOP) at both the Janus and OMEGA facilities. A schematic illustrating these diagnostics is shown in Figure A5.

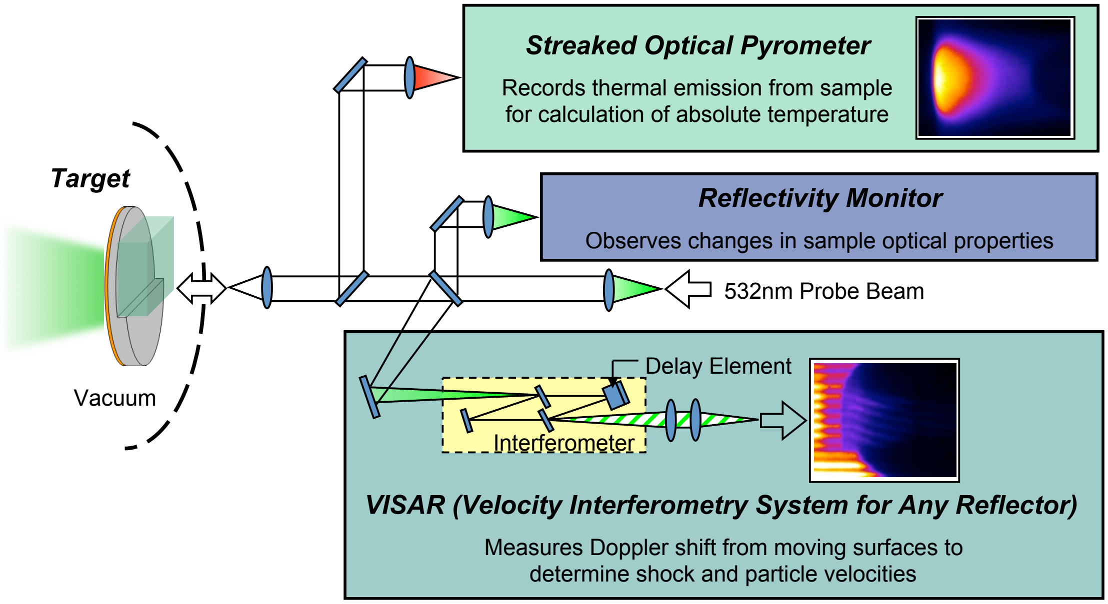

FIGURE A5. Schematic showing the diagnostics used to characterize the shocked sample. The VISAR measures shock velocity by measuring the Doppler shift from the moving shock front. Optical reflectivity is measured by comparing the reflected intensity of a probe beam with a reference intensity. Streaked Optical Pyrometry observes thermal emission from the sample, from which absolute temperatures are determined.

VISAR

The VISAR diagnostic has been described comprehensively by Barker and Hollenbach, 1972 and Celliers *et al.*, 2004. A 532 nm probe laser is reflected from the target and directed through a Mach-Zender type interferometer in which a delay element has been introduced in one leg of the optical path. This results in formation of an interference pattern upon recombination of the light from both legs of the interferometer. The Doppler effect resulting from the movement of any reflective surface in the sample results in a phase-shift in the interference fringe pattern proportional to the velocity of the reflective surface (see inset, fig A5). This interference pattern is imaged onto an optical streak camera[2] which records a record of the phase, $\phi(t)$, as it evolves in time. The delay incurred by the etalon is precisely known and determines the sensitivity of the diagnostic such that velocity can be determined directly from the phase history, $\phi(t)$.

For all results presented here, the shock front itself was optically reflecting such that the VISAR records the shock velocity, U_S. U_S is related to the phase by the following relation

---

[2] See Chapter 2 for a description of the streak camera. Detailed information is available in the following reference: High Dynamic Range Streak Camera C7700 Instruction Manual and Test Report, Ver.1.3, 2006.7, 6660-401-02, Hamamatsu Photonic Systems, Bridgewater, N.J., 08807-0910.

$$U_S = \left(\phi(t) + b\right)\left(\frac{\lambda}{2\lambda\left(1+\delta\right)n_0}\right) \tag{A6}$$

in which $\phi(t)$ is the fringe position measured as a fraction of the fringe period. The term b represents the number of integer fringe shifts relative to zero (observed from the static target). The final term defines the velocity associated with one fringe shift (termed 'VPF', for 'velocity per fringe'), where λ is the probe beam wavelength, τ is the optical delay time introduced by the etalon, $(1+\delta)$ is a correction for optical dispersion in the etalon, and n_0 is the ambient index of refraction of the sample, through which the VISAR observes the shock. A single interferometer would not permit determination of b, since every integer (2π) phase-shift is indistinguishable. For this reason, two interferometers with differing sensitivities are simultaneously employed for every experiment. Comparison of the two records allows the experimentalist to unambiguously distinguish the proper phase shift as a function of time and thus ensures correct determination of the shock velocity. Errors in measured shock velocity using this technique are typically less than 1-2%, corresponding to a resolution of ~5% of a fringe shift or better.

OPTICAL REFLECTIVITY

Optical reflectivity at 532 nm ($R_{\lambda=532}$) is obtained by comparing the reflected intensity of the VISAR probe beam with the pre-shock signal from the polished aluminum surface backing the sample and the original, unperturbed shape and intensity of the VISAR probe pulse.

For most measurements, the VISAR probe pulse is split before it encounters the sample such that the reflected portion can be compared to the intensity of the split pulse that did not encounter the sample (thus serving as a reference for the pulse shape and intensity as a function of time). By dividing the reflected signal by the unreflected signal, percent reflectivity can be determined as a function of time as

$$R_{\lambda=532nm}(t) = \frac{I_{reflected}(t)R_0}{I_{reference}(t)} \tag{A7}$$

where R_0 is a normalization factor defined by the pre-shock reflectivity from the Aluminum buffer backing the sample. This is calibrated at 85%, which is the value used for the current studies.

STREAKED OPTICAL PYROMETRY

A Streaked Optical Pyrometry system observes the thermal emission from the sample. Absolute temperatures are extracted by calibration against either a known standard material (α-SiO_2) or against a standard of known spectral radiance such as a Tungsten ribbon filament lamp. A detailed description of this diagnostic and associated calibration procedures is given in Chapter 2. The pyrometry system at the OMEGA facility has been described previously by Miller *et al.*, 2006 while the corresponding system at the Janus facility is described by Spaulding *et al.*, 2007.

EXTRACTION OF EQUATION OF STATE BY IMPEDANCE MATCHING

In order to define the shocked state in the sample using the Rankine-Hugoniot equations, both U_S and u_p must be measured unless the equation of state of the material is known *a priori*. The VISAR diagnostic typically permits observation of only one of these quantities, however. For the present studies, that is the shock velocity, U_S. For cases in which the U_S-u_p relationship is unknown, impedance matching allows simultaneous determination of both quantities [Zel'dovich and Raizer, 1967]. This technique involves abutting the sample material against another material of known EOS and observing the shock front as it transits the interface between the standard material and the sample (fig. A6). Since mass and momentum must be continuous across the boundary between materials, a common pressure and particle velocity will be achieved in both materials according to their relative densities. This common state can be determined by measuring U_S at the interface and then using the known Hugoniot of the standard and the Rankine-Hugoniot equations derived above. α-SiO_2 was used as the reference material in these studies since its EOS has been previously measured [Hicks, 2005; Knudson, 2009].

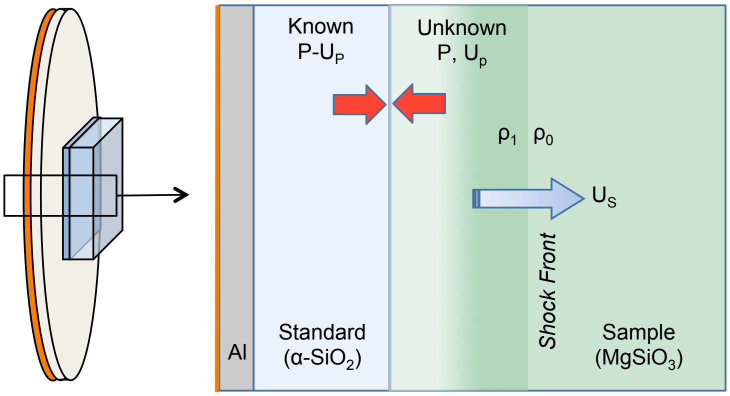

FIGURE A6. An enlarged cross-section of a typical EOS target in which the sample (of unknown EOS) abuts a material of known EOS (α-SiO_2). Pressure and particle velocity, u_p, are continuous at the interface such that measurement of U_S in both materials at the interface is sufficient to define U_S and u_p simultaneously in the sample. Measurement of U_S using the VISAR may be checked for consistency against the observed transit time through the sample (of known thickness).

Because the EOS for α-SiO_2 is known, measurement of U_S at the interface is sufficient to define P and u_p in both the standard and the sample. We plot the principle Hugoniot of α-SiO_2 in the right hand panel of Figure A7. Measurement of U_S in the sample defines a line with slope $\rho_0 U_S$ according to the second jump condition ($P=\rho_0 U_S u_P$). This is referred to as a 'Rayleigh line', which is the chord joining the initial and final states for any shock experiment. The intersection of the Rayleigh line and principle Hugoniot defines the shock state in the α-SiO_2 standard as the shock reaches the sample. In order for the two materials to come to the same P-u_p state, a reshock or release will occur in the α-SiO_2 depending on the relative impedance of the abutting sample. If the sample has a higher density than the standard, a shock will be launched back into the standard. This reshock is approximated by reflecting the principle Hugoniot of the standard about the particle velocity observed at the interface. Since the VISAR observes U_S in the sample, a Rayleigh line for the sample may be plotted in the same manner as for the standard (with slope $\rho_0 U_S$). The intersection of this Rayleigh line with the reflected α-SiO$_2$ Hugoniot then defines the common shocked state. With u_P determined in this manner and U_S observed directly with VISAR, a single experiment thus yields a single point in U_S-u_P space for the sample while several such experiments define the U_S-u_P Hugoniot of a given phase.

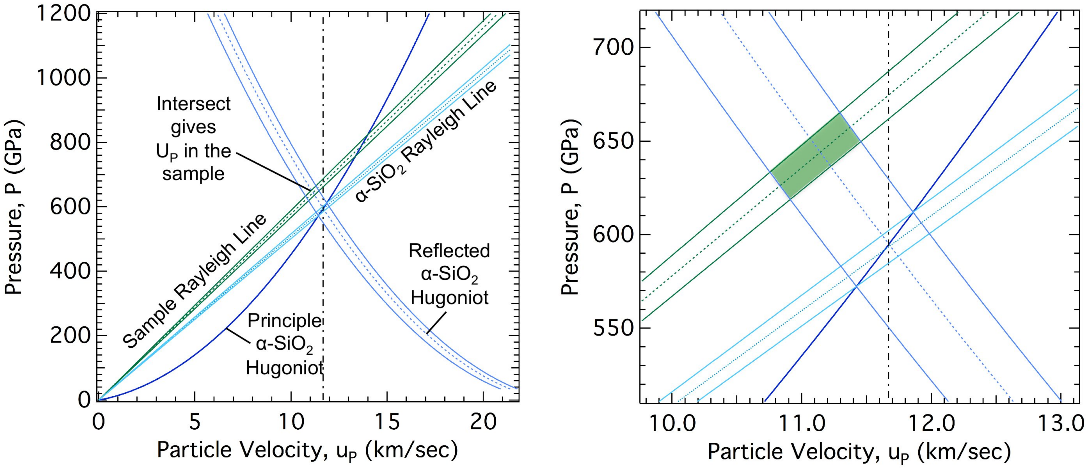

FIGURE A7. The Rankine-Hugoniot equations allow a graphical construct defining the behavior of the shock front as it encounters the interface between dissimilar materials. The intersection of the Rayleigh line for the sample and the reflected Hugoniot of the standard (α-SiO$_2$) define the common shocked-state at the interface. In this manner, U_S and u_p may be determined simultaneously in the sample.

Representative uncertainties are plotted as solid lines in Figure A7. Error in the measured shock velocity and in the initial density define the uncertainty in the slope of the Rayleigh lines and, consequently, in the reflected Hugoniot of the standard. Representative errors from a single experiment are illustrated by the shaded trapezoid in the right-hand panel of Figure A7, which is an enlarged view of the intersection shown in the left panel. In this case, a 2.5% uncertainty in U_S corresponds to a 3.5% uncertainty in pressure in the sample.

REFERENCES

Barker, L.M., and R.E. Hollenbach, Laser interferometer for measuring high velocities of any reflecting surface, *Journal of Applied Physics*, *43* (11), 4669-4675 (1972).

Celliers, P.M., Bradley, D.K., Collins, G.W., Hicks, D.G., *Rev. of Sci. Instrum.*, **75**, 11 (2004).

Hicks, D.G. *et al., Phys. Plasmas,* **12**, 082702 (2005).

Hicks, D.G. *et al.*, *Phys. Rev. Lett.,* **97**, 025502 (2006).

Knudson, M.D., Desjarlais, M.P., *Phys. Rev. Lett.,* **103**, 225501 (2009).

Miller, J. E. *et al*., *Rev. Sci. Instrum.,* **78**, 034903 (2006).

Spaulding, D.K., Hicks, D.G., Smith, R.F., Eggert, J.H., McWilliams, R.S., Collins, G.W., Jeanloz, R., *Proceedings: Shock Compression of Condensed Matter*, edited by M. Elert, M.D. Furnish, R. Chau, N. Holmes, and J. Nguyen, © 2007 American Institute of Physics, 1071.

Zeldovich, Y.B., Raizer, Y.P., *Physics of Shock Waves and High Temperature Phenomena*, Academic Press, New York, 1967.

Appendix B
Streaked Optical Pyrometer: Technical Details

The following information includes the technical specifications, layout and calibration details for the Janus Streaked Optical Pyrometry (SOP) System as it was used for the present studies. An example of the data reduction process is also given. This material is intended to complement the detailed discussion of shock temperature measurements given in chapter 2.

TABLE B1 Optical Components for the Janus Streaked Optical Pyrometer

ABBREVIATION	IDENTIFICATION	FOCAL LENGTH (MM)	SIZE (INCHES)	COMPANY/PART NUMBER
BS	Planar Blast Shield	--	2	--
146 mm Objective	Cemented Achromat Lens	250	2	CVI/AAP-250.0-50.8-425-675
	Meniscus Lens	350	2	Melles Griot/01LMP031/078
M1-M4	Aluminized Turning Mirror	--	3	CVI/PAUV-PM-3050-C
CW	Broadband Coated Target Chamber Window	--	9	--
L1-L5	Cemented Achromat Lens	1000	2	CVI/AAP-1000.0-50.8-450-750
PSC	Periscope (Stacked Turning Mirrors)	--	3	e.g. CVI/PAUV-PM-3050-C
DBS	Dichroic Beam Splitter	--	3	CVI/LWP-45-RU532-TU615-PW-3025-UV
ND	Double Neutral Density Filter Wheel	--	2	(CVI/ND-10-2.00)-(CVI/ND-400-2.00)
N1-N2	Holographic Notch Filter for 532 nm	--	2	Kaiser Optical/HSNF-20862
CL1	Concave Cylindrical Lens	-500	2	CVI/SCC-50.8-254.3-C -500-850
CL2	Convex Cylindrical Lens	+100	2	CVI/SCX-50.8-50.9-C-500-850
M5	Aluminized Turning Mirror	--	2	e.g. Melles Griot/02 MPG-011/028
R1	590 nm Color Glass Filter (optional)	--	2	e.g CVI/OG590

TABLE B2. Detector Specifications

CAMERA	Hamamatsu C7700-01 High Dynamic Range Streak Camera Serial Number 420061
FRONT-END OPTICS	Model A1976-04, 2180711, Serial Number 610064
CCD	Hamamatsu Model C4742-98, Serial Number 440216
CCD COUPLER	Model A7703-01, Serial Number 480010

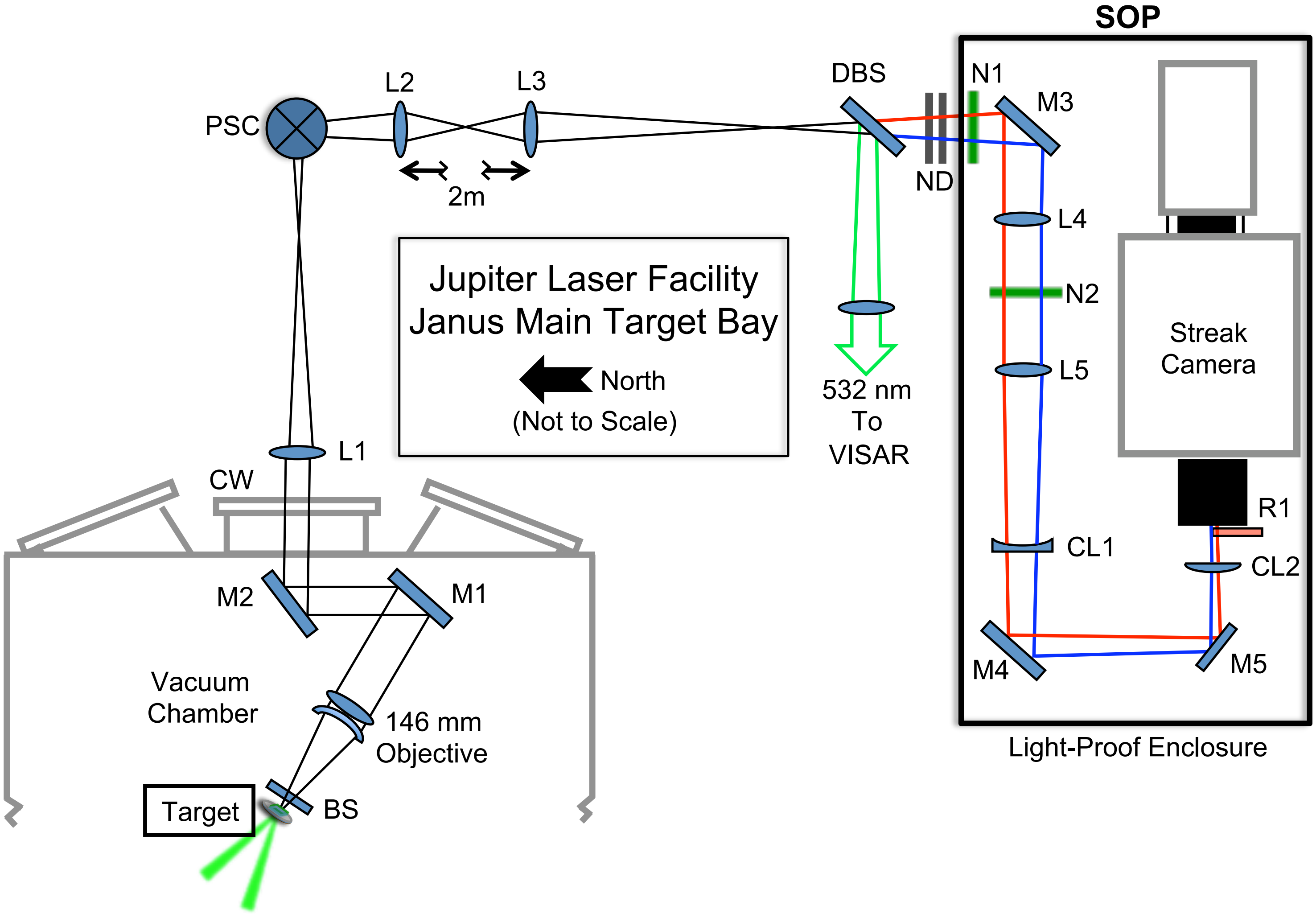

FIGURE B1. Illustrating the optical layout for the Streaked Optical Pyrometer (SOP) developed for used at the Janus Laser Facility, Lawrence Livermore National Laboratory. Thermal emission is conveyed from the vacuum chamber, is then split from the VISAR wavelength using a dichroic beam splitter (DBS), and is imaged by the pyrometry system on a Hamamatsu C7700 optical streak camera. Optical elements are identified in table B.1.

FIGURE B2. Calibration Results for the SOP Streak Camera Adjustable System Parameters (see chapter 2 for a complete description of calibration techniques and figure 2.3 for a diagram of the streak camera components)

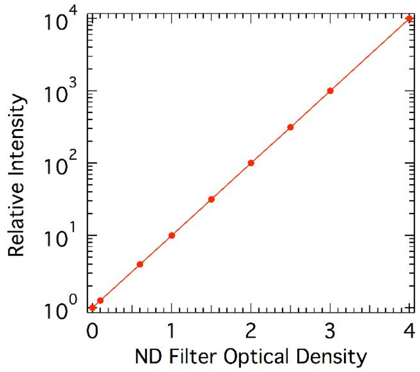

The effect of introducing ND filters to attenuate the intensity was checked to ensure that the streak camera responded linearly with intensity. The results match the expected logarithmic trend given by Beer's law. These results were collected with 20 μsec sweeps, gain = 30 and CCD exposure time = 10 msec. Intensity is determined by sampling an area on the CCD 40 pixels wide by 1024 pixels in length.

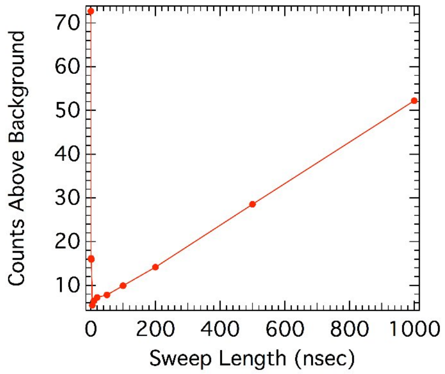

The effect of sweep speed on measured intensity was determined by varying the sweep with the camera set at gain = 20 and the CCD exposure time = 10 msec. The results are found to be linear with the exception of the shortest sweeps. The anomalously high counts for sweeps less than 5 nsec are believed to be due to automatic amplification by the camera for very low-light levels when the sweep setting is short. The camera is operated in the linear regime for all experiments, using sweep settings of 10 nsec or greater so that the intensifier is not activated.

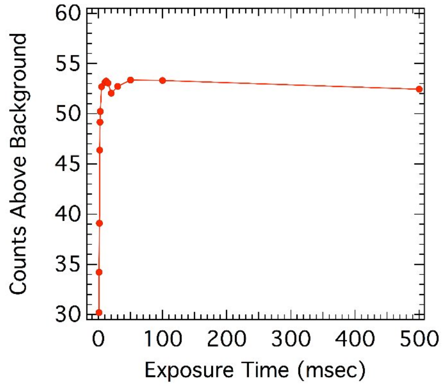

CCD exposure time was varied and intensity measured using 1 μsec sweeps with gain = 20. The exposure time is the time the CCD 'reads' the phosphor screen. The calibration results show that for exposure times longer than 10 msec, the measured intensity is ~ constant. This appears to indicate the characteristic relaxation time of the phosphor such that arbitrarily long exposure times do not record higher intensity. Exposure times of 10 msec were used for all experiments at the Janus facility according to this result.

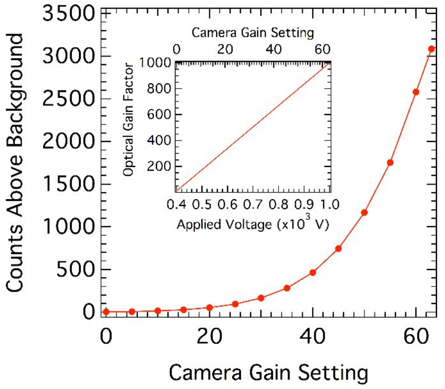

The camera's gain setting controls the voltage across the microchannel plate, hence the amplification of the signal. Gain (G) was varied using 1 μsec sweeps and 10 msec CCD exposure time. Intensity is found to obey a power-law relationship as a function of gain setting such that $I \propto (3.968 \times 10^{-4}) G^{3.825}$.

FIGURE B3. Example of Data Reduction for Shock Temperature Analysis

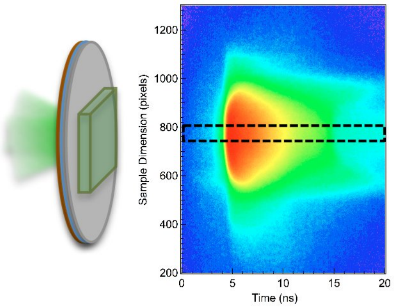

1. The raw data, shown to the left, is spatially-resolved in the vertical direction and temporally resolved in the horizontal direction. A line-out is taken over a region of interest shown by the black dotted box, resulting in the lower trace in the following plot.

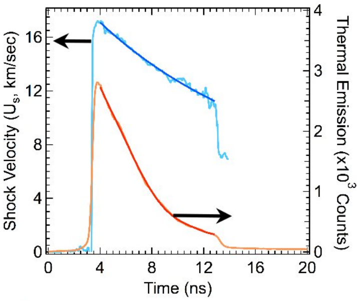

2. Background is subtracted from the intensity profile, determined for the same region of interest on the CCD (black, dotted box in top panel) using a pre-shot (dark) image. Shock velocity as a function of time is extracted separately from the VISAR record (top trace). Timing calibrations are used to correlate the two records temporally.

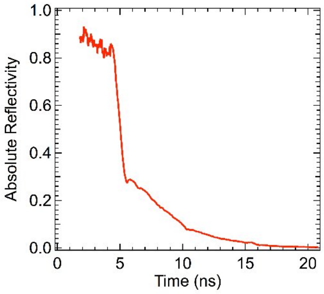

3. Reflectivity as a function of time is extracted from the VISAR data and is normalized to the preshot signal from the Al buffer backing the sample (~0.85). From this, we determine a time-dependent emissivity correction and apply this to correct the SOP intensity.

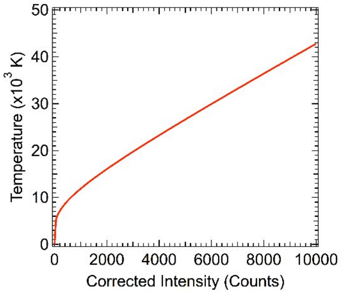

4. The calibration curve (*T vs. I*) is determined either by a separate shot or by placing an α-SiO_2 calibration sample next to the sample of interest (fig. 2.6). Temperature may then be calculated from the emissivity and background corrected values of intensity.

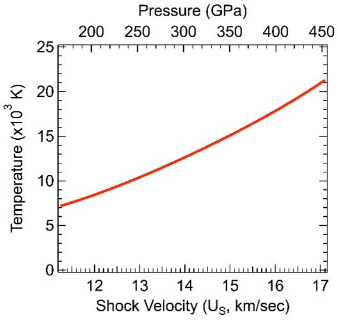

5. If the EOS is known, pressure may be extracted from the velocity data. If not, separate impedance-matching experiments are required (see appendix A). From #2, above, VISAR and SOP are correlated in time such that pressure may be plotted against temperature for the material.